Spring 2011

Epitaxial electrodeposition of metal oxide films and superlattices which exhibit resistance switching

Rakesh V. Gudavarthy

Department: Chemistry

EPITAXIAL ELECTRODEPOSITION OF METAL OXIDE FILMS AND SUPERLATTICES WHICH EXHIBIT RESISTANCE SWITCHING

by

RAKESH VATHSAL GUDAVARTHY

A DISSERTATION

Presented to the Faculty of the Graduate School of the

MISSOURI UNIVERSITY OF SCIENCE AND TECHNOLOGY

In Partial Fulfillment of the Requirements for the Degree

DOCTOR OF PHILOSOPHY

IN

CHEMISTRY

2011

Approved by

Jay A. Switzer, Advisor

Nicholas Leventis

Jeffery G. Winiarz

Manashi Nath

Matthew J. O'Keefe

PUBLICATION DISSERTATION OPTION

This dissertation has been prepared in the format used by *Journal of American Chemical Society, Advanced Materials, Chemistry of Materials* and *Journal of Materials Chemistry.* This dissertation consists of one article that has been published, two articles which have been submitted for publication and one article intended for submission. Paper I found on pages 37-47 and the related appendix, pages 102-112 is published in *Journal of American Chemical Society*. Paper II has been submitted to *Advanced Materials* (Pages 48-60) and the supporting information for the paper can be found in pages 114-119. Paper III has been prepared for publication in *Chemistry of Materials* (Pages 61-71) while paper IV has been submitted to *Journal of Materials Chemistry* (Pages 72-98). The appendix I includes the supporting information for paper I, published in the *Journal of American Chemical Society*. The appendix II has supporting information for paper II and is submitted to *Advanced Materials.* The appendices III, IV and V have unpublished results.

ABSTRACT

This dissertation presents an investigation of the electrodeposition of metal oxide films and superlattices on conducting polycrystalline and single crystal substrates. In the first part of the study, electrodeposition of magnetite (Fe_3O_4) films and superlattices in the magnetite/zinc ferrite system which exhibit resistance switching is studied. Paper I reports the electrodeposition of superlattices in the magnetite/zinc ferrite system and shows that only superlattices exhibit multistate resistance switching. In paper II, simple polycrystalline magnetite films electrodeposited on stainless steel crystals exhibit multistate resistance switching which can be tuned by controlling the composition of the films. Paper III describes the epitaxial electrodeposition of Fe_3O_4 films on Ni(111) substrates.

In the second part, electrodeposited epitaxial films of CuO onto achiral Cu single crystals using chiral precursors are studied. Paper IV describes chiral electrodeposition of CuO from copper(II) complexes of malic acid on Cu single crystals. X-ray pole figures in conjunction with stereographic projections are used to determine the absolute configuration of the films. X-ray crystal structures of copper(II) malate crystals are analyzed to understand the mechanism of chiral electrodeposition.

ACKNOWLEDGMENTS

I would like to thank Prof. Jay A. Switzer for his guidance, direction and support throughout my graduate studies. I would also like to thank Dr. Nicholas Leventis, Dr. Jeffery Winiarz, Dr. Manashi Nath, Dr. Frank Blum and Dr. Matt O'Keefe for guiding me and for agreeing to be a part of my graduate committee. I would like to thank my parents for encouraging me to pursue my doctoral degree and going through all the hardship to support my education. This dissertation is simply impossible without them. I am indebted to my father, Sujan V. Gudavarthy, for his constant encouragement during the hard times in my life. I cannot ask for more from my mother, Sharadha Gudavarthy, who has sacrificed all her life for my education and well-being. I would also like to thank my sister, Archana Gudavarthy, who has been a friend and a philosopher throughout my life. I would also like to thank my friends Sruthi Bhavanam, Sandeep Gorantla, Shardool Joshi, and Ashwin Patalay who have constantly supported me during the course of my study.

I would like to reserve special thanks for Dr. Eric W. Bohannan and Dr. Elizabeth A. Kulp, for their valuable discussions and suggestions. I would also like to thank the post-doctoral associates of the Switzer group, Dr. Steven Limmer, Dr. Vishnu Rajashekaran and Dr. Shaibal Sarkar for their guidance and intellectual discourses. Fellow group members Guojun Mu, Niharika Burla, and Zhen He also deserve mention for their assistance throughout my years at Missouri S&T. I would also like to thank the undergraduate students Andrew Wessel and Andrew Miller who worked with me and helped me finish different projects. I would also like to mention special thanks to Dr. Thomas Gemming at IFW Dresden for helping me with TEM samples. I would also like to thank Dr. Jon Reid, for providing me an opportunity to work at Novellus system.

I would also like to take this opportunity to thank the many graduate and undergraduate students, and staff members at the Materials Research Center and Chemistry department for their assistance and friendship. I would also like to thank ISC, CGS and IA members and all my friends for making my stay enjoyable.

Last but not the least; I would also like to acknowledge the financial support of the Department of Energy and the National Science Foundation.

TABLE OF CONTENTS

PAPER

APPENDICES

LIST OF ILLUSTRATIONS

Figure Page

INTRODUCTION

Paper I

Paper II

Paper III

Paper IV

Appendix A

Appendix B

Appendix C

Appendix D

Appendix E

LIST OF TABLES

NOMENCLATURE

Symbol	Description
β	Angle of Attack
α	Change in Coupler Angle

1. INTRODUCTION

1.1. ELECTRODEPOSITION

Electrodeposition is an inexpensive technique to produce materials with superior properties.[1] It involves surface phenomena, solid state processes, and processes occurring in the liquid state, and involves many scientific communities.[2] Electrodeposition is possible only on conducting substrates which are typically polycrystalline or single crystalline metals or semiconductors.[3-5] There are several factors like (1) substrate,[6-8] (2) pH of the solution,[9-12] (3) additives,[13-16] (4) applied current/potential,[17-22] and (5) solution concentration,[22] which affect the electrodeposition process. The thickness of electrodeposited films can be determined by monitoring the charge passed during the deposition. Electrodeposition has been used in the deposition of thin films of metals, [6, 23] alloys, [24, 25] ceramics, [26-28] semiconductors, [29-32] superlattices, [33-36] biominerals, [37] and superconductors.[38] Other techniques like chemical bath deposition, [39, 40] chemical vapor deposition, [41, 42] physical vapor deposition (sputtering), [43] molecular beam epitaxy, [44] laser ablation, [45] and sol gel [46] are also used in the deposition of thin films of these materials. One advantage of electrodeposition over other techniques is that the films can be produced near room temperature, minimizing solid state diffusion in the films produced. Electrodeposition has been widely used for producing protective coatings for many years; new applications have been found in the electronics industry.[47, 48, 49] Introduction of copper electrodeposition in the fabrication of interconnects in the high-end microprocessor and memory devices because of its low electrical resistivity, good electromigration resistance, and compatibility of dual damascene process has revolutionized the electronics industry. Recently, the electrodeposition technique, which exploits the thermodynamic stability of microscale or nanoscale liquid meniscus to deposit pure Cu or Pt with desirable size for interconnects and other complex three-dimensional structures has been demonstrated.[50] Electrodeposition is also a great technique to produce devices for the conversion or storage of energy, because the nanostructures are grown from the bottom up and, therefore, maintain good electrical contact with the substrate.[51] The metals, metal oxides, and superlattices produced by electrodeposition method have been shown to exhibit giant magnetoresistance,[52, 53]

resistance switching behavior,[54] enhanced optical properties,[55, 56] enhanced mechanical properties,[57, 58] and sensing properties,[59- 62] making electrodeposition a very versatile technique.

In this dissertation, the focus is on electrodeposition of transition metal oxides thin films and superlattices which exhibit resistance switching phenomenon. Electrodeposition of metal oxides can occur via (1) redox change, (2) pH change near the electrode, and (3) oxidation/reduction of complexing agents. In the redox change method, a metal ion is either oxidized or reduced at the electrode surface. This method has been used to produce oxides such as Cu_2O,[12, 63, 64, 65] Fe_3O_4,[66-69] Bi_2O_3,[70, 71] CeO_2,[72] AgO,[73] Tl_2O_3[74, 75] and PbO_2.[76] In the case of pH change, the local pH is increased or decreased by reduction or oxidation of water, causing precipitation of the metal oxide at the electrode surface. The technique has been used in the electrodeposition of CeO_2,[77, 78] ZnO,[79] ZrO_2[80] and various biomaterials.[37] Besides water oxidation/reduction for pH change, other species like O_2, [81] NO_3^{-2}, [82] and H_2O_2[83] can also be used for pH change. Finally, in the case of oxidation/reduction of complexing agents, the complexing agent coordinates with the metal ion and stabilizes the solution in high pH conditions and when oxidized releases the metal ion. The metal ion then reacts with OH^- ions from the base to precipitate the metal oxide on the electrode.[59, 60, 84, 85]

In the case of superlattices and multilayers, either a single-bath or dual-bath can be used for electrodeposition.[86] The single-bath method is simpler and is restricted to materials which form compatible electrolytes.[86] The single-bath method has been used in the electrodeposition of Cu/Ni,[87-96] Cu/Bi,[97] Cu/Ag,[98] Cu/Co[99] and Cu/CuO[100, 101] multilayers with modulation wavelengths down to 1.5 nm. In the case of dual-bath method, there is flexibility in the type of multilayers which can be electrodeposited.[86] However, the electrode needs to be transferred between two different solutions, making the process cumbersome. The dual-bath deposition method has been used to deposit multilayers in the Cu/Zn,[102] NiP_x/NiP_y[103] and Ni/NiP_x[103] systems. Defect-chemistry superlattices based on Tl_2O_3[33] and compositional superlattices in the PbO_2/Tl_2O_3[34, 35] system have been deposited from a single-bath by pulsing either the current or potential.

1.2. EPITAXIAL ELECTRODEPOSITION

Epitaxy can be defined as "the growth of crystals on a crystalline substrate that determines their orientation."[104] Epitaxial films are usually produced using molecular beam epitaxy (MBE).[105] The entire process takes place in an ultra-high vacuum.[105] MBE was the first technique to demonstrate monolayer-scale heterostructures.[106] In MBE, ultra-pure elements are individually heated in quasi-Knudsen effusion cells to their sublimation point, forming individual molecular beams.[107] The term "beams" means that the individual atom beams do not react with each other until they reach the wafer, due to the long mean free paths of the atoms. The wafer itself is maintained at elevated temperature where the atoms will react to form epitaxial films. The most important aspect of MBE is the slow deposition, which allows the films to grow epitaxially.[105] The epitaxial films so formed have superior properties, as the intrinsic properties of the material can be exploited rather than its grain boundaries. Mostly, but not limited to, epitaxial films of III-V semiconductors have been produced with this technique.[107] The films produced have superior electronic and optoelectronic properties. Quantum well structures can also be formed using the MBE method.[108] Although widely used; the major disadvantage of this technique is that it is not cost effective. Electrodeposition is a cost effective technique to produce epitaxial films. Electrodeposition being a solution process, offers degrees of freedom (pH, additives, potential etc.) to precisely control the size and morphology of the crystallites, which may not be accessible to UHV methods.

In epitaxy, the orientation of the deposited film is controlled by the orientation of the substrate.[109] There are two kinds of epitaxial films: (1) Homo-epitaxial, if the crystalline film is grown on a crystalline substrate which is a same material. (2) Hetero-epitaxial, if the crystalline film is grown on a crystalline substrate which is a different material.[110] Important factors that influence epitaxial growth are (1) lattice mismatch, and (2) binding energy between the deposited film and the substrate.[111] Generally, an epitaxial film will deposit with an orientation which forms the lowest mismatch with the substrate. The mismatch between the lattice parameter of deposited film and the substrate is adjusted by rotation of the film to form coincidence lattices. An example for such a system is the electrodeposition of Prussian Blue (PB) on Au(110) substrate.[112] The lattice mismatch between the PB film and substrate is 148%, which reduces to 0.4%, by coincidence

lattice formation. Similarly, epitaxial ZnO films were deposited on Si(001) substrate via chemical bath deposition, where the lattice mismatch reduced from 40% to 0.25% by tilting the film 51° with the normal.[113] Other examples for large lattice mismatch systems are perovskite ferroelectrics on MgO, MgO on GaAs, and GaN, AlN, ZnO, $LiNbO_3$ on sapphire.[114]

The first growth technique applied to thin layer epitaxy was liquid phase epitaxy (LPE).[115] In LPE, a supersaturated liquid solution is brought in contact with a substrate in a temperature controlled furnace. The material deposits epitaxially on the substrate when it is cooled carefully. In such case, controlling the thickness of the films is difficult. However, in electrodeposition, which is also a liquid phase technique, the thickness of the films can be controlled by controlling the charge passed. Extensive work has been carried out in the underpotential deposition of metals on single-crystal substrates.[116-122] However, there has been little work on the electrodeposition of epitaxial films in the micrometer range. Switzer's group has focused on electrodeposition of epitaxial films of CuO,[59, 60] δ-Bi_2O_3,[70, 71] Cu_2O,[63-65] Fe_3O_4,[66, 67, 69] ZnO,[113, 123] SnS,[124] Tl_2O_3,[74, 75] AgO,[73] PbO_2,[76] and superlattices[33, 34, 35, 125, 126, 127] onto Au, Cu, Si and InP single crystals. Moffat has produced epitaxial strained-layer Cu/Ni superlattices on Cu(100).[122] Allongue et al. have reported epitaxial electrodeposition of Ni films onto GaAs(100).[128] Lincot et al. have electrodeposited epitaxial films of CdTe on InP(111)[129] and ZnO on GaN(0002).[130] Kolb and coworkers have shown epitaxial clusters of Pb, Cu and Au can be grown on Si(111) substrate.[131, 132] Beaunier et al.[133] have reported epitaxial electrodeposition of PbTe on InP(111) single-crystal. Chason and coworkers have demonstrated epitaxial electrodeposition of bulk single crystals of Ni.[134] The first part of this dissertation focuses on electrodeposition of epitaxial superlattices in magnetite/zinc ferrite system. This dissertation extends the work to electrodeposition of polycrystalline films of Fe_3O_4 on stainless steel and epitaxial electrodeposition of Fe_3O_4 on Ni, and InP single-crystal substrates.

1.3. RESISTANCE SWITCHING

The rapid improvement in modern technology is bringing in new challenges for the development of memory devices both in terms of architecture and storage.

Conventional memory devices are reaching their scaling limits. In such a scenario, alternatives storage devices, with smaller sizes and higher performance are necessary. Alternative memory devices like magnetic random access memory (MRAM), [135, 136] flash memory,[137] phase change memory (PRAM),[138] ferroelectric random access memory (FeRAM)[139] and resistance random access memory (RRAM)[140, 141] are being considered. In the case of MRAM, the magnetic tunnel junction principle is used for memory storage. Flash memory uses the electrically erasable programmable memory, to erase and write the data. PRAM uses the change in resistance between the crystalline and amorphous states of compounds, FeRAM uses the polarization of material which can be reversed and RRAM uses the change in resistance of the material by applying an electric field for non-volatile memory storage.[142]

Out of all these possibilities, RRAM devices are considered to have several advantages, such as fast writing times, high densities, and low operating voltages.[143] The RRAM set up is like a simple capacitor, with metal oxide sandwiched between two metal electrodes, as shown in Figure 1.1. Because of its simple structure, multilevel stacking memory structures have been proposed.[144] The phenomena of resistance switching has been observed in a variety of metal oxides[140, 141] and organic compounds.[144, 145, 146] Hickmott[147] reported for the first time that the $Al/Al_2O_3/Al$ structure showed hysteresis in current-voltage measurements, indicating that resistive switching occurs. Burch et al.[148] and Freud et al.[149] reported independently resistance switching behavior in magnetite at 77 K. Resistance switching behavior has been reported in a large number of binary oxides.[150, 151]

Resistive switching behavior can be classified into basically two types (1) unipolar resistive switching and (2) bipolar resistive switching.[142] In unipolar resistive switching, the switching direction depends on the magnitude of applied voltage but not on the polarity. The behavior has been observed in PCMO,[152] $SrZrCO_3$,[153] $SrTiO_3$,[154] NiO,[141, 151] TiO_2,[156] Cu_2O,[157] CuO,[158] SiO_2,[159] and ZrO_2.[160] In the case of bipolar resistance switching, the switching direction depends on the polarity of the applied voltage. This type of behavior occurs with many semiconducting oxides such as complex perovskite oxides. [161, 162, 163]

The path for resistance switching can be broadly classified into two types: (1) filamentary conducting path,[164, 165] and (2) interface-type path.[155] In the filamentary conducting path, a conductive filament is formed due to thermal anodization (heating the sample to form a passivation layer on the surface) or Joule heating near the interface between the metal electrode and the oxide, which changes the resistance of the material.[164, 165] However, in the interface-type path, the resistance switching takes place at the interface between the metal electrode and the oxide. The driving mechanism for interface-type path can be electrochemical migration of oxygen vacancies, [155, 166-168] trapping of charge carriers, [161-163] and a Mott transition[169-171] induced by carriers doped at the interface.

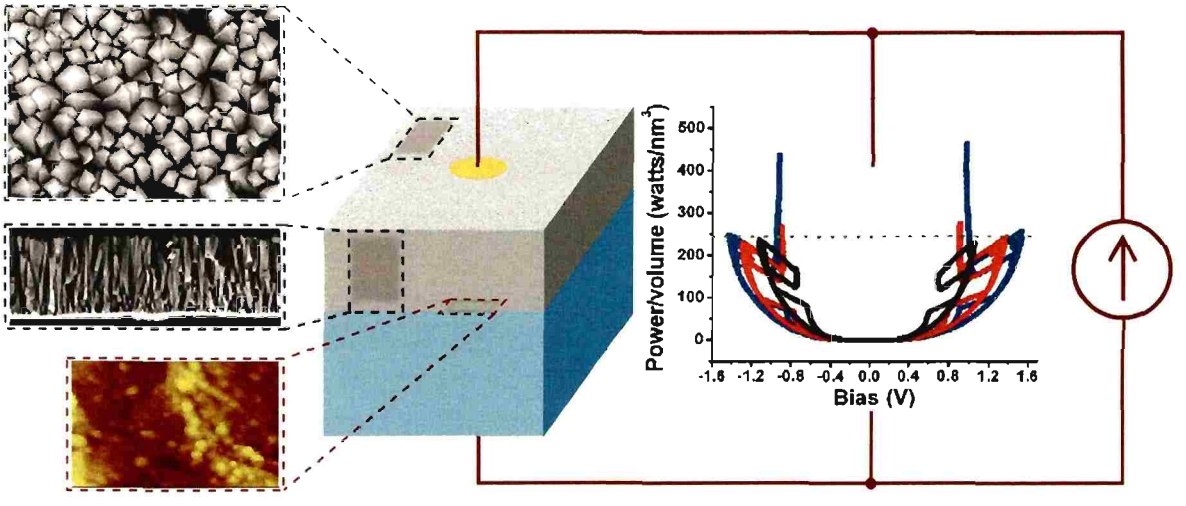

Figure 1.1. The figure shows resistance switching experimental setup for a polycrystalline magnetite (gray) on a polycrystalline stainless steel (SS) substrate (blue). The blown up regions on the magnetite film shown are the top-plan view, cross section SEM images and bottom AFM image. The plot inside the electrical circuit corresponds to power density plot with different contact areas.

Recently, resistance switching behavior has been observed in nano-phase magnetite,[172, 173] thin epitaxial films,[172] and defect chemistry superlattices of magnetite.[174] The resistance switching in magnetite does not happen at room temperature and does not follow the conventional paths for resistance switching.[172-174] For the switching to happen in magnetite, the films are held at temperatures below the Verwey transition, where

magnetite has a different phase (distorted cubic) and higher resistance. To such a film, when an electric field is applied, an insulator-to-metal phase transition occurs, and upon removal of the electric field the crystal goes back to the original state. For such a transition to occur at lower bias, it was shown that nano-phase magnetite is critical.[172, 174] Bulk single crystals exhibit resistance switching only when a large electric field is applied.[174, 175] The mechanism of resistance switching in magnetite has been attributed to electric field driven, [172] Joule heating[176] and in some cases both.[174]

In this dissertation, resistance switching in magnetite has been studied in the defect chemistry superlattices, epitaxial films, and polycrystalline films of magnetite. Defect chemistry superlattices in magnetite and polycrystalline films of magnetite on stainless steel exhibit phase transition jump, whereas the epitaxial films do not show the phase transition jump.

1.4. MAGNETITE

Magnetite (Fe_3O_4) is the oldest magnetic mineral in nature.[177] It has an inverse spinel structure with space group Fd3m and a lattice parameter of 0.8397 nm. The crystal structure of magnetite is shown in Figure 1.2. The tetrahedral sites are occupied by Fe^{3+} ions, whereas the octahedral sites are occupied by equal number of Fe^{3+} and Fe^{2+} ions. This model is in agreement with the crystal field stabilization energy (CFSE) calculation for Fe_3O_4. Fe^{2+} ions has six 3d electrons with the octahedral sites having a higher CFSE (11.9 kcal.mol^{-1}) than tetrahedral sites (7.9 kcal.mol^{-1}). On the other hand, the Fe^{3+} ions which has a zero CFSE in high spin configuration (five 3d electrons) at both tetrahedral and the octahedral sites has no site preference, occupies the octahedral sites. [178]

Magnetite exhibits ferrimagnetism below the Curie temperature of 860 K.[186] Ferrimagnetism results from antiparallel spin coupling and incomplete magnetic moment cancellation. Magnetite also has 100% spin polarization at the Fermi level.[181] Due to the high Curie temperature and 100% spin polarization, Fe_3O_4, is a potential candidate for spintronic devices and other device applications. Although 100% spin polarization has been predicted based on electron band structure calculation in Fe_3O_4, experimentally, a lower value has been reported due to deviations from stoichiometry. Debkov et al. reported that Fe_3O_4 has a negative spin polarization of -80 ± 5% for a Fe_3O_4(111) film at

room temperature.[187] The imbalance in the spin polarization results in large magnetoresistance values for Fe_3O_4. Magnetoresistance studies have been conducted on bulk Fe_3O_4 single crystals,[188, 189] deposited single crystal films,[179, 190, 191] polycrystalline films,[192-194] powders,[180, 195] and nanocontacts.[12] Coey et al.[196] attributed the MR behavior to the alignment of magnetization of the grains in the presence of a magnetic field. Kothari et al.[67] also observed approximately 6.5% MR in electrodeposited polycrystalline films which they attributed to the transport of spin polarized electrons across the spin-aligned grain boundaries.

Fe_3O_4 is a conductor at room temperature with a resistivity of ~ 0.01 Ω-cm.[3, 4] The electronic conduction is attributed to hopping of charge carriers between the Fe^{2+} and Fe^{3+} ions.[179, 180] At lower temperatures, the electrical resistivity of Fe_3O_4 increases due to charge re-ordering on the Fe^{3+} and Fe^{2+} ions in the octahedral sites.[181] The phenomenon was first discovered by E. J. W. Verwey in 1939.[182] Verwey found that the resistance increases abruptly by a factor of 100 at ~120 K in a Fe_3O_4 sample. This phenomena has since been called the Verwey transition, below which Fe_3O_4 becomes paramagnetic and the crystal structure changes from cubic to a slightly distorted cubic (resembling monoclinic), and ordering of the Fe^{2+} and Fe^{3+} occurs.[183, 184] X-ray diffraction measurements also confirmed lattice distortions at lower temperatures.[185]

Magnetite has also been shown to exhibit resistance switching behavior when it is placed at temperatures below the Verwey transition temperature and either current or bias is increased.[172-176] Bulk single crystals of magnetite exhibit resistance switching, when a large electric field is applied to the crystal.[175, 176] Recently, Natelson et al.[172] showed that the resistance switching can be achieved at low electric fields, if nano-phase magnetite is used. Switzer et al.[174] reported multistate resistance switching in electrodeposited magnetite defect chemistry superlattices. They observed that the superlattices exhibit both low-to-high and high-to-low resistance switching at relatively low bias during the iV measurements. Both Natelson and Switzer discussed the importance of the nano-phase magnetite for resistance switching to happen at a lower bias.[172, 174] The mechanism of resistance switching has been attributed to Joule heating, electric field driven and in some cases both.[172-176] It is still not clear as to which of these mechanisms is true for Fe_3O_4.

Odagawa et al.[219] reported a low-to-high resistance switching and attributed it to the oxidation of Fe_3O_4 films to γ-Fe_2O_3.

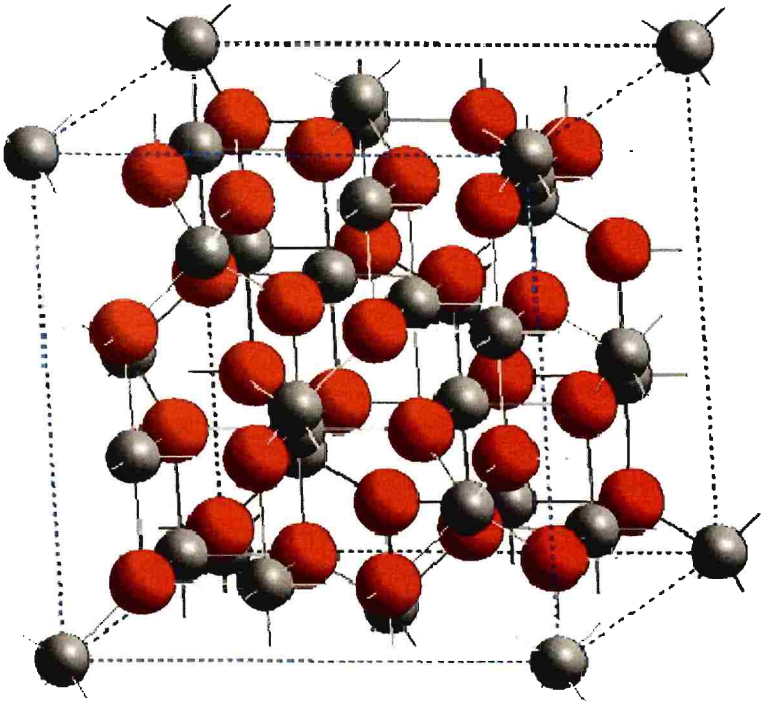

Figure 1.2. A unit cell of magnetite (Fe_3O_4) with an inverse spinel structure, space group Fd3m.

In this dissertation, magnetite films electrodeposited on polycrystalline SS substrates, epitaxial films and superlattices were characterized for magnetic properties, and for the resistance switching behavior. The films were electrodeposited from an alkaline solution of Fe(III)-TEA bath at 80 °C. Films of Fe_3O_4 were deposited in the present work on polycrystalline stainless steel, Au sputtered glass substrates and single crystals of Au, Ni and InP.

1.5. COPPER OXIDE

Copper(II) oxide (CuO) has a centrosymmetric structure (i.e. it has an inversion center, i), hence the crystal structure of CuO is achiral. CuO has a monoclinic structure, with the space group C2/c, and the lattice parameters are a = 0.4685 nm, b = 0.3430 nm, c = 0.5139 nm, $\alpha = \gamma = 90^{\circ}$, and $\beta = 99.08^{\circ}$. In the monoclinic structures, the b-axis is

unique, and is perpendicular to both a and c axes. Based on the space group, a glide plane can be perpendicular to b axis. An achiral plane has a mirror or glide plane perpendicular to it. Therefore, all planes which are parallel to b-axis are achiral, i.e. planes with k = 0. All other planes are chiral in CuO.

Chirality is the handedness of the molecule. Chiral molecules are nonsuperimposable mirror images of one another. Chiral molecules are of great interest to the pharmaceutical industry.[197] Only one of the enantiomers may be useful while the other toxic, therefore separation of these enantiomers is very critical. Traditionally, the industry has relied on using homogenous solution-based catalysis or enzymatic reactions to carry out enantiospecific syntheses. Separation of enantiomers can be improved if heterogeneous catalysts can be used.[198]

A lot of work has been done in developing heterogeneous catalysts for enantiomeric separations. Mostly the work has concentrated on adsorbing chiral molecules on surfaces and breaking the symmetry. A classic example is the Orito[199] reaction, in which hydrogenation of α-ketoesters over alumina supported platinum catalysts modified with chiral cinchonidine yields enantioselective products. Another example is the modification of a Ni surface by adsorbing (R,R)-tartaric acid. The modified Ni surface was used to catalyze β-ketoesters with a 90 % enantiomeric excess of the R-product over the S-product.[200] However, the durability of such surfaces for practical applications is of concern. An alternative to adsorption can be producing intrinsic chiral surfaces. High index surfaces of metals have kink sites which can act as chiral sites.[201] Rules to identify such surfaces have been proposed.[202, 203] An example for such a surface is Pt(643). Scholl et al.[204] reported enantiospecific adsorption of chiral molecules on these surfaces using Monte Carlo simulations, while Attard et al.[205] showed enantiospecific electrochemical oxidation of glucose on these surfaces.

Switzer et al. demonstrated a new approach to develop chiral surfaces for heterogeneous catalysis.[59, 60] In their approach, a metal oxide such as CuO, which is not intrinsically chiral, was deposited as a chiral film on low index surfaces of Au single crystal. The chirality to the film was directed by the chiral precursors present in the solution. X-ray pole figures were used to determine the chiral orientation of the CuO films and azimuthal scans were used to determine the enantiomeric excess. The chiral

CuO films also showed selectivity, and the selectivity was improved by selectively etching the films in chiral solutions.[61, 62] Widmer et al.[206] have since verified the surface chirality of these films by X-ray photoelectron diffraction. Besides CuO, biominerals such as calcite with chiral facets were also electrodeposited.[37]

In this dissertation, chiral CuO films were deposited on single crystal surfaces of Cu(111) and Cu(110) from copper(II) complexes of malic acid. The handedness of the film is directed by the chirality of the deposition solution. To understand the mechanism of chiral electrodeposition, copper malate crystals were synthesized and their structure was determined using X-ray crystallography.

2. EXPERIMENTAL

2.1. SUBSTRATE PREPARATION

2.1.1. Polycrystalline stainless steel substrates of two kinds SS 304 L (Fe, Cr < 20%, Ni < 12%, C < 0.03%, Mn < 2%, Si < 1%, P < 0.045%, and N < 0.1 %) and SS 430 (Fe, Cr < 18%, Ni < 0.75%, C < 0.12%, Mn < 1%, Si < 1%, P < 0.04%, and S < 0.03%) were purchased from Metal Samples Company (Munford, Alabama, USA). The SS substrates were successively mechanically polished at 1 and 0.25 μm. After polishing, all substrates were ultrasonically cleaned in a 1:1 acetone and ethanol mixture, followed by rinsing with deionized water. The substrate was wrapped with a SS wire to make electrical contact.

2.1.2. Single crystal Au substrates with 99.99 +% purity were purchased from Monocrystal Company (Medina, OH, USA). The diameter of the crystals was 10 mm and the thickness was 2 mm. The crystal was initially mechanically polished at 0.25 μm followed by electro-polishing. Electro-polishing is carried out anodically, at a constant current density of 1.5 A/cm^2 in a moderately stirred solution of 50 vol. % ethanol, 25 vol. % ethylene glycol, and 25 vol. % concentrated HCl at 55 °C. Electro-polishing is usually carried out for 30-45 s based on the requirement. A graphite electrode serves as the counter electrode. Following the electro-polishing, flame annealing of the Au crystal is carried out. Flame annealing is carried out in dark room using a hydrogen flame. The Au single crystal is annealed till it turns red and the flame is immediately turned off. Finally, the sample is wrapped with a Au wire for electrical contact.

2.1.3. Single crystal Ni Substrates with 99.99 +% purity were purchased from Monocrystal Company (Medina, OH, USA). The diameter of the crystals was 10 mm and the thickness was 2 mm. The crystal was initially mechanically polished at 0.25 μm followed by electro-polishing. The bath for electro-polishing Ni single crystal is prepared by taking 29 parts of distilled water (approximately 87 ml) and adding 39 parts of conc. H_2SO_4 (approximately 117 ml). A small amount of nickel sulfate is added to the mixture and the solution is stirred till it reaches room temperature. Electro-polishing is then carried out anodically, at a constant current density of 1.5 A/cm^2 at a high stir rate of 600-800 rpm for 30-45 s. A Ni foil serves as a counter electrode. The electro-polishing is

carried out at room temperature. Electrodeposition was carried out immediately after electro-polishing the crystal, to avoid the formation of any native oxide.

2.1.4 Single crystal Cu substrates with 99.99 +% purity were purchased from Monocrystal Company (Medina, OH, USA). The diameter of the crystals was 10 mm and the thickness was 2 mm. The crystal was initially mechanically polished at 0.25 μm followed by electro-polishing. The electro-polishing is carried out in a 67 vol. % orthophosphoric acid aqueous solution at a potential of 1.45 V vs. SCE. Whereas a meniscus method is used for electro-polishing other single crystals, Cu single crystals are completely dipped into the solution, and are placed at 45 ^{o} angle to the counter electrode (Cu foil), to achieve high quality surfaces. A black CuO film is formed after electro-polishing which is removed by rinsing with DI water. Immediately before electrodeposition, the crystal is treated with a drop of 0.1 M $HClO_4$ to remove any native oxide present.

2.1.5 Single crystal InP substrates were supplied by Wafer Technology Ltd., doped with sulfur to a resistivity of approximately 1.6 x 10^{-3} Ωcm. The wafers are degreased in ethanol and acetone and then rinsed with DI water before etching. The etch carried out in solution of 3 M H_2SO_4 for 3 min to remove the native oxide, followed by a thorough washing with DI water. Ohmic contacts are made using Ga-In eutectic.

2.2. MAJOR CHARACHERTIZATION TECHNIQUES

2.2.1 X-ray diffraction X-ray diffraction (XRD) is a non-destructive technique that reveals crystallography of an unknown material using monochromatic X-rays. X-rays are generated by an X-ray tube that uses a high voltage to accelerate the electrons released by a cathode to a high velocity. The so generated electrons collide with a metal target, the anode, creating the X-rays.[207] Different X-ray sources are used based on the need. Tungsten or a crack-resistant alloy of rhenium (5%) and tungsten (95%) are generally used in the medical field. When soft X-rays are needed for special applications like mammography, a molybdenum source is used. In crystallography, a copper target is most common, with cobalt often being used when fluorescence from iron content in the sample might otherwise present a problem. For a copper target, X-ray emissions commonly contains a continuous white radiation and two characteristic x-rays, K_α (λ =

0.15418 nm) and K_β (λ = 0.13922 nm) leading from 2p →1s and 3p →1s transitions, respectively. In general, the K_α transition is more intense than K_β, and is a combination of $K_{\alpha 1}$ and $K_{\alpha 2}$. This is because of the slight difference between two possible spin states of 2p electrons. Monochromatic K_α X-rays can be obtained by using suitable filters that absorb the unneeded white radiation and K_β. For example, a Ni foil is commonly used for radiation of copper target.[208]

X-ray diffraction works on the principle of Bragg's law, $n\lambda = 2d \sin\theta$, where λ is the x-ray wavelength, d is the lattice spacing and θ is the Bragg angle. The layers of a crystal act like weak reflecting mirrors for the X-rays. Only if the path difference of the reflected X-rays is a whole number of wavelengths does constructive interference occurs, as shown in Figure 2.1.

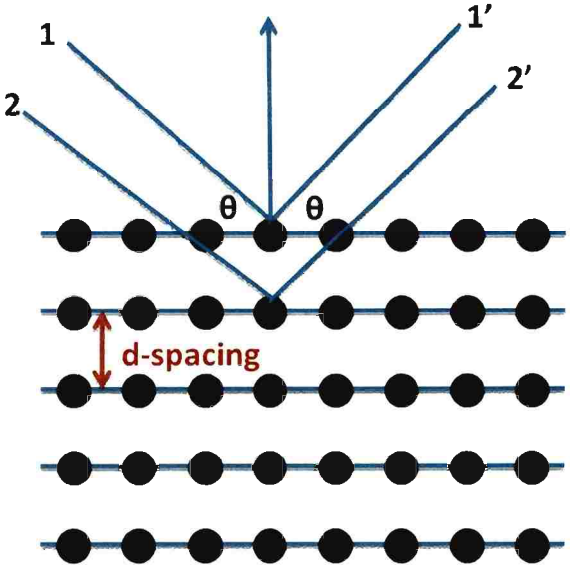

Figure 2.1. Schematic representation of Bragg's law.

In general, X-ray diffraction patterns are plots of intensity versus 2θ angle. Different planes in a crystal diffract at different angles giving a pattern which is unique to a crystal. The intensities of the reflections are determined by the distribution of the electrons in the unit cell. X-rays going through areas with high electron density will reflect strongly and areas with low electron density will give weak intensities. Therefore,

every crystalline material has a unique X-ray diffraction pattern that can be used to determine the crystallinity and phase of the deposited material.

Thin films deposited on polycrystalline substrates can be analyzed by running two types of experiments. In the first case, a symmetric scan (gonio scan) can be used to evaluate the out-of-plane texture of the film. It is a conventional θ-2θ scan for the Bragg-Brentano geometry. Figure 2.2 (A) shows a schematic representation of a gonio scan. Where, ω is the incident angle and θ is the diffracted angle. In a gonio scan, ω = θ and ω + θ = 2θ. Another way to characterize thin films is through glancing angle measurements, as shown in Figure 2.2 (B). In this case, ω + θ = 2θ and ω is fixed but θ varies. Glancing angle measurement is a good technique to measure polycrystalline grains. As the w is fixed and the θ is varied, all the planes in the material are brought into the Bragg condition. However, this technique cannot be used for highly oriented films or epitaxial films.

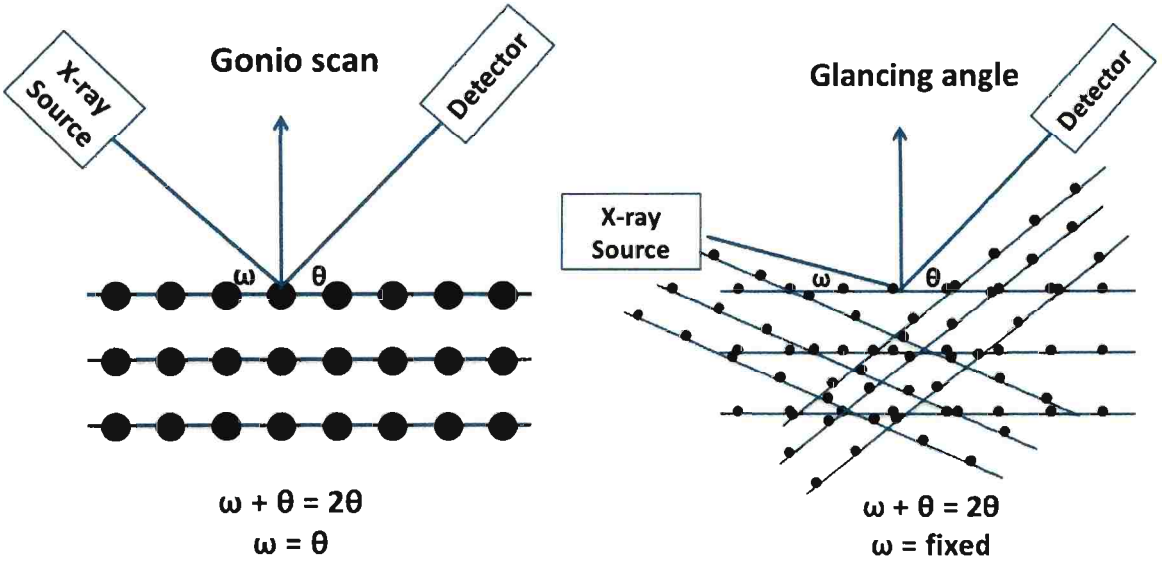

Figure 2.2. Schematic representation of (A) gonio scan used for textured films and (B) glancing angle used for polycrystalline grains.

Epitaxial films deposited on single crystals are oriented both out-of-plane as well as in-plane. In this case, X-ray characterization such as diffraction patterns, pole figures, azimuthal scans, and rocking curves are performed. Unlike polycrystalline films, epitaxial films grow with one orientation and show only a family of planes in the pattern.

In Figure 2.3, an epitaxial magnetite film deposited on a Ni(111) substrate shows only the {111} family peaks. The experimental setup to determine out-of-plane orientation is similar to the gonio scan but instead a 2θ-omega scan is run. The difference between this and the gonio scan is that there can be an offset between 2θ and omega, so that omega = ½ 2θ + offset. This is useful when collecting a diffraction scan from an epitaxial film, when the tilt of the film is compensated by the offset. Identification of the pattern is done by comparing the pattern with the existing patterns in the database. For example, a magnetite film is identified by JCPDS#19-0629 pattern. However, this does not provide any information about in-plane orientation of the film. To determine the in-plane orientation of the film, X-ray pole figures and azimuthal scans are run. Pole figures can be used to probe planes which are not parallel with the geometric surface of the sample. The sample is moved through a series of tilt angles, χ, and at each tilt angle the sample is rotated through azimuthal angle, φ, of 0 to 360°. Peaks occur in the pole figure when the Bragg condition is satisfied. During the experiment 2θ is fixed, which is normally the highest intensity peak of a randomly oriented powder diffraction pattern of the material. Figure 2.4 is a schematic representation of a pole figure measurement. Azimuthal scans can be considered as a cross-section of a pole figure. They are obtained when the measurement is carried out at a specific 2θ for only specific tilt angle, χ, and rotated azimuthally, φ, from 0 to 360°. Comparing the azimuthal scans at specific tilt angle for a substrate and a film, we can obtain the epitaxial relationships.

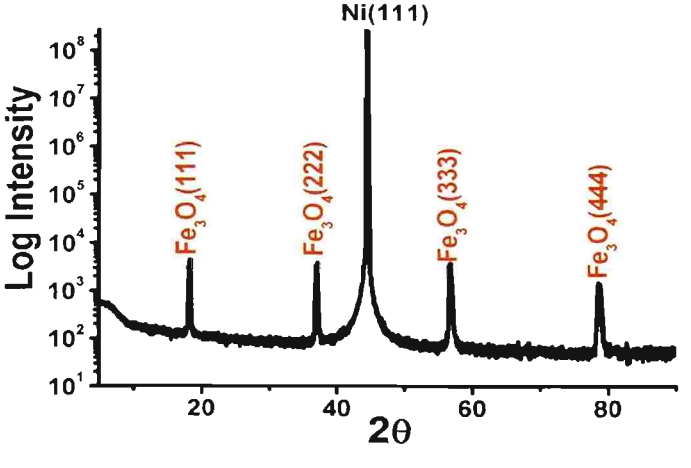

Figure 2.3. X-ray diffraction pattern of an epitaxial magnetite (Fe_3O_4) film on Ni(111) single crystal.[220]

To determine the quality of epitaxy, X-ray rocking curves are run. The rocking curves indicate the mosaic spread of the film relative to the substrate. The larger the full width at half maximum (FWHM), the larger the mosaic spread. In the experimental setup for a rocking curve, only the omega axis is scanned as data are collected. All other axes, such as 2θ, are fixed at specific angles. In a perfect single crystal, the FWHM is small indicating that all domains are aligned. The width of the rocking curve is a direct measurement of the range of orientation of the sample. In general, the rocking curves are performed for substrate as well as the film for comparison of mosaic spread. If the mosaic spread of the film is low and comparable to the substrate, the peaks in the pole figure become sharper and more intense. Rocking curves have been used to understand the in-plane misorientation of ZnO, AlN, and GaN on sapphire and MgO films grown on GaAs.[209]

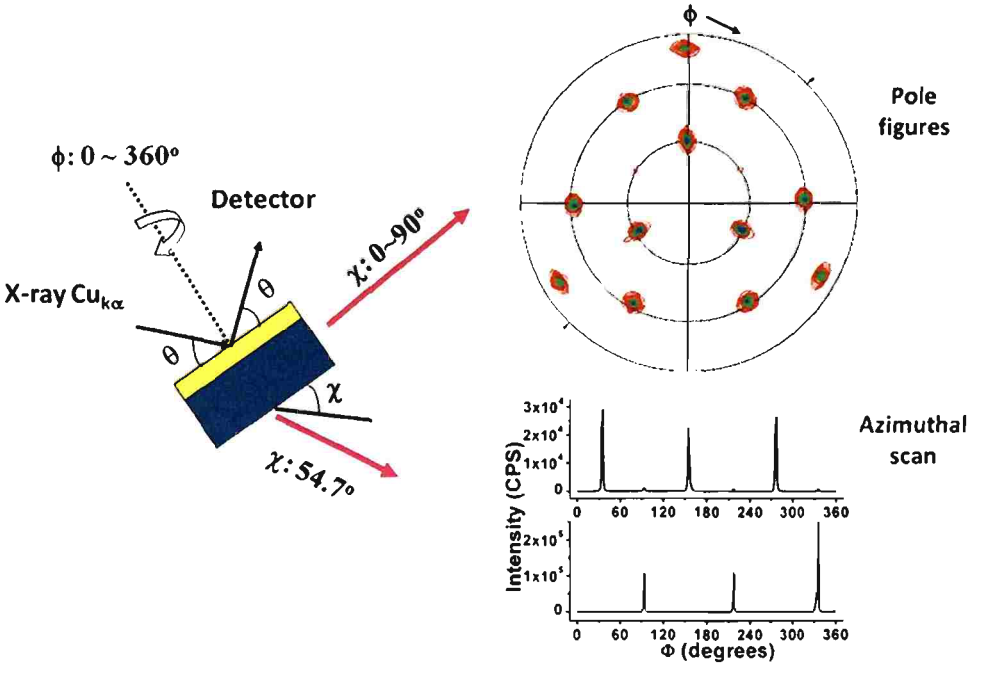

Figure 2.4. An illustration of the method to produce a (311) magnetite pole figure of a (111) oriented magnetite film on a Ni(111) substrate. The azimuthal scan on the bottom right is obtained by running the □ scan at a fixed χ.[220]

2.2.2 Scanning electron microscope (SEM) uses a focused high-energy electron beam to generate a variety of signals at the surface of solid specimens. The signals obtained from electron-sample interactions reveal information about the sample including external morphology, chemical composition, and crystalline structure and orientation of materials making up the sample.

The first SEM used to examine the surface of a solid specimen was described by Zworykin et al.[210] in 1942, working in the RCA laboratories in the United States. Since then there has been a lot of development and currently the world's highest SEM resolution at high beam energies (0.4 nm at 30 keV) is obtained with the Hitachi S-5500. In a SEM instrument, the electron gun produces a beam of electrons which are accelerated to a high energy state of about 0.2~40 eV. Accelerated electrons upon interaction with the sample generate secondary electrons, backscattered electrons, diffracted electrons, X-rays, visible light, and heat. Secondary electrons and backscattered electrons are commonly used for imaging samples: secondary electrons are most valuable for showing morphology and topography on samples and backscattered electrons are mostly used to find the contrasts in composition in multiphase samples. X-rays are produced by inelastic collisions of the incident electrons with electrons in different core shells of atoms in the sample. As the excited electrons return to lower energy states, they yield X-rays that are characteristic to a material.

Essential components of all SEMs include the following: 1) electron source (electron gun), (2) electron lenses, (3) sample stage, (4) detectors for all signals of interest, and (5) display data output devices. Figure 2.5 shows an illustration of all the components and a general working principle.

There are several advantages of using the SEM. The SEM is critical in all fields that require characterization of solid materials. Most SEMs are comparatively easy to operate, with user-friendly interfaces. However, samples must be solid and they must fit into the microscope chamber. For most instruments samples must be stable in a vacuum on the order of $10^{-5} - 10^{-6}$ torr. Energy-dispersive X-ray spectroscopy (EDS) detectors on SEMs cannot detect very light elements (H, He, and Li), and many instruments cannot detect elements with atomic number less than 11 (Na). An electrically conductive coating

is used in conventional SEMs, unless the instrument is capable of operating in a low vacuum mode.[211]

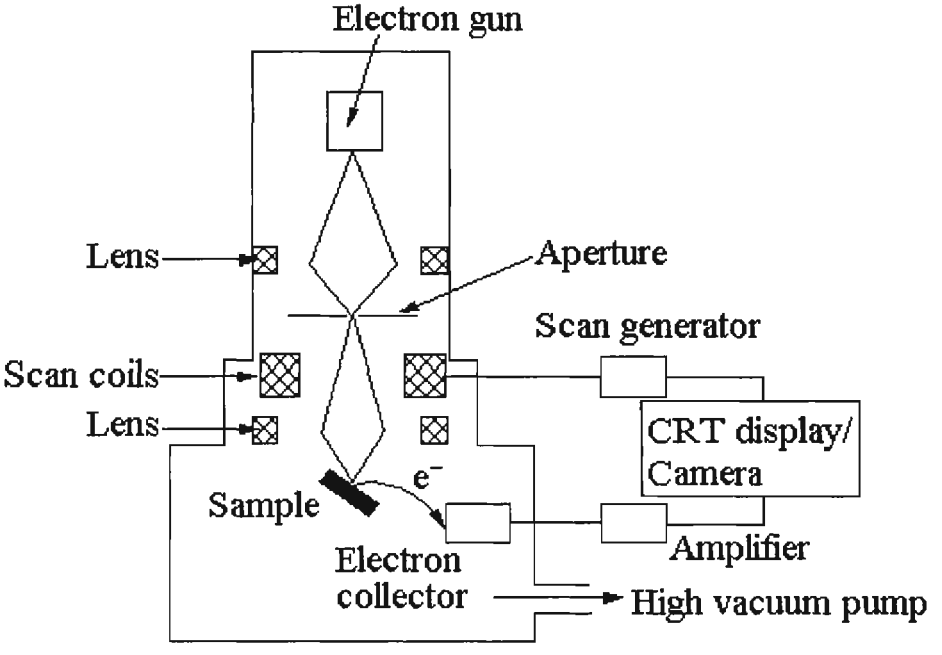

Figure 2.5. Illustration of a scanning lectron microscope[211]

2.2.3 Transmission electron microscope (TEM) uses a high voltage electron beam to create an image. The electrons interact with a very thin sample and only those that go past unobstructed hit the phosphor screen on the other side. At this point, the electrons are converted to light and an image or diffraction pattern is formed.

The dark areas of the image correspond to areas on the specimen where fewer electrons were able to pass through (either absorbed or scattered upon impact); the lighter areas are where electrons did pass through completely. TEMs are capable of imaging at a significant higher resolution than light microscopes, owing to the small de Broglie wavelength of electrons. This enables the user to examine fine detail, even as small as a single column of atoms.

Figure 2.6 illustrates the components of a typical TEM instrument. The gun in TEM is designed to create a beam of electrons, and usually can be divided into two categories: thermionic emission or field emission. In general, the sources used are tungsten and lanthanum hexaboride (LaB_6) for thermionic emission because of their higher melting temperature and low work function, respectively.

The thermionic emission current density, *J*, can be related to the work function of the emitting material and is a Boltzmann distribution given by the following equation.

$$J = AT^2 \exp(-\Phi/kT) \quad (1)$$

Where, J is the emitted current density, A is a Richardson's constant (A/m^2K^2), Φ is the work function, k is the Boltzmann's constant (8.5×10^{-5} eV/K) and T is the absolute temperature. The equation shows that in order to achieve sufficient current density it is necessary to heat the emitter, hence higher melting temperature material are used. To prevent thermal shock, there is often a delay enforced in the application of current to the tip, to prevent thermal gradients from damaging the filament. In contrast, the mechanism for field emission is much simpler. It follows a simple equation as shown below.

$$E = V/r \quad (2)$$

Where, E is electric field, V is the voltage applied and r is the radius at the point of voltage application. In field-emission guns electrons are generated in two steps. In the first step, the anode is positively charged by several kV with respect to the tip, followed by second anode accelerating electrons to 100 kV or more.

Lenses in the TEM may operate electrostatically or magnetically. Electromagnetic coils are used to generate a convex lens set up. In such lenses, the field produced must be symmetrical radially, as the deviation from radial symmetry of the magnetic lens causes aberrations such as astigmatism. There are several types of magnetic lenses in the TEM: condenser lens, objective lens, intermediate lens and projector lens. Each lens plays a different role. Condenser lens are utilized to illuminate the specimen with a parallel electron beam. Usually there are two condenser lenses, the second condenser lens controls the convergent angle of a beam leaving the condenser system, and then produces a focused beam on the specimen. The objective lens generates the image and diffraction patterns as a beam of electrons are scattered by the specimen. Intermediate and projector lens are used to magnify the images or diffraction patterns.

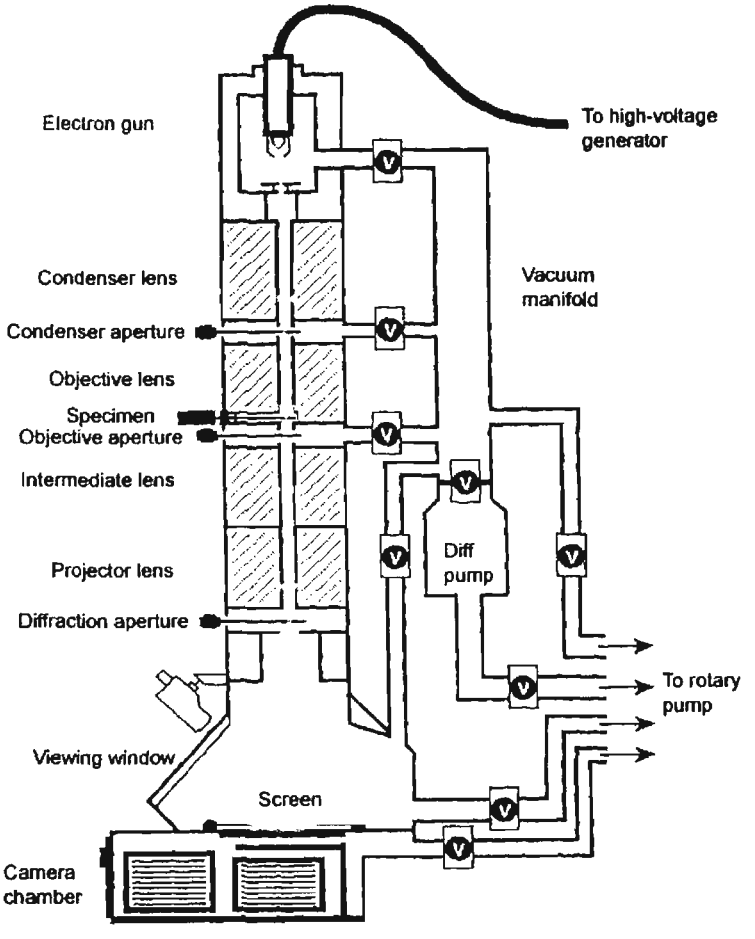

Figure 2.6. Schematic of a transmission electron microscope[212]

There are different imaging modes in TEM. In general, the most common types of imaging modes are: bright field, diffraction, electron energy loss spectroscopy (EELS), high resolution transmission electron microscopy (HRTEM), and three dimensional imaging. In this thesis, some of these techniques are used for characterizing the Fe_3O_4 films and superlattices in the magnetite/zinc ferrite system. In the bright field imaging mode, regions with higher atomic number will appear dark, while regions with low electron density appear bright. In diffraction imaging mode, the apertures are placed in the back focal plane, the desired Bragg reflections can be selected, and thus Kikuchi patterns are formed, if a crystalline material is being characterized. Such Kikuchi bands mark orientation space with well-defined intersections (called zones or poles) as well as paths connecting one intersection to the next. In the EELS technique, electrons are

selectively rejected based upon on their voltage, using a magnetic device known as an EELS spectrometer. EELS scans are used to determine different elements in the material. Finally, in the case of three dimensional imaging, multiple views of the same specimen can be obtained by rotating the angle of the sample along an axis perpendicular to the beam.[212]

Specimen preparation for TEM is a cumbersome process as the sample needs to be very thin (few hundreds of nanometers). TEM specimens can be prepared by several techniques or sometimes combinations of several techniques. Some of the sample preparation techniques are as follows: (1) mechanical milling, (2) chemical etching, (3) ion etching and (4) focused ion beam (FIB). All the TEM samples for our experiments were prepared using the focused ion beam technique. It is possible to micro machine samples very precisely using the FIB technique. FIB makes use of energetic gallium ions for milling the sample.

2.2.4 Magnetic characterization (PPMS): A 9T physical property measurement system (PPMS) from Quantum design is used to characterize electrical and magnetic properties of materials. This system allows measurements in a controlled temperature and magnetic field environment, with temperature ranging from 1.9-400 K and magnetic fields from 0-9T. The entire system is computer controlled, allowing programmed temperature, current, or field sweeps during a measurement. Its design combines many features in one instrument to make the PPMS the most versatile system of its kind. Some of the applications include: DC resistivity, AC transport (AC resistivity, Hall coefficient, iV curve, critical current), heat capacity, thermal transport (thermal conductivity, Seebeck coefficient), AC susceptibility, vibrating sample magnetometer (VSM), and torque magnetometer. Switzer's group has a PPMS purchased from Quantum Design, which has some of the above stated features.

Magnetic and electrical properties of polycrystalline and epitaxial films of magnetite, zinc ferrite and superlattices in magnetite/zinc ferrite system electrodeposited on polycrystalline and single crystalline substrates where characterized using the PPMS instrument. The resistance dependence on temperature, and magnetoresistance properties of films and superlattices were determined using the resistivity option on the PPMS.

Magnetic hysteresis loops, field-cooled and zero-field-cooled magnetization data for the films and superlattices were obtained using the VSM option on the PPMS.

The resistivity option can report resistance as well as resistivity, conductance, and conductivity for a material. Samples are mounted on standard PPMS sample pucks or on resistivity sample pucks. Resistivity sample pucks have four contacts, one positive and one negative contact for both current and voltage. For our experiments, the setup was slightly modified. Two contacts were made using In metal, one to the top of the film or superlattice and the other to the substrate. One of these contacts was soldered to the negative current and voltage and the other contact was soldered to the positive current and voltage. Even though the puck has a capability to hold three samples, only one sample was measured at a time.

For a resistance vs. temperature plot the temperature is gradually decreased from 300 K to 10 K at small steps, and at each temperature the resistance is measured. In the case of magnetoresistance measurements, the magnetic field was gradually increased and the resistance was measured at each magnetic field. Magnetoresistance is the property of a material to change the value of electrical resistance when an external magnetic field is applied. Magnetoresistance is defined as a ratio of change of resistance at an applied magnetic field (R_H) and at zero magnetic fields (R_O) to resistance at zero magnetic fields (R_O). It can be described by the following equation.

$$\% \text{ MR} = (R_H - R_O) / R_O \tag{3}$$

There are different kinds of magnetoresistance: anisotropic magnetoresistance (AMR), giant magnetoresistance (GMR), colossal magnetoresistance (CMR), and tunneling magnetoresistance (TMR). In the case of AMR, the direction of applied magnetic field with respect to the material influences the MR. The AMR effect is seen in materials because the origin of the MR effect lies in the spin orbit coupling. As the direction of magnetization rotates, the electron cloud about each nucleus deforms slightly, changing the amount of scattering of electrons. The GMR effect was first reported by Grünberg et al.[213] and Fert et al.[214] independently in 1988, in antiferromagnetically coupled multilayers of Fe/Cr. In these structures, thin layers of

magnetic metals are separated by layers of non-magnetic metals. The GMR effect requires that there is a way to change the relative orientations of the magnetization in adjacent magnetic metal layers, and the thickness of the films must be less than the mean free path of the electrons. CMR effect is generally observed in perovskite structures. In this case, the change of resistivity is in the order of tens of thousands ohm-cm. This effect was first seen by G. H. Jonker and J. H. van Santen[215] in 1950.

Magnetic hysteresis loops are obtained using the VSM option. Originally, VSM was developed by Foner.[216] The working principle of VSM is based on the Faraday's law of induction in which an electromotive force is induced by a time-varying magnetic flux. When the sample is vibrated with small fixed amplitude (A) in a magnetic field, the induced voltage (E) can be given by[217]

$$E = \sigma G A 2\pi f \cos(2\pi f t) \quad (4)$$

where, σ is the magnetic moment f the sample, G is a factor dependent upon the detection coil geometry, f is the vibration frequency and t is the time.

The magnetic hysteresis loops obtained through VSM provides detailed information about magnetization behavior for a given material, as shown in Figure 2.7. Several important properties can be obtained from a M-H loop. The saturation magnetization (M_s) is the maximum absolute value of measured magnetization M. The remanence (M_r) is defined as the magnetization retained in the material after removing the applied field. The coercivity (H_c) is the field above which a permanent magnetic moment can be sustained. The squareness ($S_r = M_r/M_s$) is an indication of the ability of a ferromagnetic material to retain magnetization after applied field is switched off.

Information of the energy barriers can be obtained by temperature-dependent magnetization data measured in zero-field-cooled (ZFC) and field-cooled (FC) procedures. In the case of ZFC magnetization curve, the sample is first cooled in a zero field from high temperature down to a low temperature. Then a magnetic field is applied and the magnetization as a function of temperature is measured in the warming process. In the FC magnetization curves, the magnetization data is obtained while cooling the sample to the low temperature in the same field. ZFC curves are the measure of

thermodynamic equilibrium states described by the Curie law. When the temperature is lowered, the system will try to approach the corresponding equilibrium state through relaxation process. When the temperature is increased, the relaxation rate increases exponentially and reaches an equilibrium value at a certain temperature, any further increase of temperature results in decreasing the magnetization following the Curie law.[218]

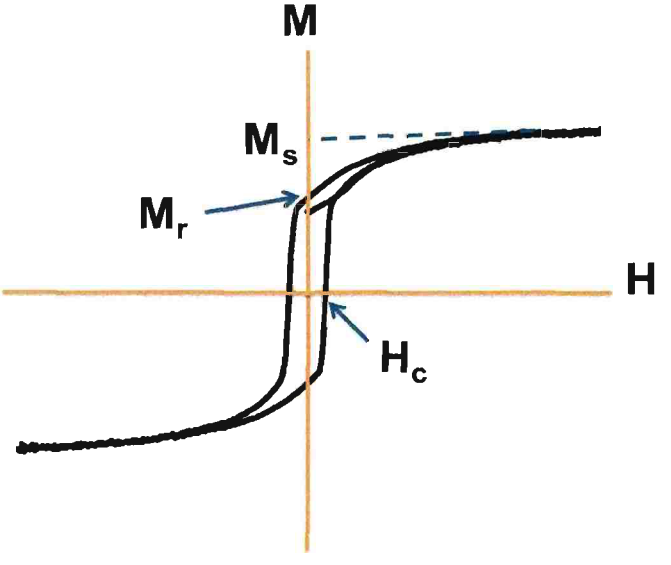

Figure 2.7. A typical hysteresis loop for a ferromagnetic material indicating the regions with information on the loop.

REFERENCES

1. U. Landau, "Plating-New Prospects for an Old Art", *Electrochemistry in Industry, New Directions,* Plenum Press, New York (1982).

2. J. W. Dini, *Electrodeposition: the materials science of coating and substrate*, Noyes publications, New Jersey (1993).

3. W. Obretenov, U. Schmidt, W. J. Lorenz, G. Staikov, E. Budevski, D. Carnal, U. Muller, H. Siegenthaler, and E. Schmidt, *J. Electrochem. Soc.,* **140**, 692 (1993).

4. H. Bort, K. Juttner, W. J. Lorenz, G. Staikov, and E. Budevski, *Electrochim Acta.*, **28**, 985 (1983).

5. R. J. Phillips, M. J. Shane, and J. A. Switzer, *J. Mater. Res.,* **4**, 923 (1989).

6. E. Budevski, G. Staikov and W.J. Lorenz. In: *Electrochemical phase formation and growth*, VCH, Weinheim, 149 (1996).

7. H.D. Merchant, Defect structure of electrodeposits. In: H.D. Mercahnt, Editor, Defect structure, morphology and properties of deposits, TMS Publication, Warrendale (PA), 1–59 (1995).

8. F. Ebrahimi and Z. Ahmed, *Materials Characterization*, **49**, 373 (2003).

9. R. Liu, F. Oba, E. W. Bohannan, F. Ernst, and J. A. Switzer, *Chem. Mater.,* **15**, 4882 (2003).

10. N. Fenineche, A. M. Chaze, and C. Coddet, *Surf. Coat. Technol.,* **88**, 264 (1997).

11. S. M. S. I. Dulal, H. J. Yun, C. B. Shin, and C. –K. Kim, *Electrochim. Acta*, **53**, 934 (2007).

12. J. A. Switzer, H. M. Kothari, and E. W. Bohannan, *J. Phys. Chem. B*, **106**, 4027 (2002).

13. H. Fischer, *Electrodepos. Surface Treatment,* **I**, 239, 319 (1972/73).

14. T. C. Franklin, *Surf. Coat. Technol.*, **30**, 415 (1987).

15. L. Oniciu and L. Muresan, *J. Appl. Electrochem.,* **21**, 565 (1991).

16. T. C. Franklin, *Plat. Surf. Finish.,* **81**, 62 (1994).

17. R. Q. Hwang and R. J. Behm, *J. Vac. Sci. Technol. B,* **10**, 256 (1992).

18. H. Brune, *Surf. Sci. Rep.*,31, **121**, (1998).

19. M. Bott, T. Michely, and G. Cosma, *Surf. Sci.*, **272**, 161 (1992).

20. S. Morin, A. Lachenwitzer, O. M. Magnussen, and R. J. Behm, *Phys. Rev. Lett.*, **83**, 5066 (1999).

21. F. Ebrahimi and Z. Ahmed, *J. Appl. Electrochem.*, **33**, 733 (2003).

22. S. Riemer, J. Gong, M. Sun, and I. Tabakovic, *J. Electrochem. Soc.*, **156**, D439 (2009).

23. D. Josell, D. Wheeler, W. H. Huber, and T. P. Moffat, *Phys. Rev. Letts.*, **87**, 016102 (2001).

24. E. B. Svedberg, J. J. Mallett, S. Sayan, A. J. Shapiro, J. Alexander, W. F. Egelhoff, and T. Moffat, *App. Phys. Letts.*, **85**, 1353 (2004).

25. J. L. Stojak, J. Frasner, and J. B. Talbot, *Advances in Electrochemical Science and Engineering*,**7**, 193 (2001).

26. J. A. Switzer, *Am. Ceram. Soc. Bull.*, **66**, 1521 (1987).

27. J. Feng and D. C. Johnson, *J. Electrochem. Soc.*, **137**, 506 (1990).

28. B. E. Breyfogle, R. J. Philips, and J. A. Switzer, *Chem. Mater.*, **4**, 1356 (1992).

29. J. L. Stickney, Advancces in Electrochemical Science and Engineering, 7, 1 (2001).

30. K. Rajeshwar, *Adv. Mater.*, **4**, 23 (1992).

31. J. L. Stickney, *Electroanal. Chem.*, **21**, 75 (1999).

32. G. Hodes and I. Rubinstein, *Electrochemistry of Nanomaterials*, Wiley-VCH, Weinheim, Germany, 25-66 (2001).

33. J. A. Switzer, M. J. Shane, and R. J. Phillips, *Science*, **247**, 444 (1990).

34. J. A. Switzer, R. P. Raffaelle, R. J. Phillips, C. J. Hung, and T. D. Golden, *Science*, **258**, 1918 (1992).

35. J. A. Switzer, C. J. Hung, B. E. Breyfogle, M. G. Shumsky, R. Van Leeuwen, and T. D. Golden, *Science*, **264**, 1573 (1994).

36. T. P. Moffat, *J. Electrochem. Soc.*, **142**, 3767 (1995).

37. E. A. Kulp and J. A. Switzer, *J. Am. Chem. Soc.*, **129**, 15120 (2007).

38. M. L. Norton, *Mater. Res. Bull.*, **24**, 1391 (1989).

39. R. O. Borges and D. Lincot, *J. Electrochem. Soc.*, **140**, 3464 (1993).

40. P. K. Nair, M. T. S. Nair, V. M. Garcia, O. L. Arenas, Y. Pena, A. Castillo, I. T. Ayala, O. Gomezdaza, A. Sanchez, J. Campos, H. Hu, R. Suarez, and M. E. Rincon, *Sol. Energ Mat. Sol C*, **52**, 313 (1998).

41. D. Smith, Thin-Film Deposition: Principles and Practice, MacGraw-Hill (1995).

42. R. C. Jaeger, "Film Deposition". *Introduction to Microelectronic Fabrication*, ISBN 0-201-44494-7, Upper Saddle River: Prentice Hall (2002).

43. A. Anders, Editor, Handbook of plasma Immersion Ion implantation and Deposition, New York: Wiley-Interscience (2000).

44. M. A. Herman, and H. Sitter, Editors, *Molecular Beam Epitaxy- Fundamentals and Current Status,* Springer-Verlag, Berlin (1989).

45. M. Antaya, J. R. Dahn, J. S. Preston, E. Rossen, and J. N. Reimers, *J. Electrochem. Soc.,* **140**, 575 (1993).

46. L. L. Hench, J. K. West, *Chem. Rev.*, **90**, 33 (1990).

47. D. Edelstein, J. Heidenreich, R. Goldblatt, W. Cote, C. Uzoh, N. Lusting, P. Roper, T. McDevitt, W. Motsiff, A. Simon, J. Dukovic, R. Wachnik, H. Rathore, R. Schulz, L. Su, S. Luce, and J. Slattery, *IEEE IEDM*, **97**, 31.3.1 (1997).

48. T. P. Moffat and L. –Y. Ou Yang, *J. Electrochem. Soc.,* **157**, D228 (2010).

49. R. Akolkar and U. Landau, *J. Electrochem. Soc.,* **151**, C702 (2004).

50. J. Hu and M. –F. Yu, *Science*, **329**, 313 (2010).

51. J. A. Switzer and G. Hodes, *MRS Bulletin*, **35**, 743 (2010).

52. F. Y. Yang, K. Liu, K. Hong, D. H. Reich, P. C. Searson, and C. L. Chien, *Science*, **284**, 1335 (1999).

53. M. Alper, K. Attenborough, R. Hart, S. J. Lane, D. S. Lashmore, C. Younes, and W. Schwarzacher, *Appl. Phys. Lett.*, **63**, 2144 (1993).

54. R. Müller, O. Rouault, A. Katzenmeyer, L. Goux, D. J. Wouters, J. Genoe, and P. Heremans, *Phil. Trans. R. Soc.*, **367**, 4191 (2009).

55. J. A. Switzer, E*lectrochemistry of Nanomaterials,* G. Hodes, Ed. (Wiley-VCH, Weinheim, 2001) chap 3.

56. J. A. Switzer, *Handbook of Nanophase Materials,* A. Goldstein, Ed. (Marcel Dekkar, New York, 1996) chap 4.

57. M. Hong, S. Wolf, D. c. Gubser, Eds. *Metallic Multilayers and Epitaxy* (Metllurgical Society, USA, 1988).

58. L. L. Chang, B. C. Giessen, Eds. *Synthetic Modulated Structures* (Academic, Orlando, 1985).

59. J. A. Switzer, H. M. Kothari, P. Poizot, S. Nakanishi, and E. W. Bohannan, *Nature*, **425**, 490 (2003).

60. H. M. Kothari, E. A. Kulp, S. Boonsalee, M. P. Nikiforov, E. W. Bohannan, P. Poizot, S. Nakanishi, and J. A. Switzer, *Chem. Mater.*, **16**, 4232 (2004).

61. S. K. Sarkar, N. Burla, E. W. Bohannan, and J. A. Switzer, *J. Am. Chem. Soc.*, **129**, 8972 (2007).

62. S. K. Sarkar, N. Burla, E. W. Bohannan, and J. A. Switzer, *Electrochem. Acta,* **53**, 6191 (2008).

63. R. Liu, E. W. Bohannan, J. A. Switzer, F. Oba, and F. Ernst, *Appl. Phys. Lett.*, **83**, 1944 (2003).

64. R. Liu, F. Oba, E. W. Bohannan, F. Ernst, and J. A. Switzer, *Chem. Mater.*, **15**, 4882 (2003).

65. R. Liu, E. A. Kulp, F. Oba, E. W. Bohannan, F. Ernst, and J. A. Switzer, *Chem. Mater.*, **17**, 725 (2005).

66. T. A. Sorenson, S. A. Morton, D. G. Waddill, and J. A. Switzer, *J. Am. Chem. Soc.*, **124**, 7604 (2002).

67. H. M. Kothari, E. A. Kulp, S. J. Limmer, P. Poizot, E. W. Bohannan, and J. A. Switzer, *J. Mater. Res.*, **21**, 293 (2006).

68. S. Mitra, P. Poizot, A. Finke, J. –M. Tarascon, *Adv. Funct. Mater.*, **16**, 2281 (2006).

69. E. A. Kulp, H. M. Kothari, S. J. Limmer, J. Yang, R. V. Gudavarthy, E. W. Bohannan, and J. A. Switzer, *Chem. Mater.*, **21**, 5022 (2009).

70. J. A. Switzer, M. G. Shumsky, and E. W. Bohannan, *Science*, **284**, 293 (1999).

71. E. W. Bohannan, C. C. Jaynes, M. G. Shumsky, J. K. Barton, and J. A. Switzer, *Solid State Ionics,* **131**, 97 (2000).

72. E. A. Kulp, S. J. Limmer, E. W. Bohannan, and J. A. Switzer, *Solid State Ionics,* **178**, 749 (2007).

73. B. E. Breyfogle, C. J. hung, M. G. Shumsky, and J. A. Switzer, *J. Electrochem. Soc.*, **143**, 2741 (1996).

74. J. A. Switzer, *J. Electrochem. Soc.*, **133**, 722 (1986).

75. R. A. van Leeuwen, C. –J. Hung, D. R. Kammler, and J. A. Switzer, *J. Phys. Chem.*, **99**, 15247 (1995).

76. A. A. Vertegel, E. W. Bohannan, M. G. Shumsky, and J. A. Switzer, *J. electrochem. Soc.*, **148**, C253 (2001).

77. Y. Zhou, R. J. Phillips, and J. A. Switzer,*J. Am. Ceram. Soc.*, **78**, 981 (1995).

78. J. A. Switzer, *Ceram. Bull.*, **66**, 1521 (1987).

79. S. J. Limmer, E. A. Kulp, E. W. Bohannan, and J. A. Switzer, *Langmuir*, **22**, 10535 (2006).

80. J. A. Switzer and R. J. Phillips, *J. Mater. Res. Soc. Symp. Proc.*, **121**, 111 (1988).

81. R. Liu, A. A. Vertegel, E. W. Bohannan, T. A. Sorenson, and J. A. Switzer, *Chem. Mater.*, **13**, 508 (2001)

82. S. Peulon and D. Lincot, *Adv. Mater.*, **8**, 166 (1996).

83. S. Peulon and D. Lincot, *J. Electrochem. Soc.*, **145**, 864 (1998).

84. P. Poizot, C. –J. Hung, M. P. Nikiforov, E. W. Bohannan, and J. A. Switzer, *Electrochem. Solid-State Lett.*, **6**, C21 (2003).

85. K. Nakaoka and K. Ogura, *J. Electrocrochem. Soc.*, **149**, C579 (2002).

86. C. A. Ross, *Ann. Rev. Mater. Sci.*, **24**, 159 (1994).

87. W. Schwarzacher and D. S. Lashmore, *IEEE Trans. Magn.*, **32**, 3133 (1996).

88. M. Alper, W. Schwarzacher, and S. J. Lane, *J. Electrochem. Soc.*, **144**, 2346 (1997).

89. D. Simmunovich, M. Schlesinger, and D. D. Synder, *J. Electrochem. Soc.*, **141**, L10 (1994).

90. S. K. Ghosh, P. K. Limaye, B. P. Swain, N. L. Soni, R. G. Agarwal, R. O. Dusane, A. K. Grover, *Surf. Coatings Technol.*, **201**, 4609 (2007).

91. D. S. Lashmore and M. P. Dariel, *J. electrochem. Soc.*, **135**, 1218 (1988).

92. T. Moffat, *J. Electrochem. Soc.*, **142**, 3767 (1995).

93. D. Tench and J. White, *J. Electrochem. Soc.*, **137**, 3061 (1990).

94. C. Ogden, Plating Surface Finishing, **5**, 130 (1986).

95. J. Yahalom and O. Zadok, *J. Mater. Sci.,* **22**, 499 (1987).

96. A. Tokarz, A. Wolkenberg, and T. Przeslawski, *J. Electrochem. Soc.,* **149**, C607 (2002).

97. A. Brenner, *Electrodeposition of Alloys;* Academic Press: New York, **2**, 589 (1963).

98. A. R. Bachmann, A. Mugarza, J. E. Ortega, and S. Speller, *Phys. Rev. B*, **64**, 153409 (2001).

99. F. Tsui, B. Chen, J. Wellman, C. Uher, and R. Clarke, *J. Appl. Phys.,* **81**, 4586 (1997).

100. W. Kim and R. Weil, *Surf. Coat. Technol.*, **31**, 143 (1987).

101. P. Boher, P. Houdy, C. Schiller, and L. J. Ijzendoorn, *Thin Solid films,* **174**, 91 (1989).

102. G. Barral and S. Maximovitch, *Coloque de Phys.*, **C4**, 291 (1990).

103. L. M. Goldman, C. A. Ross, W. Ohash, D. Wu, and F. Spaepen, *Appl. Phys. Lett.,* **55**, 2182 (1989).

104. E. G. Bauer, B. W. Dodson, D. J. Ehrlich, L. C. Feldman, C. P. Flynn, M. W. Geis, J. P. Harbison, R. Matyi, P. S. Peercy, P. M. Petroff, J. M. Phillips, G. B. Stringfellow, and A. Zangwill, *J. Mater. Res.*, **5**, 852 (1990).

105. M. A. Herman, and H. Sitter, Editors, *Molecular Beam Epitaxy-Fundamentals and Current Status*, Springer-Verlag, Berlin (1989).

106. B. A. Joycee, *Rep. Prog. Phys.,* **48**, 1637 (1985).

107. A. Y. Cho, and J. R. Arthur, Prog. *Solid state Chem.*, **10**, 157 (1975).

108. T. Fujii, Y. Nakata, S. Muto, and S. Hiyamizu, *Jpn. J. Appl. Phys.*, **25**, L598 (1986).

109. E. Budevski, G. Staikov, W. J. Lorenz, Electrochemical Phase Formation and Growth: An Introduction to the Initial Stages of Metal Deposition, Wiley-VCH, Weinheim, Germany, (1996).

110. E. S. Machlin, Materials Science in MicroelectronicsI: The relationships between thin film processing and structure, Elsevier, 2005.

111. T. Fujii, D. Alders, F. C. Voogt, T. Hibma, B. T. Thole, and G. A. Sawatzky, *Surf. Science*, **366**, 579 (1996).

112. S. Nakanishi, G. Lu, H. M. Kothari, E. W. Bohannan, and J. A. Switzer, *J. Am. Chem. Soc.*, **125**, 14998 (2003).

113. G. Mu, R. V. Gudavarthy, E. A. Kulp, and J. A. Switzer, *Chem. Mater.*, **21**, 3960 (2009).

114. V. Srikanth, J. S. Speck, and D. R. Clarke, *J. Appl. Phys.*, **82**, 4286 (1997).

115. M. A. Herman, and H. Sitter, Editors, *Molecular Beam Epitaxy-Fundamentals and Current Status*, Springer-Verlag, Berlin (1989).

116. G. Staikov, E. Budevski, W. Obretenov, K. Jüttner, and W. J. Lorenz, *Surf. Sci.*, **248**, 234 (1991).

117. W. Obretenov, U. Schmidt, W. J. Lorenz, G. Staikov, E. Budevski, D. Carnal, U. Müller, H. Siegenthaler, and E. Schmidt, *J. Electrochem. Soc.*, **140**, 692 (1993).

118. T. C. Hsieh and T. C. Chiang, *Surf. Sci.*, **166**, 554 (1986).

119. T. Miller, A. Samsavar, G. E. Franklin, and T. C. Chiang, *Phys. Rev. Lett.*, **61**, 1404 (1988).

120. K. Jüttner, W. J. Lorenz, G. Staikov, and E. Budevski, *Electrochim. Acta*, **23**, 741 (1978).

121. N. Batina, T. Will, and D. W. Kolb, *Faraday Disc.*, **94**, 93 (1992).

122. T. P. Moffat, *J. Electrochem. Soc.*, **142**, 3767 (1995).

123. R. Liu, A. A. Vertegel, E. W. Bohannan, and T. A. Sorenson, *Chem. Mater.*, **13**, 508 (2001).

124. S. Boonsalee, R. V. Gudavarthy, E. W. Bohannan, and J. A. Switzer, *Chem. Mater.*, **20**, 5737 (2008).

125. H. M. Kothari, A. A. Vertegel, E. W. Bohannan, and J. A. Switzer, *Chem. Mater.*, **14**, 2750 (2002).

126. R. J. Phillips, T. D. Golden, M. G. Shumsky, E. W. Bohannan, and J. A. Switzer, *Chem. Mater.*, **9**, 1670 (1997).

127. J. A. Switzer, and T. D. Golden, *Adv. Mater.*, **5**, 474 (1993).

128. P. Allongue, and E. Souteyrand, *J. Vac. Sci. & Tech .B*, **5**, 1644 (1987).

129. D. Lincot, A. Kampmann, B. Mokili, J. Vedel, R. Cortes, and M. Forment, *Appl. Phys. Lett.*, **67**, 2355 (1995).

130. Th. Pauporte, and D. Lincot, *Appl. Phys. Lett.*, **75**, 3817 (1999).

131. J. C. Ziegler, G. Scherb, O. Bunk, J. Zegenhagen, and D. M. Kolb, *Electrochim. Acta.*, **45**, 4599 (2000).

132. J. C. Ziegler, G. Scherb, O. Bunk, A. Kazimirov, L. X. Cao, D. M. Kolb, R. L. Johnson, and J. Zengenhagen, *Surf. Sci.*, **452**, 150 (2000).

133. L. Beaunier, H. Cachet, R. Cortes, M. Froment, *J. Electroanal. Chem.*, **532**, 215 (2002).

134. J. W. Shin, A. Standley, and E. Chason, *Appl. Phys. Lett.*, **90**, 261909 (2007).

135. J. Åkerman, *Science*, **308**, 508 (2005).

136. S. Parkin, X. Jiang, C. Kaiser, A. Panchula, K. Roche, and M. Samant, *Proc. IEEE*, **91**, 661 (2003).

137. R. Bez, E. Camerlenghi, A. Modelli, and A. Visconti, *Proc. IEEE*, **91**, 489 (2003).

138. H. F. Hamann, M. O'Boyle, Y. C. Martin, M. Rooks, and K. Wickramasinghe, *Nat. Mater.*, **5**, 283 (2006).

139. J. Junquera, and P. Ghosez, *Nature*, **422**, 506 (2003)

140. W. W. Zhuang, W. Pan, B. D. Ulich, J. J. Lee, L. Stecker, A. Bumaster, D. R. Evans, S. T. Hsu, M. Tajin, A. Shimaoka, K. Inoue, T. Naka, N. Awaya, K. Sakiyama, Y. Wang, S. Q. Liu, N. J. Wu, and A. Ignateiv, *Tech. Dig. IEDM*, 193, 2002.

141. I. G. Baek, M. S. Lee, S. Seo, M. J. Lee, D. H. Seo, D.-S. Suh, J. C. Park, S. O. Park, H. S. Kim, I. K. Yoo, U. –I. Chung, and J. T. Moon, *Tech. Dig. IEDM*, 587, 2004.

142. A. Sawa, *Mater. Today*, **11**, 28 (2008).

143. K. Tsubouchi, I. Ohkubo, H. Kumigashira, M. Oshima, Y. Matsumoto, K. Itaka, T. Ohnishi, M. Lippmaa, and H. Koinuma, *Adv. Mater.* , **19**, 1711 (2007).

144. I. G. Baek, D. C. Kim, M. J. Lee, H.-J. Kim, E. K. Yim, M. S. Lee, J. E. Lee, S. E. Ahn, S. Seo, J. H. Lee, J. C. Park, Y. K. Cha, S. O. Park, H. S. Kim, I. K. Yoo, U.-I. Chung, J. T. Moon, and B. I. Ryu, *IEDM Tech. Dig.*, 769, 2005.

145. R. Müller, R. Naulaerts, J. Billen, J. Genoe, and P. Heremans, *Appl. Phys. Lett.*, **90**, 063503 (2007).

146. L. Ma, S. Pyo, J. Ouyang, Q. Xu, and Y. Yang, *Appl. Phys. Lett.*, **82**, 1419 (2003).

147. T. W. Hickmott, *J. Appl. Phys.*, **33**, 2669 (1962).

148. T. J. Burch, P. P. Craig, C. Hendrick, T. A. Kitchens, J. I. Budnick, J. A. Cannon, M. Lipsicas, and D. Mattis, *Phys. Rev. Lett.*, **23**, 1444 (1969).

149. P. J. Freud, and A. Z. Hed, *Phys. Rev. Lett.*, **23**, 1440 (1969).

150. J. G. Simmons and R.R. Verderber, *Proc. R. Soc. London*, **301**, 77 (1967)

151. J. F. Gibbons, and W. E. Beadle, *Solid-state Electron.*, **7**, 785 (1964)

152. S. Q. Liu, N. J. Wu, and A. Ignatiev, *Appl. Phys. Lett.*, **76**, 2749 (2000).

153. A. Beck, J. G. Bednorz, Ch. Gerber, C. Rossel, and D. Widmer, *Appl. Phys. Lett.*, **77**, 139 (2000).

154. Y. Watanabe, J. G. Bednorz, A. Bietisch, Ch. Gerber, D. Widmer, A. Beck, and S. J. Wind, *Appl. Phys. Lett.*, **78**, 3738 (2001).

155. A. Baikalov, Y. Q. Wang, B. Shen, B. Lorenz, S. Tsui, Y. Y. Sun, Y. Y. Xue, and C. W. Chu, Appl. Phys. Lett., 83, 957 (2003).

156. B. J. Choi, D. S. Jeong, S. K. Kim, C. Rhode, S. Choi, J. H. Oh, H. J. Kim, C. S. Hwang, K. Szot, R. Waser, B. Reichenberg, and S. Tiedke, *J. Appl. Phys.*, **98**, 033715 (2005).

157. A. Chen, S. Haddad, Y. –C. Wu, T. –N. Fang, Z. Lan, S. Avanzino, S. Pangrle, M. Buynoski, M. Rathor, W. Cai, N. Tripsas, C. Bill, M. VanBuskirk, and M. Taguchi, *Tech. Dig. IEDM*, 746 (2005).

158. K. Fujiwara, T. Nemoto, M. J. Rozenberg, Y. Nakamura, and H. Takagi, *Jpn. J. Appl. Phys.*, **47**, 6266 (2008).

159. J. Yao, L. Zhang, Z. Zhang, T. He, Z. Jin, P. J. Wheeler, D. Natelson and J. M. Tour, *small*, 5, 2910 (2009).

160. C.-Y. Lin, C. –Y. Wu, C. –Y. Wu, T. –C. Lee, F. –L. Yang, C. Hu, and T. –Y. Tseng, *IEEE elec. Dev. Let.*, **28**, 0741 (2007).

161. A. Sawa, T. Fujii, M. Kawasaki, and Y. Tokura, *Appl. Phys. Lett.*, **85**, 4073 (2004).

162. T. Fujii, M. Kawasaki, A. S. Akoh, Y. Kawazoe, and Y. Tokura, *Appl. Phys. Lett.*, **86**, 012107 (2005).

163. A. Sawa, T. Fujii, M. Kawasaki, and Y. Tokura, *Jpn. J. Appl. Phys.*, **44**, L1241 (2005).

164. K. Kinoshita, T. Tamura, M. Aoki, Y. Sugiyama, and H. Tanaka, *Appl. Phys. Lett.*, **89**, 103509 (2006).

165. K. M. Kim, B. J. Choi, and C. S. Hwang, *Appl. Phys. Lett.,* **90**, 242906 (2007).

166. S. Tsui, A. Baikalov, J. Cmaidalka, Y. Y. Sun, Y. Q. Wang, Y. Y. Xue, C. W. Chu, L. Chen, and A. J. Jacobson, *Appl. Phys. Lett.*, **85**, 317 (2004).

167. X. Chen, N. J. Wu, J. Strozier, and A. Ignatiev, *Appl. Phys. Lett.*, **87**, 233506 (2005).

168. S. H. Jeon, B. H. Park, J. Lee, B. Lee, and S. Han, *Appl. Phys. Lett.*, **89**, 042904 (2006).

169. M. J. Rozenberg, I. H. Inoue, and M. J. Sanchez, *Appl. Phys. Lett.*, **88**, 033510 (2006).

170. R. Fors, S. I. Khartsev, and A. M. Grishin, *Phys. Rev. B*, **71**, 045305 (2005).

171. M. J. Rozenberg, I. H. Inoue, and M. J. Sanchez, *Phys. Rev. Lett.*, **92**, 178302 (2004).

172. S. Lee, A. Fursina, J. T. Mayo, C. T. Yavuz, V. L. Colvin, R. G. S. Sofin, I. V. Shvets, D. Natelson, *Nat. Mater.*, **7**, 130 (2008).

173. A. A. Fursina, R. G. S. Sofin, I. V. Shvets, and D. Natelson, *Phys. Rev. B*, **79**, 245131 (2009).

174. J. A. Switzer, R. V. Gudavarthy, E. A. Kulp, G. Mu, Z. He, and A. Wessel, *J. Am. Chem. Soc.*, **132**, 1258 (2010).

175. T. J. Burch, P. P. Craig, C. Hendrick, T. A. Kitchens, J. I. Budnick, J. A. Cannon, M. Lipsicas, D. Mattis, Phys. Rev. Lett. 1969, 23, 1444.

176. P. J. Freud, A. Z. Hed, Phys. Rev. Lett. 1969, 23, 1440.

177. R. J. Harrison, R. E. Dunin-Borkowski, and A. Putins, *PNAS*, **99**, 16556 (2002).

178. D. McKie, and C. McKie, *Crystalline Solids*, Walton-on-Thames, Surrey: Thomas Nelson and Sons, Ltd. (1974).

179. S. B. Ogale, K. Ghosh, R. P. Sharma, R. L. Greene, R. Ramesh, and T. Venkatesan, *Phys. Rev. B*, **57**, 7823 (1998).

180. M. J. D. Coey, A. E. Berkowitz, L. Barcells, F. F. Putris, and F. T. Parker, *Appl. Phys. Lett.,* **72**, 734 (1998).

181. Z. Zhang, and S. Satpathy, *Phys. Rev. B*, **44**, 13319 (1991).

182. E. J. W. Verwey, *Nature*, **144**, 327 (1939).

183. E. J. W. Verwey, and P. W. Haayman, *Physica*, **8**, 979 (1941).

184. E. J. W. Verwey, P. W. Haayman, and P.C. Romeijin, *J. Chem. Phys.*, **15**, 181 (1947).

185. J. Yoshida, and S. Iida, *J Phys. Soc. Jap.*, **47**, 1627 (1979).

186. R. M. Cornell, U. Schwetmann, The Iron oxides: Structure, Properties, Reactions, Occurrences and Uses, Wiley: Weinheim, 1996.

187. Y. S. Debkov, U. Rudiger, and G. Guntherodt, *Phys. Rev. B*, **65**, 064417 (2002).

188. J. J. Versluijis, M. A. Bari, and J. M. D. Coey, *Phys. Rev. Lett.*, **87**, 026601 (2001).

189. V. V. Girdin, G. R. Hearne, and H. M. Honig, *Phys. Rev. B*, **53**, 15518 (1996).

190. G. Q. Gong, A. Gupta, G. Xioa, Q. Qian, and V. P. Dravid, *Phys. Rev. B*, **56**, 5096 (1997).

191. X. W. Li, A. Gupta, G. Xioa, and G. Q. Gong, *J. Appl. Phys. B*, **83**, 7049 (1998).

192. D. T. Margulies, F. T. Parker, F. E. Spada, R. S. Goldman, J. Li, R. Sinclair, and A. E. Berkowitz, *Phys. Rev. B*, **53**, 9175 (1996).

193. H. Liu, E. Y. Jiang, H. L. Bai, R. K. Zheng, H. L. Wei, and X.X. Zhang, *Appl. Phys. Lett.*, **83**, 3531 (2003).

194. J. P. Hong, S. B. Lee, Y. W. Jung, J. H. Lee, S. K. Yoon, K. W. Kim, O. C. Kim, C. H. Lee, and M. H. Jung, *Appl. Phys. Lett.*, **83**, 1590 (2003).

195. J. B. Yang, X. D. Zhou, W. B. Yelon, W. J. James, Q. Cai, K. V. Gopalakrishnan, S. K. Malik, X. C. Sun, and D. E. Nilkes, *J. Sppl. Phys.*, **85**, 7540 (2004).

196. J. M. D. Coey, A. E. Berkowitz, L. Barcells, F. F. Putris, and F. T. Parker, *Appl. Phys. Lett.*, **72**, 734 (1998).

197. S. C. Stinson, *Chem. Eng. News*, **79**, 79 (2001).

198. M. Jacoby, *Chem. Eng. News*, **82**, 37 (2004).

199. Y. Orito, S. Imai, and G. Nyugen, *Synth. Org. Chem. Jpn.*, **37**, 173 (1979).

200. Y. Izumi, *Adv. Catal.*, **32**, 215 (1994).

201. C. F. McFadden, P. S. Cremer, and A. J. Gellman, *Langmuir*, **12**, 2483 (1996).

202. G. A. Attard, *J. Phys. Chem. B*, **105**, 3158 (2001).

203. D. S. Scholl, A. Asthagiri, and T. D. Power, *J. Phys. Chem. B*, **105**, 4771 (2001).

204. D. S. Scholl, *Langmuir*, **14**, 862 (1998).

205. A. Ahmadi, G. Attard, J. Feliu, and A. Rodes, *Langmuir*, **15**, 2420 (1999).

206. R. Widmer, F. –J. Haung, P. Ruffieux, O. Gr□ning, M. Bielmann, P. Gr□ning, R. Fasel, *J. Am. Chem. Soc.*, **128**, 14103 (2006).

207. E. Whaites, and C. Roderick, Essentials of Dental Radiography and Radiology, 19-22 (2002).

208. B. D. Culity, and S. R. Stock, *Elements of X-ray Diffraction*, 3rd ed. 2001, Upper Saddle River, New Jersey: Prentice Hall.

209. V. Srikanth, J. S. Speck, and D. R. Clarke, *J. Appl. Phys.*, **82**, 4286 (1997).

210. V. K. Zworykin and E. G. Ramberg, *Photoelectricity and Its Applications*, J. Wiley & Sons, New York, 1949.

211. J. I. Goldstein, D. E. Newbury, P. Echlin, D. C. Joy, A. D. Roming, C. E. Fiori and E. Lifshin, *Scanning Electron Microscopy and X-Ray Microanalysis*. 2nd ed. New York and London:Plenum Press, 1992.

212. D. B.Williams, and C. B. Carter, *Transmission Electron Microscopy: Basics*. Vol. I., New York: Springer Science-Business media, Inc, 1996.

213. P. Grünberg, R. Schreiber, Y. Pang, M. B. Brodsky, and H. Sowers, *Phys. Rev. Lett.*, **57**, 2442 (1986).

214. M. N. Baibich, J. Broto, A. Fert, F. N. Van Dau, F. Petroff, P. Eitenne, G. Creuzer, A. Friederich, and J. Chazelas, Phys. Rev. Lett. **61**, 2472 (1988).

215. G. H. Jonker, and J. H. Van Santen, Physica, 16, 377 (1950).

216. S. Foner, *Rev. Sci. Instrum.*, **27**, 548 (1956).

217. S. Foner, *J. Appl. Phys.*, **79**, 4740 (1996).

218. P. A. Joy, P. S. Anil Kumar and S. K. Date, *J. Phys.: Condens. Matter*, **10**, 11049 (1998).

219. A. Odagawa, Y. Katoh, Y. Kanzawa, Z. Wei, T. Mikawa, S. Muraoka, and T. Takagi, *Appl. Phys. Lett.* **91**, 133503/1 (2007).

220. R. V. Gudavarthy, S. Gorantla, G. Mu, E. A. Kulp, T. Gemming, J. Eckert, and J. A. Switzer, *Chem. Mater.* Manuscript under preparation.

PAPER

I. Resistance switching in electrodeposited magnetite superlattices

Jay A. Switzer,* Rakesh V. Gudavarthy, Elizabeth A. Kulp, Guojun Mu, Zhen He, Andrew J. Wessel

Department of Chemistry and Graduate Center for Materials Research, Missouri University of Science and Technology, Rolla, MO 65409-1170, USA

Email: jswitzer@mst.edu

As the size of non-volatile memory continues to shrink, there is increasing demand for highly scalable memory devices. An emerging technology is resistive random access memory (RRAM) that is based on resistance switching in materials such as transition metal oxides.[1] Natelson and coworkers have shown that nanophase magnetite, Fe_3O_4, exhibits resistance switching,[2] which they attribute to an electric field driven insulator-to-metal phase transition below the Verwey temperature[3] of 120 K due to strong electron-phonon coupling. For such RRAM devices, it is often necessary to have nanophase material. Superlattices (that is, periodic layered nanostructures with coherent stacking of atomic planes) are ideal for such applications, because they combine the nanometer-scale dimensions of the individual layer thicknesses with the utility of large-scale films that can be conveniently connected to the real world. We previously demonstrated that it is possible to electrodeposit both defect chemistry and compositional ceramic superlattices.[4] Here, we show that defect chemistry superlattices based on Fe_3O_4 and compositional superlattices in the $Fe_3O_4/ZnFe_2O_4$ system can be electrodeposited as epitaxial films on Au(111) from a single plating bath by simply pulsing the applied potential. We designate superlattices based on Fe_3O_4 which have alternating layers with different Fe(III)/Fe(II) ratios as *defect chemistry* superlattices, and superlattices in the $Fe_3O_4/ZnFe_2O_4$ system which have alternating layers with different Fe/Zn ratios as *compositional* superlattices. Due to the nanometer-scale thickness of the layers in the

magnetite defect-chemistry superlattices they exhibit a unique and potentially important multistate resistance switching during perpendicular transport measurements.

In the deposition of superlattices we exploit the fact that magnetite (Fe_3O_4) and zinc ferrite ($ZnFe_2O_4$) deposit by an electrochemical/chemical (EC) mechanism, and that the surface concentrations of Fe(II) and Fe(III) can be precisely controlled through the applied potential. Films of Fe_3O_4 can be deposited with stoichiometries that depend on the applied potential. We deposit defect chemistry superlattices based on Fe_3O_4 from a stirred solution of 87 mM Fe(III), 100 mM triethanolamine (TEA), and 2 M NaOH at 80 °C. The deposition of Fe_3O_4 is believed to occur by an electrochemical-chemical (EC) mechanism described by Eq. 1 and 2.[5]

$$Fe(TEA)^{3+} + e^- \rightarrow Fe^{2+} + TEA \quad (1)$$

$$Fe^{2+} + 2Fe(TEA)^{3+} + 8OH^- \rightarrow Fe_3O_4 + 2TEA + 4H_2O \quad (2)$$

A linear sweep voltammogram at 50 mV/s of an Au(111) single crystal in the stirred (200 rpm) deposition bath is shown in Figure. 1A. The deposition of Fe_3O_4 begins at a potential of -0.99 V, and the reaction becomes mass-transport-limited at a potential of about -1.2 V vs. Ag/AgCl. The mass-transport-limited current is predominately controlled by convection. At low overpotentials where i = 0, the surface concentration of $Fe(TEA)^{3+}$ should be equal to the bulk concentration, whereas at high overpotentials at which the current reaches the mass-transport limit the surface concentration of $Fe(TEA)^{3+}$ should approach zero. The surface concentration of Fe(III) can be calculated from Eq. 3,

$$\frac{i}{i_{l,c}} = \frac{[C_{Fe(III)}(bulk) - C_{Fe(III)}(surface)]}{C_{Fe(III)}(bulk)} \quad (3)$$

where i is the measured current, $i_{l,c}$ is the limiting cathodic current, $C_{Fe(III)}(bulk)$ is the bulk concentration of Fe(III) in solution, and $C_{Fe(III)}(surface)$ is the Fe(III) concentration at the electrode surface.[6] Stoichiometric Fe_3O_4 should deposit at an applied potential of -1.06 V vs. Ag/AgCl at which $i/i_{l,c} = 1/3$. The material should have an excess of Fe(III) at potentials more positive than -1.06 V, and an excess of Fe(II) at potentials more negative than -1.06 V vs. Ag/AgCl.

Compositional superlattices in the $Fe_3O_4/ZnFe_2O_4$ system can be produced by adding 30 mM Zn(II) to the deposition bath. The Zn(II) is electrochemically inert in the potential range of deposition and will substitute for Fe(II) in the crystal structure. The Zn(II) concentration in the film should decrease as the current approaches the mass transport limit, because the surface concentration of Fe(II) increases as the current is increased. The calculated surface concentrations of Fe(III), Fe(II), and Zn(II) are shown in Figure. 1B. The dependence of the lattice parameters of Fe_3O_4 and $Zn_xFe_{3-x}O_4$ films on the applied potential is shown in Figure. 1C. In reasonable agreement with our calculations, Fe_3O_4 deposited at approximately -1.05 to -1.06 V vs. Ag/AgCl has a lattice parameter that agrees well with the literature value of Fe_3O_4. We also measured the Verwey transition of films grown at a series of potentials by transport measurements. The Verwey transition temperature reaches a maximum value of 123 K for a magnetite film deposited at -1.065 V vs. Ag/AgCl, compared with 103 K for a film grown at -1.01 V vs. Ag/AgCl. Because nonstoichiometry is known to lower the Verwey transition temperature, our results suggest that nearly stoichiometric magnetite is produced at a potential of -1.065 V vs. Ag/AgCl. Films grown in the presence of Zn(II) have lattice parameters that approach the literature value of $ZnFe_2O_4$ at more positive potentials. The calculated and measured (by EDS) Zn content of the films as a function of potential are shown in Figure. 1D. The Zn concentration was calculated by assuming that the Zn(II)/Fe(II) ratio in the film is the same as the ratio of the surface concentrations calculated in Fig. 1B from the linear sweep voltammogram. The Zn content in the films decreases as the current approaches the mass transport limit.

Defect chemistry superlattices based on Fe_3O_4 were deposited by pulsing the potential in the Fe(III)-TEA bath between -1.01 and -1.065 V vs. Ag/AgCl. Compositional superlattices in the $Fe_3O_4/ZnFe_2O_4$ system were deposited from the same bath with 30 mM Zn(II) added by pulsing between -0.99 and -1.05 V vs. Ag/AgCl. The superlattices were deposited as epitaxial films on single-crystal Au(111) substrates.

The layered structure of a compositional superlattice in the $Fe_3O_4/ZnFe_2O_4$ system is readily apparent in the high angle annular dark field (HAADF) image in Figure. 2A that we obtained in a focused ion beam (FIB) microscope. The superlattice was designed to have a large modulation wavelength of 70 nm so that it could be easily imaged in the

FIB. The light layers that are 25 nm thick correspond to the higher zinc content layer that was grown at -0.99 V vs. Ag/AgCl. The darker layers that are 45 nm thick correspond to the lower zinc content material that was grown at -1.05 V vs. Ag/AgCl.

The superlattices were also characterized by X-ray diffraction. Figure. 2B shows the (311) X-ray pole figures of a compositional superlattice in the $Fe_3O_4/ZnFe_2O_4$ system with a modulation wavelength of 12.5 nm (left) and the Au(111) substrate (right). The superlattice was deposited from the Zn(II)-containing bath by pulsing between -0.99 V vs. Ag/AgCl for 2.5 s and -1.05 V vs. Ag/AgCl for 0.5 s. The X-ray pole figures show that the superlattice grows epitaxially on the Au(111). Both pole figures have sharp peaks at tilt angles of 29.5, 58.5, and 80°, but the peaks for the superlattice are rotated azimuthally by 180° relative to the Au(111) peaks. That is, the films grow with the same (111) out-of-plane orientation as the substrate, but they are rotated antiparallel in-plane. The epitaxial relationship of the films to the Au(111) substrate is $Fe_3O_4(111)[01\bar{1}]//Au(111)[0\bar{1}1]$.

X-ray diffraction provides direct evidence that these multilayered films are superlattices (that is, crystallographically coherent multilayers). Figures. 2C and 2D show X-ray diffraction patterns of Fe_3O_4 superlattices (Fig. 2C) with modulation wavelengths of 12.2, 20.6, and 25.8 nm, and compositional superlattices in the $Fe_3O_4/ZnFe_2O_4$ system (Fig. 2D) with modulation wavelengths of 12.5, 16.8, and 29.2 nm. The superperiodicity of the superlattices manifests itself as satellites around the (444) Bragg peak. The modulation wavelength, Λ, of the superlattices was calculated from the position of the satellites using Eq. 4, where λ is the wavelength of the x-ray source (Cu Kα = 0.15401 nm), L is the order of the satellite and θ is the diffraction angle of satellite L.[4b] The satellites are more intense in the Zn-containing superlattices, due to the larger Z-contrast in those superlattices.

$$\Lambda = \frac{\lambda(L_1 - L_2)}{2(\sin\theta_1 - \sin\theta_2)} \tag{4}$$

The electrodeposited defect-chemistry superlattices based on magnetite exhibit resistance switching during perpendicular transport measurements at 77 K. Resistance switching in bulk magnetite has been known since 1969.[7] Basically, a sample is

maintained at a temperature (for example, 77 K) below the Verwey transition (120 K), at which the material is insulating. During a sweep of either the applied current or voltage, the magnetite undergoes an insulator-to-metal phase transition and the resistance sharply decreases. The high-to-low resistance switching in single-crystal magnetite has been attributed to an insulator-to-metal transition driven either by Joule heating due to the current flowing through the sample,[7] or to an electric-field-driven transition due to the strong electron-phonon coupling.[2] Lee et al. presented strong evidence that the insulator-to-metal transition in nanophase magnetite is driven by the applied electric field.[2a]

For our resistance switching studies, a contact is made to the top of the superlattice and to the Au(111) single crystal using pressed In contacts (see inset of Figure. 3). This configuration ensures perpendicular transport of charge through the sample. The sample is held below the Verwey transition by immersing it in liquid nitrogen at 77 K, and the bias is measured as the applied current is swept from 0 to 2 A at 50 mA/s. Figure. 3 shows iV curves for two magnetite films grown at -1.01 and -1.065 V vs. Ag/AgCl and a superlattice produced by pulsing between -1.01 V for 1.5 s and -1.065 V vs. Ag/AgCl for 0.5 s. The modulation wavelength of the superlattice is 12.2 nm (measured by X-ray diffraction), and it consists of 354 bilayers. The iV curve of the Fe(III)-rich film deposited at -1.01 V is non-ohmic, but it shows no evidence of resistance switching. The iV curve of the Fe_3O_4 film deposited at -1.065 V has a similar non-ohmic shape, except that it shows abrupt low-to-high resistance switching at applied biases of +0.95 and -0.93 V. This low-to-high resistance switching is not due to the insulating-to-metal phase transition that occurs at the Verwey transition. A similar transition has been observed in nanophase magnetite at room temperature.[8] Odagawa et al. attributed this low-to-high resistance switch to a field-driven oxidation of Fe_3O_4 to the less conductive γ-Fe_2O_3 (maghemite) at the interface between the metallic anode electrode and the Fe_3O_4.[8a] They detected maghemite at the interface using Raman spectroscopy. We assume that the low-to-high resistance switch that we observe in the Fe_3O_4 deposited at -1.065 V vs. Ag/AgCl is also due to the oxidation of Fe_3O_4 to the more resistive γ-Fe_2O_3.

The iV curve for the superlattice in Figure. 3B is richer in features than that of the individual films due to the nano-layering of the superlattice. It shows two low-to-high resistance switches at applied biases of +1.7/-1.5 V and +2.4/-2.3 V. We assume that

these first two transitions are associated with the electrochemical oxidation of Fe_3O_4 to the more resistive γ-Fe_2O_3 at the contact/film interface as proposed by Odagawa et al.[8a] Following the second of these low-to-high resistance switches, the curve shows oscillations of the bias voltage, followed by a negative differential resistance (NDR) feature at +2.7/-2.6 V. The resistance of the superlattice abruptly decreases after the NDR feature, as shown by the near-vertical increase in current to the 2A limit of our instrument following the NDR feature. This final high-to-low resistance switch is consistent with the insulator-to-metal phase transition of the Verwey transition.

Because both the applied electric fields ($\sim 10^6$ V/m) and the resulting currents (~1 A) are large in the resistance switching experiments, it is difficult to determine whether the insulator-to-metal transition in the superlattices is caused by Joule heating of the sample (from 77 K to greater than the Verwey transition temperature) or to an electric-field-driven transition that is due to strong electron-phonon coupling. Our measurements do show, however, that the transition is not due entirely to Joule heating, because the magnetite films deposited at -1.01 and -1.065 V vs. Ag/AgCl do not undergo the insulator-to-metal transition, even though the power dissipated by the samples is as large as that of the superlattice. For the magnetite film deposited at -1.01 V vs. Ag/AgCl, the Verwey transition temperature is 103 K, compared with 121 K for the superlattice, so it should take less power dissipation to raise the sample above the Verwey transition, yet the insulator-to-metal transition is not observed.

The insulator-to-metal phase transition in the superlattice may be facilitated by residual strain in the superlattice. Because of the lattice mismatch between the two layers in the superlattice, the alternating layers have 0.37% compressive and 0.37% tensile strain. These alternating strain fields will lower the symmetry of the system so that the structure of the magnetite more closely resembles the monoclinic low-temperature phase below the Verwey transition than the high-temperature cubic phase, resulting in a more kinetically labile phase transition. The alternating strain fields may also affect electron-phonon interaction. Below the Verwey transition, magnetite is in a charge ordered state with strong coupling of phonons to conduction electrons.[9] As suggested by other researchers,[2,10] the applied electric field may break down the charge-ordered state in the material. In our experiments this transition occurs with the nanolayered superlattice, but

not with the individual films. The fact that multiple resistance states can be accessed by simply varying the applied bias opens up new possibilities for multi-bit data storage and retrieval.

Acknowledgment. This work was funded by supported by the U. S. Department of Energy, Office of Basic Energy Sciences under Grant No. DE-FG02-08ER46518.

Supporting Information Available: Methods and materials, linear sweep voltammograms, Verwey transition temperatures, and additional resistance switching results. This material is available free of charge via the Internet at http://pubs.acs.org.

REFERENCES

1. (a) Waser, R.; Aono, M. *Nat. Mater.* **2007**, *6*, 833-840. (b) Sawa, A. *Mater. Today* **2008**, *11*, 28-36. (c) Szot, K.; Speier, W.; Bihlmayer, G.; Waser, R. *Nat. Mater.* **2006**, *5*, 312-320. (d) Yang, Y. C.; Pan, F.; Liu, Q.; Liu, M.; Zeng, F. *Nano Lett.* **2009**, *9*, 1636-1643.
2. (a) Lee, S.; Fursina, A.; Mayo, J. T.; Yavuz, C. T.; Colvin, V. L.; Sofin, R. G. S.; Shvets, I. V.; Natelson, D. *Nat. Mater.* **2008**, *7*, 130-133. (b) Fursina, A. A.; Sofin, R. G. S.; Shvets, I. V.; Natelson, D. *Phys. Rev. B.* **2009**, *79*, 245131/1-245131/6.
3. Verwey, E. J. W. *Nature* **1939**, *144*, 327-328.
4. (a) Switzer, J. A.; Hung, C.-J.; Breyfogle, B. E.; Shumsky, M. G.; Van Leeuwen, R.; Golden, T. D. *Science* **1994**, *264*, 1573-1576. (b) Switzer, J. A.; Shane, M. J.; Phillips, R. J. *Science* **1990**, *247*, 444-446. (c) Kothari, H. M.; Vertegel, A. A.; Bohannan, E. W.; Switzer, J. A. *Chem. Mater.* **2002**, *14*, 2750-2756.
5. (a) Kulp, E. A.; Kothari, H. M.; Limmer, S. J.; Yang, J.; Gudavarthy, R. V.; Bohannan, E. W.; Switzer, J. A. *Chem. Mater.* **2009**, *21*, 5022-5031. (b) Kothari, H. M.; Kulp, E. A.; Limmer, S. J.; Poizot, P.; Bohannan, E. W.; Switzer, J. A. *J. Mater. Res.* **2006**, *21*, 293-301.
6. Bard, A. J.; Faulkner, L. R. *Electrochemical Methods: Fundamentals and Applications* Wiley: New York, 2001; p. 340.
7. (a) Burch, T. J.; Craig, P. P.; Hedrick, C.; Kitchens, T. A.; Budnick, J. I.; Cannon, J. A.; Lipsicas, M.; Mattis, D. *Phys. Rev. Lett.* **1969**, *23*, 1444-1447. (b) Freud, P. J.; Hed, A. Z. *Phys. Rev. Lett.* **1969**, *23*, 1440-1443.
8. (a) Odagawa, A.; Katoh, Y.; Kanzawa, Y.; Wei, Z.; Mikawa, T.; Muraoka, S.; Takagi, T. *Appl. Phys. Lett.* **2007**, *91*, 133503/1-133503/3. (b) Kim, T. H.; Jang, E. Y.; Lee, N. J.; Choi, D. J.; Lee, K.-J.; Jang, J.-T.; Choi, J.-S.; Moon, S. H.; Cheon, J. *Nano Lett.* **2009**, *9*, 2229-2233.
9. (a) Piekarz, P.; Parlinski, K.; Oles, A. M. *Phys. Rev. Lett.* **2006**, *97*, 156402/1-156402/4. (b) Huang, D. J.; Lin, H.-J.; Okamoto, J.; Chao, K. S.; Jeng, H.-T.; Guo, G. Y.; Hsu, C.-H.; Huang, C.-M.; Ling, D. C.; Wu, W. B.; Yang, C. S.; Chen, C. T. *Phys. Rev. Lett.* **2006**, *96*, 096401/1-096401/4.

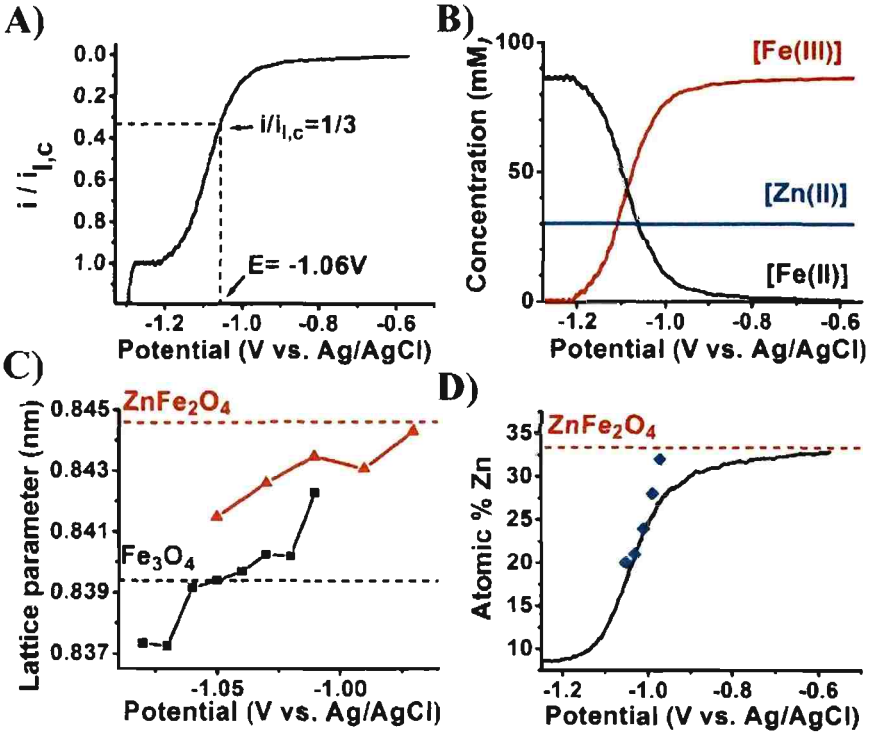

Figure. 1. Using the applied potential to control the composition of magnetite and zinc ferrite films. **A)** Linear sweep voltammogram in the Fe(III)-TEA bath used to produce magnetite defect chemistry superlattices. **B)** Plot of the concentrations of Fe(III), Fe(II), and Zn(II) at the electrode surface as a function of potential for the alkaline Fe(III)-TEA bath with 30 mM Zn(II) added, which is used to produce compositional superlattices in the $Fe_3O_4/ZnFe_2O_4$ system. **C)** Plot of the lattice parameters of magnetite (black squares) and films in the magnetite/zinc ferrite system (red triangles) as a function of applied potential. The literature values for the lattice parameters of stoichiometric Fe_3O_4 and $ZnFe_2O_4$ are shown as black and red horizontal dashed lines. **D)** Comparison of the measured Zn concentration (blue diamonds) to the calculated Zn concentration (smooth black curve) for films in the $Fe_3O_4/ZnFe_2O_4$ system as a function of applied potential. The composition of stoichiometric $ZnFe_2O_4$ is shown as a horizontal dashed red line.

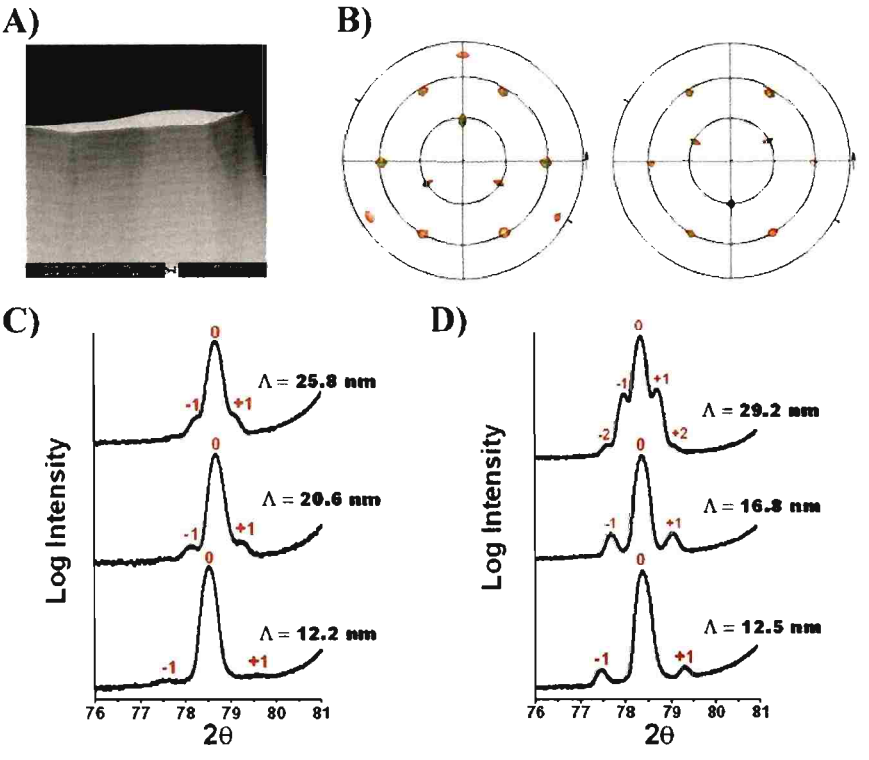

Figure. 2. Electron microscopy and X-ray diffraction of electrodeposited superlattices. **A)** STEM-high angle annular dark field image of zinc ferrite superlattice with a modulation wavelength of 70 nm. **B)** (311) pole figures of zinc ferrite superlattice with 12.5 nm modulation wavelength (left) and Au(111) substrate (right). **C)** 2θ scan around the (444) reflection for magnetite superlattices. **D)** 2θ scan around the (444) reflection for zinc ferrite superlattices.

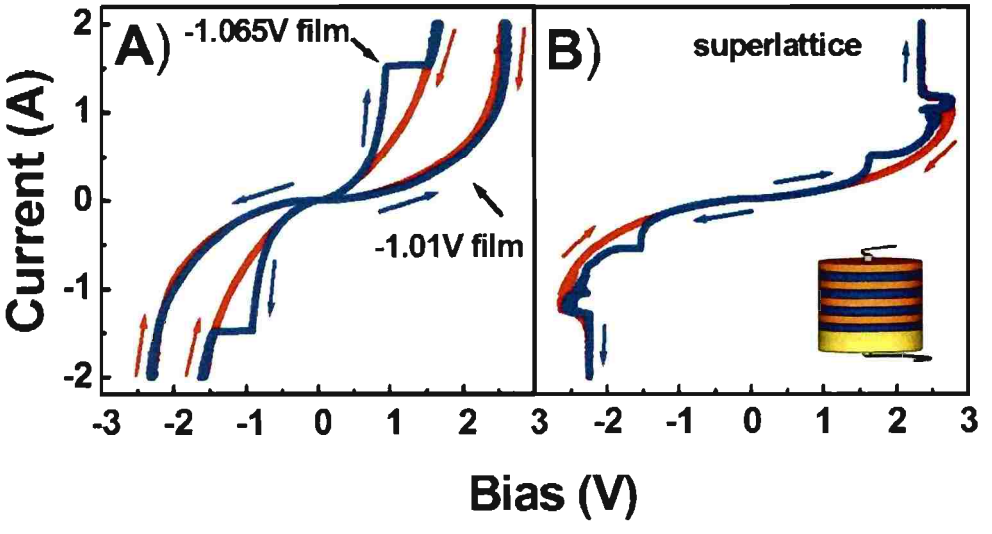

Figure. 3. Resistance switching of magnetite films (A) and a magnetite superlattice (B) on Au(111) at 77 K. The iV curves were run with the current flowing perpendicular to the films by scanning the applied current at 50 mA/sec. In each curve the forward scan is blue, and the reverse scan is red. The magnetite films in (A) were grown at -1.01 V and -1.065 V to a thickness of 5 μm. The magnetite superlattice in (B) was produced by pulsing between -1.01 V for 1.5 sec and -1.065 V for 0.5 sec with a modulation wavelength of 12.2 nm, 354 bilayers, and a total thickness of 4.3 μm. Only the superlattice shows the negative differential resistance (NDR) feature due to the field-assisted insulator-to-metal phase transition.

II. Resistance Switching in Electrodeposited Polycrystalline Fe_3O_4 Films**

Rakesh V. Gudavarthy, Andrew S. Miller, Eric W. Bohannan, Elizabeth A. Kulp, Zhen He and Jay A. Switzer*

[*] Prof. Jay A. Switzer, R. V. Gudavarthy, A. S. Miller, Dr. E. W. Bohannan, Dr. E. A. Kulp, Z. He

Department of Chemistry and Graduate Center for Materials Research

103 Straumanis-James Hall (Materials Research Center)

Missouri University of Science and Technology

Rolla, MO 65409-1170, USA.

[**] This work was supported by the U.S. Department of Energy, Office of Basic Energy Sciences under Grant No. DE-FG02-08ER46518. The authors would like to thank Prof. Matt O'Keefe and Mr. Travis K. McKindra for helping with Au sputtering. Supporting Information is available from Wiley InterScience or from the author.

Keywords: Data Storage, Thin Films, Nanocrystals, Magnetic Materials

As conventional memory devices reach the size limit, the search for small nonvolatile memory devices intensifies. Some of the nonvolatile memory devices which have been considered recently include magnetic random access memory,[1,2] flash memory,[3] phase change memory,[4] and resistance random access memory (RRAM).[5,6] Among these new memory devices, RRAM devices are considered to have several advantages, such as fast writing times, high densities, and low operating voltages.[7] Magnetite, Fe_3O_4, is a good candidate for such RRAM devices. Fe_3O_4 undergoes a metal-insulator transition at the Verwey temperature (T_V ~120 K).[8] Above T_V, Fe_3O_4 has a cubic structure and is moderately conducting, transforming to a distorted cubic structure below T_V, which is insulating.[9] Natelson and co-workers have shown that nanophase Fe_3O_4 exhibit resistance switching, when a large electric field is applied for a film which is in the insulating state below T_V, due to strong electron-phonon coupling.[10] Recently, we have shown that superlattices in the Fe_3O_4 system exhibit multistate resistance

switching during perpendicular transport measurements at 77 K.[11] Here, we show that simple polycrystalline films of Fe_3O_4 electrodeposited on stainless steel (SS) substrates also exhibit multistate resistance switching due to the presence of a thin nano-crystalline layer. We also show that in such films resistance switching can be tuned by controlling the composition of the films by varying the potential for deposition.

In this paper, we study the resistance switching behavior of polycrystalline Fe_3O_4 films electrodeposited on stainless steel (SS) substrates at 77 K. It is seen that the films grown at potentials more positive than -1.05 V (vs. Ag/AgCl) have low-to-high and high-to-low resistance jumps. Films grown at potentials more negative than -1.05 V have only high-to-low resistance jumps. The study indicates that the primary cause for the low-to-high resistance jump is the non-stoichiometry of the Fe_3O_4 films. This is further supported by the fact that the jump disappears for stoichiometric Fe_3O_4 films. However, the high-to-low jump due to the insulator to metal transition is facilitated by the presence of a thin nano-crystalline layer near the SS substrate. We believe that Joule heating is the primary mechanism through which the high-to-low resistance jump occurs in the polycrystalline films.

A linear sweep voltammogram at 50 mV/s of a SS substrate indicated that the deposition of Fe_3O_4 begins at a potential of -0.99 V, and reaches the mass transport limit at a potential of -1.2 V vs Ag/AgCl. In the deposition of Fe_3O_4, we exploit the fact that the reaction proceeds via an electrochemical/chemical (EC) mechanism and the surface concentrations of Fe(II) and Fe(III) can be precisely controlled through the applied potential, described by eqs 1 and 2.[11, 12]

$$Fe(TEA)^{3+} + e^- \rightarrow Fe^{2+} + TEA \quad (1)$$

$$Fe^{2+} + 2Fe(TEA)^{3+} + 8OH^- \rightarrow Fe_3O_4 + 2TEA + 4H_2O \quad (2)$$

At low overpotentials where i = 0, the surface concentration of $Fe(TEA)^{3+}$ should be equal to the bulk concentration, whereas, at high overpotentials at which the current reaches the mass-transport limit the surface concentration of Fe(III) should approach zero. The surface concentration of Fe(III) at different potentials can be calculated from eq 3,

$$\frac{i}{i_{l,c}} = \frac{[C_{Fe(III)}(bulk) - C_{Fe(III)}(surface)]}{C_{Fe(III)}(bulk)} \quad (3)$$

where i is the measured current, $i_{l,c}$ is the limiting cathodic current, $C_{Fe(III)}$ (bulk) is the bulk concentration of Fe(III) in solution, and $C_{Fe(III)}$(surface) is the Fe(III) concentration at the electrode surface.[11] Stoichiometric Fe_3O_4 can be deposited at the potential where $i/i_{l,c} = 1/3$. At any other potential non-stoichiometric Fe_3O_4 is deposited. [11] In our experiments, stoichiometric Fe_3O_4 films can be electrodeposited at a potential of -1.05 V vs Ag/AgCl on a SS substrate. Material deposited at potentials more positive than -1.05 V should have excess Fe(III), and material deposited at potentials more negative than -1.05 V should have excess Fe(II). XRD also suggests that stoichiometric Fe_3O_4 can be deposited at -1.05 V (see Figure S1).

Resistance switching studies were performed on the electrodeposited polycrystalline Fe_3O_4 films on SS substrates. Contacts were made to the top of the film and the SS substrate using pressed In metal and silver wire. The sample was held below the Verwey transition by immersing it in liquid nitrogen at 77 K, and the bias was measured as the applied current was swept from 0 to 2 A at 50 mA/s. Figure 1 shows the iV curves for the Fe_3O_4 films electrodeposited at 10 mV increments starting at -1.01 V vs Ag/AgCl. The iV curves for the films deposited between -1.01 V to -1.04 V (Figure 1A through 1D) show a non-ohmic behavior and have a low-to-high resistance switch followed by a sharp high-to-low resistance switch irrespective of the sign of the applied bias. Whereas, the films deposited between -1.05 V to -1.09 V (Figure 1E through 1I) also have a non-ohmic behavior but have either a very small or no low-to-high resistance jump. Especially, the stoichiometric Fe_3O_4 film deposited at -1.05 V vs Ag/AgCl has no low-to-high resistance jump. The films grown at potentials more negative than -1.05 V have a very small low-to-high resistance switch. Following the low-to-high resistance switch, all the curves show oscillation of the bias voltage. The iV curves for the films deposited at all of the potentials show a high-to-low resistance switch. This high-to-low resistance switch is consistent with the insulator-to-metal Verwey transition.

The mechanism of resistance switching in Fe_3O_4 films has been attributed to Joule heating, electric-field-driven or in some cases both. [10, 11, 13, 14] We assume that the low-

to-high resistance switch in our samples is associated with electrochemical oxidation of Fe_3O_4 to the more resistive γ-Fe_2O_3 as proposed by Odagawa et al. [15] The low-to-high resistance switch only occurs in non-stochiometric Fe_3O_4 films as shown in Figure 1. The scan rate dependence study shows that the low-to-high resistance switch is highly scan rate dependent indicating that it is a slow process. On the other hand, the high-to-low resistance switch is a very fast process and is scan rate independent (see Figure S2).

It is difficult to determine whether the high-to-low resistance switch (insulator-to-metal transition) occurs due to Joule heating or if it is electric-field-driven because both the applied electric field (~10^6 V/m) and the resulting currents (~ 1 A) are large. To determine whether the effect is due to the applied electric field or to Joule heating, we varied the contact sizes and measured the bias as the applied current was scanned from 0 to 2 A. Figure 2A shows the iV curves with different contact sizes for a Fe_3O_4 film deposited at -1.01 V vs. Ag/AgCl on SS substrate. The curves show that as the contact size increases, the insulator-to-metal transition occurs at lower bias. The graph was re-plotted with power density as a function of bias as shown in Figure 2B. The figure shows that although the bias at which the insulator-to-metal transition occurs is a function of the contact area, this transition occurs at a fixed power density of 248 W/nm^3 for each film. The fact that the insulator-to-metal transition occurs at fixed power density suggests that Joule heating is the cause for the transition. The iV curves in Figure 2A also show that the hysteresis increases as we increase the contact size. This can also be attributed to Joule heating as shown by other researchers.[16] Two types of contacts (In and Au) were tried for resistance switch experiments on the -1.01 V Fe_3O_4 films, which includes In and Au, and we found that there was no significant effect on the general shape of the iV curves (see Figure S3). Depending on the contact size, the bias at which the jump occurred was different. This shows that the barrier between the film and the contact does not play a major role in the resistance switching.

Resistance switching was earlier observed in Fe_3O_4 single crystals,[13, 14] nano-particles,[10] epitaxial thin films,[10] and defect chemistry superlattices.[11] It was shown that nanometer size Fe_3O_4 particles are critical for the switching to happen at lower bias. Single crystal Fe_3O_4 shows resistance switching, only if a large bias (~10 V) is applied.[13] We did not observe resistance switching on commercial Fe_3O_4 (111) single

crystal within our instrument limitation (± 2 A, ± 10 V, see figure S4). When the resistance switching experiment was performed on a 2 μm thick epitaxial film, electrodeposited at -1.03 V on Au(111), we observed only a low-to-high resistance jump, due to non-stoichiometric Fe_3O_4. Whereas, the epitaxial film deposited at -1.08 V on Au(111) had no jump.

To understand why resistance switching is seen on polycrystalline films, we studied the morphology of the films deposited on a polycrystalline SS substrate. Figure 3A shows the top plan view of the film deposited at -1.05 V on SS. The figure shows that the films are highly crystalline, and the size of each crystallite is approximately 500 nm. To obtain the cross-sectional view and also to see the bottom of the film, the films were peeled off onto a microscope slide using superglue. Figure 3B shows the cross-sectional view of the columns of Fe_3O_4. The columns start growing from very small crystals (Volmer-Weber growth) before coalescence occurs and results in bigger crystallites. The average width of the columns is approximately 300 nm. To determine the size of the initial crystallites, SEM microscopy was performed on the bottom of the film as shown in Figure 3C. The SEM image of the bottom of the film looks smooth, indicating that there might be a very thin nano-crystalline layer to start with, which then transforms to bigger crystallites. The AFM technique was used to determine the size of the initial crystallites. Figure 3D shows an AFM image of the Fe_3O_4 surface peeled off onto the glass substrate. The average particle size determined by fitting to a normal distribution was around 41± 20 nm. The thickness of this nano-crystalline layer is approximately 50 nm determined from the cross sectional SEM image. The presence of nano-crystallites in this layer is critical for insulator-to-metal phase transition to occur at lower bias in polycrystalline films. It is well known fact that the particle size affects the magnetic and transport properties of the materials. [17] Poddar et al. observed a shift in the Verwey transition from 120 K in the bulk magnetite single crystal to 90 K in magnetite nano-particles with a size range of 6-8 nm. [18, 19] In our case, we believe that the presence of nano-crystallites shifts the Verwey temperature to a lower value which allows for resistance switching to happen at lower bias. The switching starts in the nano crystalline layer where the phase transition initiates, eventually, transforming the entire bulk material. In the case of epitaxial bulk

films and single crystals the phase transition jump is not possible because the T_v is close to the bulk value (~120 K).

Resistance switching has been observed in various other transition metal oxides. [20, 21] Metal oxide such as Fe_3O_4, [22, 23] Cu_2O, [24] CuO, [25] Bi_2O_3, [26] and ZnO [27] which can be electrodeposited onto different substrates can be good candidates for such RRAM devices. These metal oxides utilize the filamentary mechanism for resistance switching.[28] However, the fact that the resistance switching can be obtained on a Fe_3O_4 film electrodeposited on a simple polycrystalline substrate which can be tuned by controlling the composition, opens up new possibilities for memory storage devices. Integration of Fe_3O_4 into current devices might be a major challenge, as it works at temperatures below 120 K.

In conclusion, we have demonstrated that resistance switching can be tuned by controlling the composition of the Fe_3O_4 films. Non-stoichiometric Fe_3O_4 films show low-to-high resistance jumps as well as high-to-low resistance jumps. However, the stoichiometric Fe_3O_4 film only shows a high-to-low resistance jump. The low-to-high jump is a slow process and is highly scan rate dependent. On the other hand, the high-to-low jump associated with the Verwey transition is a fast process and is scan rate independent. In our experiments, we also observed that by increasing the contact size the insulator-to-metal transition occurs at lower bias but fixed power density indicating that Joule heating plays a significant role in the resistance switching. Our experiments also suggest that the insulator-to-metal transition may be facilitated by the presence of a thin nano-crystalline layer which is critical for resistance switching to occur at lower bias.

Experimental

The deposition bath for magnetite films contained 87 mM Fe(III), 100 mM TEA, and 2 M NaOH. The solution was prepared by dissolving 2.6 grams of iron (II) sulfate pentahydrate in 15 ml of 1 M triethanolamine (TEA), resulting in a deep red-colored solution. It was diluted with 50 ml of deionized water. The diluted solution was then added to a second solution that was produced by adding 12.0 g of NaOH pellets to 85 ml of deionized water. The resulting 150 ml of grey-green solution was heated to 80 °C and stirred at a rate of 200 rpm.

The electrodeposition of films and linear sweep voltammograms (Fig. S1 A) was performed using a Brinkmann PGSTAT 30 Autolab potentiostat controlled with GPES software version 4.9. Polycrystalline films were deposited on stainless steel (SS) 304 L pucks with a geometric area of 1.76 cm^2, wrapped with a SS wire around the perimeter of the crystal for electrical contact. A Pt wire served as the counter electrode, and an Ag/AgCl (KCl saturated) electrode was the reference electrode. The SS pucks were mechanically polished before each deposition. The films were deposited onto SS pucks by applying constant potentials of -1.01, -1.02, -1.03, -1.04, -1.05, -1.06, -1.07, -1.08, and -1.09 V vs. Ag/AgCl. The total charge passed through the electrode was controlled to be 1 C/cm^2 to obtain a film that was approximately 2 μm thick.

The morphology of the electrodeposited films was probed by scanning electron microscopy (SEM) and atomic force microscopy (AFM). The images were obtained on a Hitachi S4700 SEM. Tapping mode AFM images were obtained for a film peeled of onto a microscope slide using a Digital Instruments Nanoscope IIIa scanning probe microscope.

X-ray analysis was performed using a high-resolution Philips X-pert MRD x-ray diffractometer with a Cu $K_{\alpha 1}$ radiation source (λ = 0.154056 nm). The symmetric x-ray diffraction patterns were obtained using the line focus mode (Figure S1 C). The primary optics consisted of a combination Göbel mirror and a two crystal Ge(220) two-bounce hybrid monochromator (PW3147/00) producing pure Cu $K_{\alpha 1}$ radiation on the incident beam side. A 0.18° parallel plate collimator (PW3098/18) was used as the secondary optics. The lattice parameter of each film was determined by Rietveld analysis using RIQAS software from Materials Data Inc. (Figure S1 B). X-ray pole figures were obtained in a point focus mode (Figure S1 D). A crossed slit collimator module (PW3084/62) served as the primary optics. A 0.27° parallel plate collimator (PW3098/27) equipped with a flat graphite monochromator (PW3121/00) was used as the secondary optics.

Current-voltage curves of Fe_3O_4 on SS pucks, Au(111) crystal and commercial single crystal were measured at 77 K (in liquid N_2) using an EG&G Princeton Applied Research PARSTAT 2273 potentiostat/galvanostat controlled with powersuite software version 2.58. One silver wire was attached to the film surface with indium metal, the

other connected to the SS substrate. For iV curves, the working electrode and sensor leads from the potentiostat were connected to the film surface. The reference and counter electrode leads from the potentiostat were connected to the SS substrate. Both current and voltage scans were performed. The current was scanned at 50 mA/s. Both types of scans were plotted as current vs. bias. The instrument limits for the PARSTAT 2273 potentiostat/galvanostat are ±2 A and ±10 V. The area of the contact was measured using the HiRoX KH-3000 Digital Imaging System.

REFERENCES

[1] J. Åkerman, *Science* **2005**, *308*, 508.

[2] S. Parkin, X. Jiang, C. Kaiser, A. Panchula, K. Roche, M. Samant, *Proc. IEEE* **2003**, *91*, 661.

[3] R. Bez, E. Camerlenghi, A. Modelli, A. Visconti, *Proc. IEEE* **2003**, *91*, 489.

[4] H.F. Hamann, M. O'Boyle, Y.C. Martin, M. Rooks, K. Wickramasinghe, *Nat. Mater.* **2006**, *5*, 283.

[5] W.W. Zhuang ,W Pan, B. D. Ulich, J. J. Lee, L. Stecker, A. Bumaster, D. R. Evans, S. T. Hsu, M. Tajin, A. Shimaoka, K. Inoue, T. Naka, N. Awaya, K. Sakiyama, Y. Wang, S. Q. Liu, N. J. Wu, A. Ignatiev, *Tech. Dig. IEDM* **2002**, 193.

[6] I. G. Baek, M. S. Lee, S. Seo, M. J. Lee, D. H. Seo, D.-S. Suh, J. C. Park, S. O. Park, H. S. Kim, I. K. Yoo, U-In Chung, J. T. Moon, *Tech. Dig. IEDM* **2004**, 587.

[7] K. Tsubouchi, I. Ohkubo, H. Kumigashira, M. Oshima, Y. Matsumoto, K. Itaka, T. Ohnishi, M. Lippmaa, H. Koinuma, *Adv. Mater.* **2007**, *19*, 1711.

[8] E. J. W. Verwey, *Nature* **1939**, *144*, 327.

[9] G. Kh. Rozenberg, M. P. Pasternak, W. M. Xu, Y. Amiel, M. Hanfland, M. Amboage, R. D. Taylor, R. Jeanloz, *Phys. Rev. Lett.* **2006**, *96*, 045705.

[10] S. Lee, A. Fursina, J. T. Mayo, C. T. Yavuz, V. L. Colvin, R. G. S. Sofin, I. V. Shvets, D. Natelson, *Nat. Mater.* **2008**, *7*, 130.

[11] J. A. Switzer, R. V. Gudavarthy, E. A. Kulp, G. Mu, Z. He, A. Wessel, *J. Am. Chem. Soc.* **2010**, *132*, 1258.

[12] E. A. Kulp, H. M. Kothari, S. J. Limmer, J. Yang, R. V. Gudavarthy, E. W. Bohannan, J. A. Switzer, *Chem. Mater.* **2009**, *21*, 5502.

[13] T. J. Burch, P. P. Craig, C. Hendrick, T. A. Kitchens, J. I. Budnick, J. A. Cannon, M. Lipsicas, D. Mattis, *Phys. Rev. Lett.* **1969**, *23*, 1444.

[14] P. J. Freud, A. Z. Hed, *Phys. Rev. Lett.* **1969**, *23*, 1440.

[15] A. Odagawa, Y. Katoh, Y. Kanzawa, Z. Wei, T. Mikawa, S. Muraoka, T. Takagi, *Appl. Phys. Lett.* **2007**, *91*, 133503.

[16] A. A. Fursina, R. G. S. Sofin, I. V. Shvets, D. Natelson, *Phys. Rev. B.* **2009**, *79*, 245131/1.

[17] X. Battle, A. Labarta, *J. Phys. D: Appl. Phys.* **2002**, *35*, R15.

[18] P. Poddar , T. Fried, G. Markovich, *Phys. Rev. B* **2002**, *65*, 172405.

[19] P. Poddar, T. Fried, G. Markvoich, A. Sharoni, D. Katz, T. Wizanksy, O. Millo, *Europhys. Lett,* **2003**, *64*, 98.

[20] A. Sawa, *Mater. Today* **2008**, *11*, 28.

[21] R. Wasner, M. Aono *Nat. Mater.* **2007**, *6*, 833.

[22] M. P. Nikiforov, A. A. Vertegel, M. G. Shumsky, J. A. Switzer, *Adv. Mater.* **2000**, *12*, 1351.

[23] T. A. Sorenson, S. A. Morton, D. G. Waddill, J. A. Switzer, *J. Amer. Chem. Soc.* **2002**, *124*, 7604.

[24] R. Liu, E. W. Bohannan, J.A. Switzer, F. Oba, F. Ernst, *Appl. Phys. Lett.* **2003**, *83*, 1944.

[25] J. A. Switzer, H. M. Kothari, P. Poizot, S. Nakanishi, E. W. Bohannan, *Nature* **2003**, *425*, 490.

[26] J. A. Switzer, M. G. Shumsky, E. W. Bohannan, *Science* **1999**, *284*, 293.

[27] G. Mu, R. V. Gudavarthy, E. A. Kulp, J. A. Switzer, *Chem. Mater.* **2009**, *21*, 3960.

[28] B. J. Choi, D. S. Jeong, S. K. Kim, C. Rohde, S. Choi, J. H. Oh, H. J. Kim, C. S. Hwang, K. Szot, R. Wasner, B. Reichenberg, S. Teidke, *J. Appl. Phys.* **2005**, *98*, 033715.

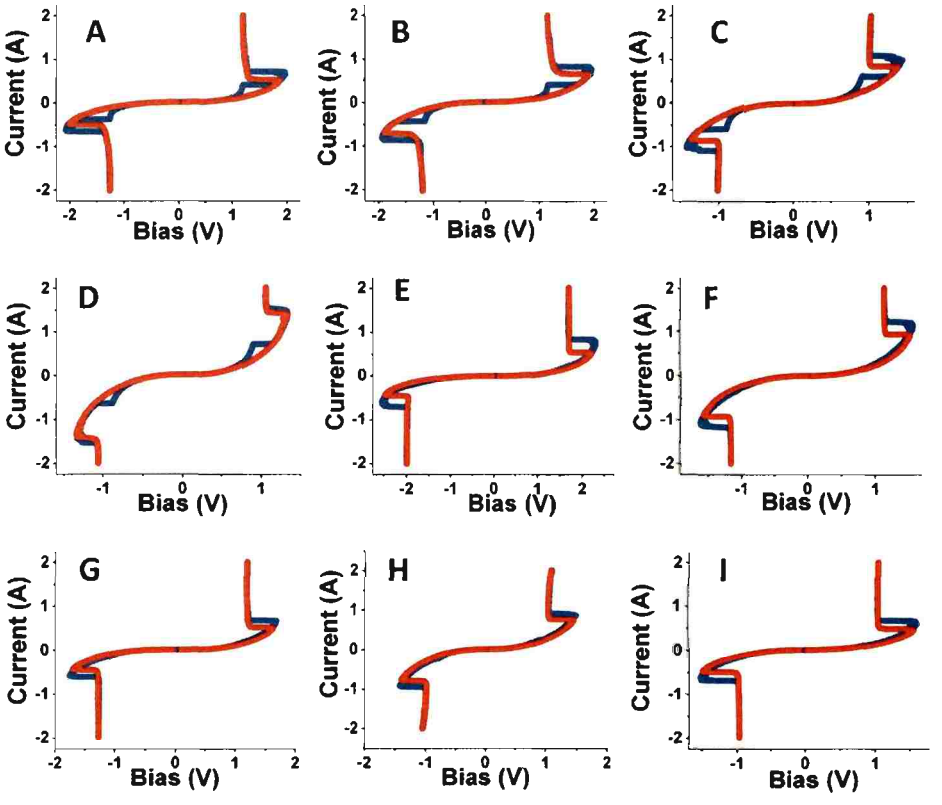

Figure 1. Resistance switching at 77 K of polycrystalline Fe_3O_4 films deposited on SS substrates that were grown at different potentials. (A) -1.01 V (B) -1.02 V (C) -1.03 V (D) -1.04 V (E) -1.05 V (F) -1.06 V (G) -1.07 V (H) -1.08 V (I) -1.09 V vs Ag/AgCl. The iV curves were run with the current flowing perpendicular to the films by scanning the applied current at 50 mA/s. In each curve, the forward scan is blue and the reverse scan is red. The Fe_3O_4 films were grown to a thickness of approximately 2 μm by passing 1 C/cm^2 of charge.

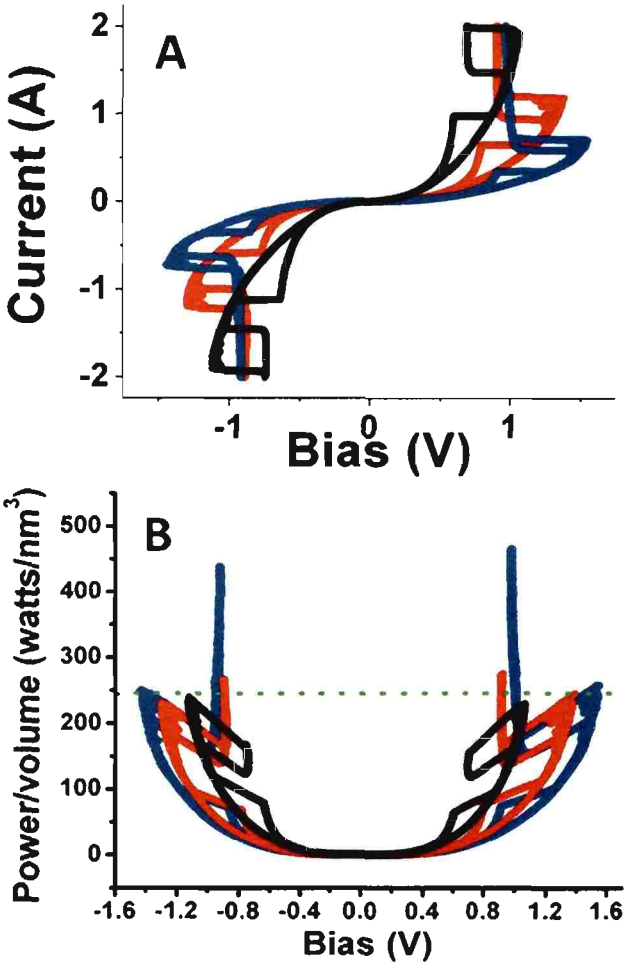

Figure 2. Effect of contact area on resistance switching of a Fe_3O_4 film deposited at -1.01 V vs Ag/AgCl on a SS substrate. (A) iV curves obtained by scanning the applied current at 50 mA/s. (B) Power/volume vs bias plot for the iV curves shown in (A). The blue, red and black curves represent 2.1 mm^2, 3.3 mm^2, 4.4 mm^2 In contact areas. These results indicate that the high-to-low jump occurs at different biases but at the same power density (248 W/nm^3) due to Joule heating.

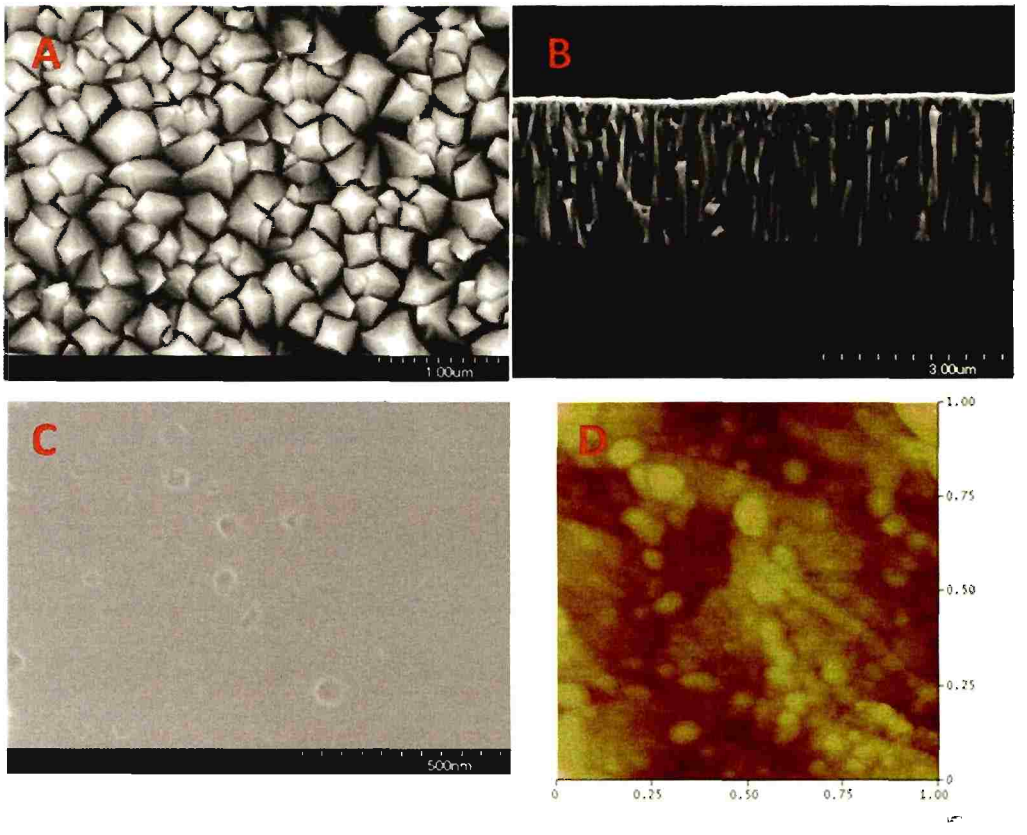

Figure 3. SEM and AFM images of a -1.05 V (vs Ag/AgCl) Fe_3O_4 film deposited on a SS substrate. (A) Top view SEM image of the film. (B) Cross-section of the film which is peeled of onto a microscopic glass slide using superglue. (C) Bottom of the film which is peeled off onto a microscope slide using superglue. (D) Tapping mode AFM image of the bottom of the film peeled off onto a microscope slide.

III. Epitaxial Electrodeposition of Fe_3O_4 on Single-Crystal Ni(111)

Rakesh V. Gudavarthy,[†] Sandeep Gorantla,[‡] Guojun Mu,[†] Elizabeth A. Kulp,[†] Thomas Gemming,[‡] Jürgen Eckert[‡] and Jay A. Switzer[†]

Department of Chemistry and Graduate Center for Materials Research, Missouri University of Science and Technology, Rolla, Missouri 65409-1170

IFW Dresden, P.O. Box 270116, D-01171 Dresden, Germany.

Magnetite, Fe_3O_4, is a promising source of spin polarized carriers because density-functional theory spin resolved density of states calculations have suggested that electrons at the Fermi level are 100% spin-polarized.[1, 2] Being a half-metallic material with 100 % spin polarization, Fe_3O_4 is a good candidate for spin-based devices such as magnetic random access memory (MRAM), magnetic heads, and magnetic sensors.[3] A large magnetoresistance effect has been reported for Fe_3O_4 nanostructures,[4] tunnel junctions,[5] and grain boundaries.[6] Epitaxial growth of Fe_3O_4 has been demonstrated by several groups and several interesting magnetic properties such as superparamagnetism,[7] slow saturation behavior,[8] and local out-of-plane magnetic moments in zero field[8] have been observed. Electrodeposition of epitaxial Fe_3O_4 film on Ni single crystal is a challenge due to the large mismatch (~58 % by comparing the lattice parameters). However, epitaxial electrodeposition and chemical bath deposition has been demonstrated for large mismatch systems, which can be reduced by the formation of coincidence lattices.[9, 10] In this paper, we report the epitaxial electrodeposition of Fe_3O_4 on Ni(111) single crystal in which the lattice mismatch is reduced to 2% by forming a coincidence lattice. The epitaxial film shows resistance switching at 77 K and a magnetoresistance (MR) of 0.8 % at 200 K.

Fe_3O_4 is a ferrimagnetic mixed-valence 3d transition metal oxide that has an inverse spinel structure (space group Fd3m) with a lattice constant of 0.8397 nm. Fe_3O_4 undergoes a metal-to-insulator Verwey transition at $T_v \approx 120$ K,[11] and the Curie temperature of magnetite is 860 K. Above T_v, Fe_3O_4 has a cubic structure with Fe^{3+} occupying tetrahedral sites and Fe^{3+}, Fe^{2+} occupying octahedral sites. Conduction at high temperatures have been attributed to hopping of spin-polarized electrons between

magnetically ordered Fe^{3+} and Fe^{2+} in octahedral sites. However, below T_v, Fe_3O_4 undergoes a first-order phase transition to a monoclinic unit cell through a charge ordering at octahedral sites. This explanation has been under scrutiny,[12, 13] with experiments suggesting some charge ordering in one case [14, 15] and others implying structural changes leading to a change in conductivity. [16, 17]

Epitaxial thin films of Fe_3O_4 have been grown by MBE, [18] pulsed laser deposition, [19] laser ablation, [20] and oxidation of Fe thin films[21] on a variety of substrates. Our group has previously reported the epitaxial electrodeposition of Fe_3O_4 on Au(111), Au(110) and Au(100) single crystals from both acidic and basic solutions.[22-25] In this work, the deposition of epitaxial Fe_3O_4 films was carried out from an alkaline solution containing 43.3 mM iron(III) sulfate, 100 mM TEA (triethanolamine), and 2 M NaOH. The deposition temperature was 80 °C and the deposition potential was -1.01 V vs. Ag/AgCl. The thickness of the film was approximately 300 nm.

The orientation of the Fe_3O_4 film grown on Ni(111) was determined by x-ray diffraction (XRD) using a high-resolution four-circle diffractometer (Philips X'Pert MRD). The Bragg-Brentano scans in Fig. 1(A) probe the out-of-plane orientation of the film. Only the {111} family of peaks of Fe_3O_4 are observed. The lattice parameter of 0.8394 nm determined for the Fe_3O_4 film agrees well with the known bulk lattice parameter, indicating that the majority of the film is relaxed. The in-plane orientation of the film was determined by X-ray pole figures. Fig. 1(B) shows the (311) pole figure of Fe_3O_4 film on the Ni(111) single crystal. The (311) reflections on the pole figure occur at tilt angles, χ, of 29.5°, 58.5°, and 80°. The epitaxial relationship between the film and substrate was determined from azimuthal scans. The azimuthal scans were obtained by selecting the Ni (311) planes at $2\theta = 93.044°$, the Fe_3O_4 (311) planes at $2\theta = 35.456°$, and tilting the sample to $\chi = 29.5°$. The azimuthal scans show that the Fe_3O_4 film is rotated by 180° around the [111] axis relative to the Ni substrate, which gives the epitaxial relationship $Fe_3O_4(111)[\bar{1}10]//Ni(111)[01\bar{1}]$. The azimuthal scans also indicate that the Fe_3O_4 film is 99% oriented anti-parallel to the substrate. The SEM image of Fe_3O_4 on Ni(111) single crystal in Fig. 1(C) is consistent with the pole figure analysis of a film on Ni(111). The micrograph reveals that the majority of the film is dominated by one set of (111) triangular facets of Fe_3O_4. The majority of the facets point upwards with a few

facets rotated 180°. The interface model in Fig. 1(D) is consistent with the epitaxial relationship determined from the X-ray pole figure. In the interface model, Ni atoms are colored gray and O atoms are colored red. The spacing between the adjacent O atoms is 5.937 Å and that of Ni atoms is 4.983 Å. By comparing the spacing between oxygen atoms and Ni atoms, the lattice mismatch is calculated to be 19 % in the $[2\bar{1}\,\bar{1}]$ in-plane direction and also 19 % in the $[1\bar{2}1]$ in-plane direction, which is 60° rotated to the $[2\bar{1}\,\bar{1}]$ direction. The mismatch is dramatically lowered to 2%, when the spacing between 4 unit meshes of O is compared with 8 unit meshes of Ni in the $[2\bar{1}\,\bar{1}]$ and $[1\bar{2}1]$ directions.

The cross-section of the Fe_3O_4/Ni interface was studied by transmission electron microscopy (TEM). Fig. 2(A) shows a conventional bright-field image of Fe_3O_4 grown on Ni, obtained through third order aberration corrected TEM (TITAN^3 80-300, FEI Company) operated at 300 kV. The insets show the selected area diffraction (SAD) patterns of the film and substrate. The SAD patterns of both the film and the substrate indicate a [111] orientation consistent with the XRD. Fig. 2(B) shows a high-resolution TEM (HRTEM) image of the interface. The image reveals that the interface between Fe_3O_4 and Ni is sharp. Fig. 2 (C) shows the SAD pattern obtained from the interface. The pattern shows spots of similar planes from both the film and the substrate. This confirms the epitaxial orientation relationship indicated by the XRD. Also, the spot pattern is indexed using an overlay of calculated diffraction patterns, using JEMS software, of Fe_3O_4 and Ni. The calculated pattern is in agreement with the experimental spot pattern and further supports the epitaxial nature of the interface. In addition, electron energy loss spectroscopy (EELS) was obtained across the interface, as shown in Fig. 2(D). The scan indicated the absence of any excess oxygen, ruling out the possibility of NiO layer.

Magnetic measurements were carried out with a Quantum Design Physical Property Measurement System (PPMS) using the resistivity option for the instrument. Perpendicular transport measurements were carried out by making pressure contacts. Two silver wires were attached one to the Fe_3O_4 film and the other to the Ni surface by pressing indium metal. Fig. 3(A) shows the resistance versus temperature plot of epitaxial Fe_3O_4 film electrodeposited on Ni(111). The plot reveals a sharp increase in resistance after 93 K indicating the Verwey transition. Fig. 3(B) is the differential plot of the resistance versus temperature. The plot shows a dip at 93 K in agreement with Fig. 3(A),

indicative of the Verwey transition temperature. One possible explanation for the shift of Verwey transition from the bulk value of ~120 K to a lower temperature can be attributed to the non-stoichiometric Fe_3O_4 formation as seen by other researchers.[26, 27] We prepare the films by electrochemical reduction of a Fe(III)-TEA (triethanolamine) complex at 80 ^{o}C in stongly alkaline solution. The deposition is believed to occur by electrochemical-chemical (EC) mechanism described by Eq. 1 and 2.

$$Fe(TEA)^{3+} + e^{-} \rightarrow Fe^{2+} + TEA \quad (1)$$

$$Fe^{2+} + 2Fe(TEA)^{3+} + 8OH^{-} \rightarrow Fe_3O_4 + 2TEA + 4H_2O \quad (2)$$

Because of the EC nature of the deposition reaction, it is possible to control the composition of the film through the applied potential. At low overpotentials at which j = 0, the surface concentration of $Fe(TEA)^{3+}$ should be equal to the bulk concentration, whereas at high overpotential at which $j = j_l$ the surface concentration should approach zero. Hence the material should have excess of Fe^{3+} at low overpotential and an excess of Fe^{2+} at high over potential.[25, 29, 30] A linear sweep voltammogram run in the deposition bath indicates that the reduction begins at -1.01 V (~2 mA/cm^2) and reaches a limiting current at -1.2 V (~15 mA/cm^2) vs. Ag/AgCl. Stoichiometric Fe_3O_4 can be produced at -1.05 V vs. Ag/AgCl. That would imply that the films grown at -1.01 V would have excess of Fe(III) in them, resulting in non-stoichiometric Fe_3O_4 film formation. For such films, the Verwey temperature is shifted to a lower value. Fig. 2(C) shows the magnetoresistance (MR) scan obtained on a electrodeposited Fe_3O_4 film on Ni(111) at 200 K. A magnetoresistance value of -0.8 % was obtained for the film. It is expected that a magnetic tunnel junction can be formed with Fe_3O_4/NiO/Ni interface with NiO layer serving as antiferromagnetic layer in the ferrimagnetic/antiferromagnetic/ferromagnetic sandwich. Such type of couplings in metals has shown giant magnetoresistance effect (GMR).[30] However, the electrodeposited Fe_3O_4 films on Ni(111) do not show any significant TMR or GMR effect. This is consistent with the absence of NiO at the interface as confirmed by our TEM analysis.

A particularly interesting feature that the electrodeposited magnetite films exhibit is resistance-switching during perpendicular transport measurements.[28, 29] Recently, we

have shown that superlattices in the magnetite system and polycrystalline magnetite films exhibit resistance switching.[28, 29] It was shown that the films with non-stoichiometric Fe_3O_4 exhibit both low-to-high and high-to-low jumps.[29] Figure 3(D) shows the iV curve obtained at 77 K by sweeping the current from 0 to 2 A at 50 mA/s for a -1.01 V Fe_3O_4 film on Ni(111). During the forward scan it is seen that the film undergoes a low-to-high resistance jump at 1.5 V irrespective of the sign of the bias applied. Following the low-to-high resistance jump, we observe oscillation in the bias. Low-to-high resistance switching has previously been reported in Fe_3O_4 and the origin of such switching has been attributed to oxidation of Fe_3O_4 to γ-Fe_2O_3 at the anode.[32] We believe that in our case also the low-to-high resistance occurs due to the oxidation of Fe_3O_4 to γ-Fe_2O_3 under the contact. As reported before, we do not observe the phase transition jump in our epitaxial films.[28, 29] It was shown previously that nanophase magnetite is critical for the phase transition jump to occur.[28, 31] Bulk magnetite films and single crystals show high-to-low resistance switching (phase transition jump) only at very high bias (~10 V).[33] Similarly, the Fe_3O_4 films deposited on the Ni(111) single crystal do not show the phase transition jump.

In conclusion, we have demonstrated that epitaxial films of Fe_3O_4 can be electrodeposited onto a Ni(111) single crystal. The films grow with a [111] out-of-plane orientation, with the in-plane $[\bar{1}10]$ direction of Fe_3O_4 aligned with the $[01\bar{1}]$ direction of Ni(111) . The TEM results are in agreement with XRD results. The EELS scan shows that there is no NiO interlayer between the electrodeposited Fe_3O_4 film and the Ni(111) substrate. The Fe_3O_4 film on Ni(111) has a Verwey transition temperature which is shifted to a lower value of 93 K from the bulk value of 120 K. We believe that this shift is due to the non-stoichiometry of Fe_3O_4. A magnetoresistance value of 0.8% is obtained at 200 K. The films of Fe_3O_4 on Ni(111) exhibit high-to-low resistance switching.

Acknowledgement: The authors would like to thank Dr. Eric Bohannan for his useful comments and discussions and Dina Lohse for TEM specimen preparation. The work was supported by Department of Energy Grant DE-FC07-03ID14509.

REFERENCES

1. Z. Zhang and S. Satpathy, Phys. Rev. B **1991**, *44*, 13319.

2. V. I. Anisimov, I. S. Elfimov, N. Hamada, and K. Terakura, Phys. Rev. B **1996**, *54*, 4387.

3. M. Julliere, Phys. Lett. **1975**, *54A*, 225.

4. J. J. Versluijs, M. A. Bari, and J. M. D. Coey, Phys. Rev. Lett. **2001**, *87*, 026601.

5. P. Seneor, A. Fert, J. –L. Maurice, F. Montaigne, F. Petroff, and A. Vaures, Appl. Phys. Lett. **1999**, *74*, 4017.

6. P. Chen, D. Y. Xing, Y. M. Du, J. M. Zhu, and D. Feng, Phys. Rev. Lett. **2001**, *87*, 107202.

7. F. C. Voogt, T. T. M. Palstra, L. Niesen, O. C. Rogojanu, M. A. James, and T. Hibma, Phys. Rev. B **1998**, *57*, R8107.

8. D. T. Margulies, F. T. Parker, F. E. Spada, R. S. Goldman, J. Li, R. Sinclair, and A. E. Berkowitz, Phys. Rev. B **1996**, *53*, 9175.

9. S. Nakanishi, G. Lu, H. M. Kothari, E. W. Bohannan, and J. A. Switzer, J. Am. Chem. Soc. **2003**, *123*, 14998.

10. G. Mu, R. V. Gudavarthy, E. A. Kulp, and J. A. Switzer, Chem. Mater. **2009**, *21*, 3960.

11. E. J. W. Verwey, Nature **1939**, *144*, 327.

12. F. Walz, J. Phys. Condens. Mater. **2002**, *14*, R285.

13. J. Gracia and G. Subias, J. Phys. Condens. Mater **2004**, *16*, R145.

14. D. J. Huang, H, -J. Lin, J. Okamoto, K. S. Chao, H. –T. Jeng, G. Y. Guo, C. –H. Hsu, C. –M. Huang, D. C. Ling, W. B. Wu, C. S. Yang, and C. T. Chen, Phys. Rev. Lett. **2006**, *96*, 096401.

15. E. Nazarenko, J. E. Lorenzo, Y. Joly, J. L. Hoeau, D. Mannix, and C. Marin, Phys. Rev. Lett. **2006**, *97*, 056403.

16. G. Subias, J. Gracia, J. Blasco, M. G. Proietti, H. Renevier, and M. C. Sanchez, Phys. Rev. Lett. **2004**, *93*, 156408.

17. G. Kh. Rozenberg, M. P. Pasternak, W. M. Xu, Y. Amiel, M. Hanfland, M. Amboage, R. D. Taylor, and R. Jeanloz, Phys. Rev. Lett. **2006**, *96*, 045705.

18. J. F. Anderson, M. Kuhn, U. Diebold, K. Shaw, P. Stoyanov, and D. Lind, Phys. Rev. B **2002**, *56*, 9902.

19. G. Q. Gong, A. Gupta, G. Xiao, W. Qian, and V. P. Dravid, Phys. Rev. B **1997**, *56*, 5096.

20. R. J. Kennedy and P. A. Stampe, J. Phys. D: Appl. Phys. **1999**, *32*, 16.

21. W. Weiss and M. Ritter Phys. Rev. B **1999**, *59*, 5201.

22. M. P. Nikiforov, A. A. Vertegel, M. G. Shumsky, and J. A. Switzer, Adv. Mater. **2000**, *12*, 1351.

23. T. A. Sorenson, S. A. Morton, G. D. Waddill, and J. A. Switzer, J. Am. Chem. Soc. **2002**, *124*, 7604.

24. H. M. Kothari, E. A. Kulp, S. J. Limmer, P. Poizot, E. W. Bohannan, and J. A. Switzer, J. Mater. Res. **2006**, *21*, 293.

25. E. A. Kulp, H. M. Kothari, S. J. Limmer, J. Yang, R. V. Gudavarthy, E. W. Bohannan, J. A. Switzer, Chem. Mater. **2009**, *21*, 5502.

26. X. Z. Kakol and J. M. Honig, Phys. Rev. B **1989**, ***40***, 9090.

27. Y. J. P. Shepherd, J. W. Koenitzer, R. Aragón, C. J. Sandberg, and J. M. Honig, Phys. Rev. B **1985**, ***31***, 1107.

28. J. A. Switzer, R. V. Gudavarthy, E. A. Kulp, G. Mu, Z. He, and A. Wessel, J. Am. Chem. Soc. **2010**, *132*, 1258.

29. R. V. Gudavarthy, A. S. Miller, E. W. Bohannan, E. A. Kulp, Z. He, and J. A. Switzer, Electrochem. Acta. Submitted (2010).

30. G. Binasch, P. Grünberg, F. Sauernbach, and W. Zinn, Phys. Rev. B **1989**, *39*, 4828.

31. S. Lee, A. Fursina, J. T. Mayo, C. T. Yavuz, V. L. Colvin, R. G. S. Sofin, I. V. Shevts, D. Natelson, Nat. Mater. **2008**, *7*, 130.

32. A. Odagawa, Y. Katoh, Y. Kanzawa, Z. Wei, T. Mikawa, S. Muraoka, T. Takagi, Appl. Phys. Lett. **2007**, *91*, 133503.

33. M. N. Baibich, J. Broto, A. Fert, F. N. Van Dau, F. Petroff, P. Eitenne, G. Creuzer, A. Friederich, and J. Chazelas, Phys. Rev. Lett. **1988**, *61*, 2472.

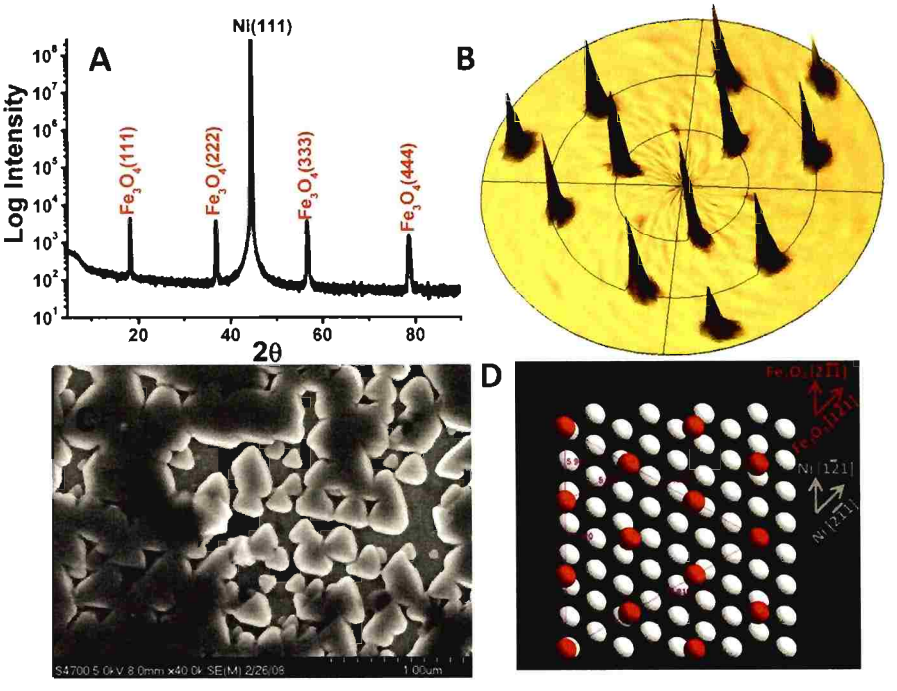

FIG. 1. XRD, SEM, and interface model for epitaxial Fe_3O_4 film Ni(111). (A) X-ray 2θ scan of the film. Only the {111} family planes of Fe_3O_4 are observed. (B) (311) pole figure of Fe_3O_4 on Ni(111), (C) SEM micrograph showing the triangular facets of Fe_3O_4 on Ni(111) and (D) an interface model for Fe_3O_4(111) on Ni(111). The Ni atoms are colored grey, and the O atoms are colored red.

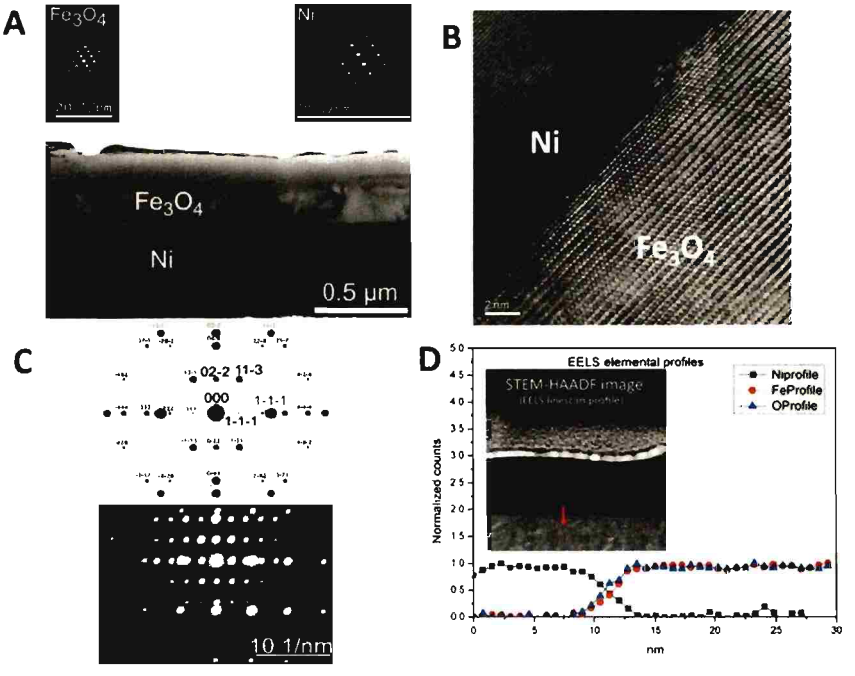

FIG. 2. Cross-sectional TEM characterization of the Fe_3O_4 film on Ni(111) single crystal. (A) Conventional bright-field TEM image showing the sharp interface, insets show the corresponding diffraction pattern (scalebar is 20 nm^{-1}). (B) HRTEM image of the Fe_3O_4/Ni interface; shows the epitaxial growth of Fe_3O_4 on Ni substrate. This clearly shows that the two materials are not separated by any diffused interlayer (Image processing: Noise filtered through fast fourier transformation). (C) The calculated diffraction patterns overlay (above) in agreement with experimental selected area diffraction (SAD) pattern of the interface between Fe_3O_4 and Ni (below) (scalebar is 5 nm^{-1}). (D) EELS line scan on the Fe_3O_4/Ni interface shows that there is no excess oxygen at the interface.

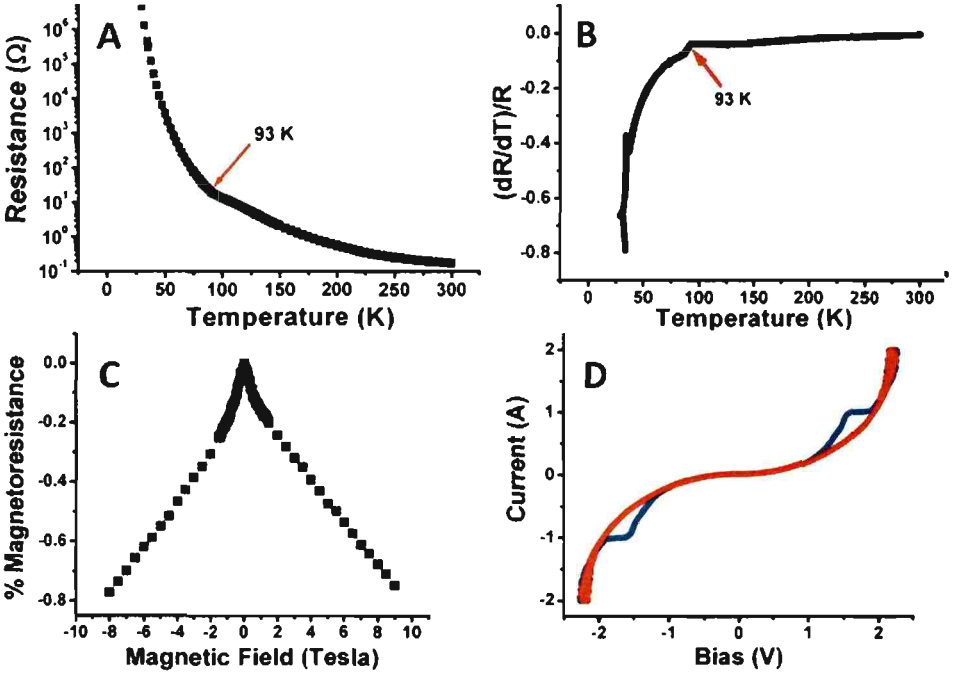

FIG. 3. Magnetic and electrical properties of an epitaxial film of Fe_3O_4 on Ni(111). (A) Resistance vs. temperature curve indicating a Verwey transition at 93 K. (B) Differential plot normalized with resistance which indicates a clear Verwey transition at 93 K. (C) Magnetoresistance plot at 200 K for a Fe_3O_4 film deposited on Ni(111). (D) iV curve scanning the applied current at 50 mA/s. Blue line indicates forward sweep and red lines indicates backward sweep.

IV. Epitaxial electrodeposition of chiral CuO films from copper(II) complexes of malic acid on Cu(111) and Cu(110) single crystals†

Rakesh V. Gudavarthy,*[a] Niharika Burla,[a] Elizabeth A. Kulp,[a] Steven J. Limmer[a], Ekkehard Sinn,[a, b] and Jay A. Switzer[a]

ABSTRACT

Chiral films of CuO were anodically electrodeposited onto Cu(111) and Cu(110) single crystals from alkaline solutions of Cu(II) complexed with the malate ion. The chirality of the film was directed by the chiral solution precursor. X-ray diffraction pole figures and stereographic projections were used to determine the absolute configuration of the films. CuO films grown on Cu(111) from L-malate had $(\bar{1}\,1\,1)$ and (311) orientations and the films grown from D-malate had $(1\,\bar{1}\,\bar{1})$ and $(\bar{3}\,\bar{1}\,\bar{1})$ orientations. CuO films grown on Cu(110) from L-malate had (110) and $(3\,1\,\bar{1})$ orientations, whereas the films grown from D-malate deposition bath had $(\bar{1}\,\bar{1}\,0)$ and $(\bar{3}\,\bar{1}\,1)$ orientations. The CuO films grown from a racemic malate bath showed only the $(\bar{1}\,1\,1)$ and $(1\,\bar{1}\,\bar{1})$ orientations on Cu(111) and (110) and $(\bar{1}\,\bar{1}\,0)$ orientations on Cu(110). Crystals of L-, D- and racemic bis(malato)copper(II) dihydrate complexes were grown and analyzed using X-ray crystallography. The chiral complexes of bis(malato)copper(II) dihydrate were each found to belong to the monoclinic space group $P2_1$ where as the racemic complex belonged to the centrosymmetric $P2_1/c$ space group. The chiral complexes form coordination polymer along the b-axis, in which the carboxyl group from each complex links to the axial site of an adjacent Cu(II) complex. In the complex produced from the racemic mixture, the coordination polymer does not form.

INTRODUCTION

Chirality in nature has inspired research on the production of enantiospecific surfaces for chiral catalysts and sensors for potential use in pharmaceutical, agrochemical, and related industries.[1, 2] One method to produce chiral surfaces is to cleave an achiral face-centered cubic metal surface at small angles exposing the kink sites

of high Miller index surfaces. [3, 4] Scholl et al.[5] showed enantiospecific adsorption of chiral molecules on Pt(643) surfaces by Monte Carlo simulations. Attard et al.[6] confirmed chiral recognition of such surfaces by demonstrating enantiospecific electrochemical oxidation of glucose on Pt(643) and its enantiomer, $Pt(\overline{6}\overline{4}\overline{3})$. In a different process, chiral organic molecules are adsorbed on achiral surfaces rendering the surface chiral.[7-12] Raval[7] et al. show that adsorption of pure (R,R)-tartaric acid on copper substrate creates a chiral template that destroys the mirror symmetry planes of the copper surface and exposes the copper atoms in chiral spaces.

Cupric oxide (CuO) has a monoclinic structure with a centrosymmetric space group, C2/c.[13-15] CuO thin films have been prepared by several techniques such as electrodeposition[16-18], sol-gel synthesis[19], MBE[20], MOCVD[21], thermal[22] and anodic oxidation. [23] Our approach to generating epitaxial chiral films is through the electrodeposition of CuO. Previously, we have electrodeposited chiral CuO films on achiral single crystals using chiral precursors such as tartaric[24] and amino acids.[25] In these studies, we have shown that the chirality of the film is controlled by the chirality of the precursors in the deposition bath. The absolute chiral orientations of the CuO films were verified by x-ray diffraction pole figures and stereographic projections.[24-27] Widmer et.al[28] has since verified the surface chirality of these films by X-ray photoelectron diffraction. In previous studies, we have shown that chiral surfaces of the electrodeposited CuO films can act as chiral sensors.[29]

In this paper, we extend our work to show that malic acid, a dicarboxylic acid with one chiral center, can also direct the chirality of deposited CuO films on Cu(111) and Cu(110). We observe that films grown from L-tartaric acid and L-malic acid produce opposite enantiomorphs. Previously copper(II) complexes with racemic malic acid, chiral and racemic tartaric acid have been studied using X-ray crystallography by other groups.[30, 31] In other studies it has been shown that Co(II)[32] and Zn(II)[33] form complexes with L-(-)-malic acid [(S)-(-)-hydroxysuccinic acid] and crystallize in monoclinic space group $P2_1$. In this paper, X-ray crystallographic data for copper(II) complexes with L-, D- and DL- malic acid has been studied to help provide insight into the mechanism of chiral electrodeposition. The complexes synthesized in the presence of chiral malic acid

crystallized in monoclinic space group $P2_1$. However, the racemic complex crystallized in a centrosymmetric space group $P2_1/c$.

EXPERIMENTAL SECTION

Synthesis of chiral and racemic copper(II)malate single crystals

Crystals of copper(II) malate were grown from a saturated solution containing malic acid and copper(II)oxide. CuO powder was added to a supersaturated solution of malic acid and the solution was stirred and heated for a period of 12 hrs. Heating helped the reaction go faster. Undissolved CuO was filtered out and the clear blue solution was then allowed to undergo batch crystallization at room temperature, free of any mechanical vibration and disturbances. Blue crystals with different sizes were seen to form within a period of two days. Thus obtained crystals were then rinsed with deionized water, air dried, and the X-ray quality crystals were chosen for crystal structure analysis. CuO powder used in the synthesis was purchased from Aldrich, and the L- and D- malic acid were purchased from Alfa Aesar. The single enantiomers had an optical purity 98+% enantiomeric excess and all reagents were used without further purification.

X-ray single crystal analysis

The crystallographic data were collected on the blue single crystals of L-, D- and racemic bis(malato)copper(II) dihydrate complexes $Cu[COOCH(OH)CH_2CO(OH)]_2.2H_2O$ with a Bruker Smart Apex CCD diffractometer using Mo radiation (λ = 0.71073Å) and a graphite monochromator. The collected data were reduced using the SAINT program, [34] and multi-scan absorption corrections were performed using the SADABS program.[35] The structures were solved by the heavy-atom method and refined by the full-matrix least-squares procedure on the peak intensities (F^2) using the SHELXTL version 5.1.[36] All non-hydrogen atoms were refined anisotropically and hydrogen atoms were inserted in their calculated positions and were constrained to ride on their parent atoms. Comparative crystallographic data for the monoclinic complexes refined by the least squares is summarized in Table 1. Selected bond lengths and angles are given in the supplementary material. Crystallographic data for Cu(II)L-malate dihydrate, Cu(II)D-malate dihydrate and Cu(II)DL-malate dihydrate have been

deposited with the Cambridge Crystallographic Data Center (CCDC 634735, CCDC 634400, and CCDC 634933).

Surface preparation of copper single crystals

Electrochemical experiments were carried out using an EG&G applied research (PAR) model 273A potentiostat/galvanostat. The cell consisted of a platinum counter electrode and a standard calomel reference electrode (SCE). The working electrode were single crystals of Cu(111) and Cu(110) which were purchased from Monocrystals company (diameter 10 mm and thickness 2 mm). A Cu wire fitted around the single crystal served as an electrical contact to the working electrode. The working electrode was placed in the solution using the meniscus method. The Cu single crystals were electropolished prior to deposition. Electropolishing was carried out in a solution consisting of 67 vol % orthophosphoric acid, by immersing the working electrode (anode) at an angle of 45^{o} and a constant potential of 1.45 V vs. SCE was applied for 45 seconds. Native oxides present on the crystals were removed by treating the crystal with 0.1M $HClO_4$.

Deposition of CuO using malic acid

Thin films of CuO were deposited on Cu(111) and Cu(110) single crystals from a highly alkaline solution of copper(II) complexed with malic acid. The deposition bath consisted of 50 mM $CuSO_4.5H_2O$, 150 mM malic acid and 4 M NaOH. L-(-)-malic acid [(S)-(-)-hydroxysuccinic acid], D-(+)- malic acid [(R) –(+)-hydroxysuccinic acid] and DL-malic acid were purchased from Alfa Aesar. The single enantiomers had an optical purity 98+% ee and all reagents were used without further purification. The electrodeposition was performed using a constant applied potential of +0.35 V vs. SCE for 900 sec at 30 ^{o}C. Around 1 C/cm of charge passed during the deposition time.

X-ray Diffraction measurements on the electrodeposited films

X-ray diffraction measurements were performed on the electrodeposited CuO films with a high-resolution Philips X'Pert MRD diffractometer. For θ-2θ scans the primary optics module was a combination Gobel mirror and a crystal Ge (220) 2-bounce hybrid monochromator, and the secondary optics module was a 0.18^{o} parallel plate collimator. The hybrid monochromator produces pure Cu $K\alpha_1$ radiation (λ = 0.1540562 nm) with a divergence of 25 arc seconds. Pole figures were obtained in point-focus mode

using a crossed-slit collimator as the primary optics. Stereographic projections were obtained using CaRIne Crystallography software V. 3.0.

RESULTS AND DISCUSSION

Figure 1 shows the θ-2θ X-ray diffraction scans for two films grown from Cu(II)-malate solution on Cu(111). Figure 1(A) shows the scan for the film obtained from L-(-)-malate solution while Figure 1(B) shows the scan obtained from D-(+)-malate. The θ-2θ patterns for both the films are essentially identical, with peaks observed at 35.57° (d = 0.2525 nm), 38.75° (d = 0.2325 nm) and at 73.30° (d = 0.1305 nm). Figure 1(C) shows the scan obtained from racemic malate has only one peak at 35.57° which can assigned to either $(1\,\bar{1}\,\bar{1})$ or $(\bar{1}\,11)$. The Cu(111) substrate peak is observed at 44.27°. Indexing the peaks is problematic for CuO as the peak at 35.57° can be assigned to either CuO $(1\,\bar{1}\,\bar{1})$ or $(\bar{1}\,11)$ because the d-spacing for the two planes are equivalent. Table 1 lists all the set of planes corresponding to the peaks observed in Figure 1 that have the same d-spacing.

Based on the listings in Table 1, the peaks could be assigned as any one of the four orientations. It is impossible to distinguish between the orientations based on the θ-2θ scans. In addition, we have shown previously that for CuO, all planes (hkl) and $(\bar{h}\bar{k}\bar{l})$ where k=0 are achiral. All other planes are chiral.[37] For all planes (hkl) the enantiomeric pair is $(\bar{h}\bar{k}\bar{l})$. All the planes in Table 1 corresponding to peaks observed in Figure 1 are chiral. The absolute configuration of the chiral films can be determined by X-ray pole figure analysis. Pole figures are obtained by selecting a reflection to probe while measuring the diffracted intensity as a function of sample tilt (χ) and rotation (Φ). The sample is tilted from a $\chi = 0^\circ$ to 90° for each tilt angle and is rotated through azimuthal angles, Φ, of 0 to 360°. The plane with highest intensity in the powder pattern is usually probed, so as to achieve highest diffracted intensity. Figure 2(A), 2(B), and 2(C) shows CuO(111) pole figures for the films grown from L-malate, D-malate and DL-malate deposition bath on Cu(111) single crystal. The d-spacing for CuO(111) and (200) are sufficiently close so that resolution of these planes is difficult. We must therefore account

for the presence of the (200) reflections in the pole figures as well as the (111) reflections.

To interpret pole figures, we use stereographic projections. Figures 3(A) and 3(B) shows the $(\bar{1}\,1\,1)$ and $(1\,\bar{1}\,\bar{1})$ stereographic projections of monoclinic CuO. The radial direction is the tilt angle, χ, while the azimuthal angle, φ, is the rotation of the sample about the axis. The positions of CuO{111} and CuO{200} reflections are specified. Figure 3(A) shows that for the $(\bar{1}\,1\,1)$ orientation, reflections from the $(\bar{1}\,1\,\bar{1})$ plane at a χ of 57°, and the (111) planes at a χ of 63°, are separated azimuthally by 115° rotated counterclockwise ($\Delta\varphi$ = -115°). Figure 3(B) shows that for $(1\,\bar{1}\,\bar{1})$ orientation, reflections from the $(1\,\bar{1}\,1)$ plane at χ = 57° and the $(\bar{1}\,\bar{1}\,\bar{1})$ plane at χ = 63° are separated azimuthally by 115° rotated clockwise ($\Delta\varphi$ = 115°). The calculated interplanar angles obtained from stereographic projections correspond with the measured interplanar angles of the pole figures. Figure 2(A) and 2(B) also show reflections at χ = 27°. These reflections can be explained by figures 3(C) and 3(D). Figure 3(C) shows that for the (311) orientation, reflections from the (111) plane at a χ of 27.19°, and the $(1\,\bar{1}\,1)$ plane at a χ of 68.14°, are separated azimuthally by 125.18° rotated counterclockwise. Figure 3(D) shows that for the $(\bar{3}\,\bar{1}\,\bar{1})$ orientation, reflections from the $(\bar{1}\,\bar{1}\,\bar{1})$ plane at χ of 27.19°, and the $(\bar{1}\,1\,\bar{1})$ plane at a χ of 68.14°, are separated azimuthally by 125.18° rotated clockwise. Figures 3(A) and 3(C) clearly explains the pole figure of Figure 2(A) and confirms the presence of $(\bar{1}\,1\,1)$ and (311) orientations for the film grown from L-malate deposition bath. Similarly, Figures 3(B) and 3(D) explain the pole figure of Figure 2(B) and confirm the presence of $(1\,\bar{1}\,\bar{1})$ and $(\bar{3}\,\bar{1}\,\bar{1})$ orientations for the film grown from the D-malate deposition bath. Figure 2(C) shows the CuO(111) pole figure for a CuO film grown from the DL-malate deposition bath. Figure 2C shows no reflections at χ = 27°, indicating the absence of both (311) and $(\bar{3}\,\bar{1}\,\bar{1})$ orientations. This result is consistent with Figure 3C which shows no peak at 73.342° for (311) or $(\bar{3}\,\bar{1}\,\bar{1})$. Reflection at χ = 63° correspond to both $(\bar{1}\,1\,1)$ and $(1\,\bar{1}\,\bar{1})$ orientations. Azimuthal scans extracted from the (111) pole figures at χ = 63° with the azimuthal angle, φ, varying from 60° to 120° (not shown)

indicates a little higher preference for $(\bar{1}\,1\,1)$ orientation. Figures 4(A), 4(B) and 4(C) show the microstructures as observed by scanning electron microscope (SEM) for the films grown from L-malate, D-malate and DL-malate deposition baths on Cu(111) single crystals. The individual crystallites have a rice grain structure arranged in triangular pattern consistent with the X-ray diffraction results. Multiple domains of each orientation are rotated by 120°. The SEM image of the film grown from L-malate deposition bath shows that the grains are approximately 300 nm long and 60 nm wide, while the grains of the film grown from D-malate deposition bath are approximately 350 nm long and 100 nm wide. The film grown from DL-malate bath had 350 nm size particles as well as 300 nm size particles. Micrographs do not show the chirality of the films.

Under the same electrochemical conditions, CuO films were also grown on Cu(110) substrate. Figure 5 shows θ-2θ XRD scans for films grown from Cu(II) malate solutions on Cu (110). Figure 5(A) shows the scan for the film obtained from a deposition bath consisting of L-malate while Figure 5(B) shows the scan obtained from D-malate deposition bath. The θ-2θ scans are essentially identical for both the films, with peaks at 2θ of 32.40°, 67.90° and 66.28°. The Cu(220) substrate peak is observed at 2θ =32.12°. The peak at 53.2° in Figure 5(B) is an impurity peak and is observed with the bare Cu single crystal. To index these patterns, pole figures and stereographic projections are used to distinguish between the CuO(110) and $(\bar{1}\,\bar{1}\,0)$ orientations. Figures 6(A), 6(B) and 6(C) show the CuO(111) pole figure for a film of CuO deposited from L-malate, D-malate and DL malate deposition bath on Cu(110). It is evident from the Figures 6(A) and 6(B) that they are nonsuperimposable mirror images of one another and rotate in opposite directions. The stereographic projection in Figure 7(A) shows that for the (110) orientation, reflections from the $(\bar{1}\,1\,\bar{1})$ plane at χ = 78.54° and the (111) plane at χ = 27.16° are separated azimuthally by 125.15° rotated counterclockwise. Figure 7(B) shows that for the $(\bar{1}\,\bar{1}\,0)$ orientation, reflections from the $(1\,\bar{1}\,1)$ plane is at χ = 78.54° and the $(\bar{1}\,\bar{1}\,\bar{1})$ plane is at χ = 27.16° are separated azimuthally by 125.15° rotated clockwise. Figures 6(A) and 6(B) also show tail-like reflections at χ = 48.84° and at χ =29.59°. These reflections can be explained by the stereographic projection in Figures 7(C) and 7(D). Figure 7(C) shows that for the $(31\,\bar{1})$ orientation, reflections from the (111) plane occur

at a tilt $\chi = 48.84^{\circ}$ and reflections from (100) planes are seen at $\chi = 29.59^{\circ}$. Figure 7(D) shows that for the $(\bar{3}\,\bar{1}\,1)$ orientation the $(\bar{1}\,\bar{1}\,\bar{1})$ planes occur at $\chi = 48.84^{\circ}$ and reflections from $(\bar{1}\,00)$ planes are seen at $\chi = 29.59^{\circ}$. Stereographic projections in Figures 7(A) and 7(C) explain the pole figure in Figure 6A and confirm the presence of (110) and -orientations for the film grown from L-malate deposition bath. Similarly Figures 7(B) and 7(D) explain the pole figure in Figure 6(B) and confirm the presence of $(\bar{1}\,\bar{1}\,0)$ and $(\bar{3}\,\bar{1}\,1)$ orientations for the film grown from D-malate deposition bath. Figure 6(C) shows the CuO(111) pole figure for a CuO film grown from DL-malate deposition bath. Pole figure indicates presence of both (110) and $(\bar{1}\,\bar{1}\,0)$ orientations with a slightly higher preference for the (110) orientation.

Figures 8(A), 8(B) and 8(C) show the SEM images of the CuO films grown from L-malate, D-malate and DL-malate deposition bath on Cu(110) single crystal. The individual crystallites have a rice grain structure. The SEM image of the film grown from a L-malate deposition bath shows that the grains are approximately 300 nm long and 60 nm wide, while the film grown from a D-malate deposition bath are approximately 350 nm long and 100 nm wide. The film grown from DL-malate bath had particles of both sizes.

It was interesting to compare the orientations of electrodeposited films from L (+)- tartaric acid and L (-)- malic acid on the Cu(111) single crystal. Figure 9(A) shows the CuO(111) pole figure for a film grown from the L-(+)- tartrate bath, while Figure 9(B) shows the CuO(111) pole figure for the film grown from the L-(-)-malate deposition bath. It is evident from Figures 9(A) and 9(B) that both the pole figures are nonsuperimposable mirror images of each other. Opposite enantiomorphs are obtained even though the films are both grown from the L enantiomers. The use of L- and D notation results in an arbitrary assignment of configuration.

Absolute configuration to the chiral molecules can be assigned using Cahn Ingold Prelog (CIP) sequence rules. CIP uses R and S notation; an R isomer can be either dextrorotatory or levorotatory, depending upon its exact constituents. Utilizing this method, we find that L-(+)-tartaric acid can be assigned (R,R) and L-(-)-malic acid can be assigned (S) configuration respectively. It was interesting to observe that films grown

from both R versions of tartaric acid and malic acid resulted in CuO $(1\,\bar{1}\,\bar{1})$ orientation on Cu(111), while the S version of each resulted in a CuO $(\bar{1}\,11)$ orientation. Besides CuO $(1\,\bar{1}\,\bar{1})$ or CuO $(\bar{1}\,11)$ orientations, a film grown from malic acid results in forming a second orientation.

Surface imprinting results in chiral surfaces.[37] Once the chiral molecule is adsorbed on the substrate it reconstructs the surface and surface remains intact even on removal of the adsorbed chiral molecule.[38, 39] On the other hand chiral templating is induced by adsorbing chiral molecules on achiral surfaces without surface reconstruction. Raval and co-workers have shown chiral templating on Cu(110) in which case adsorption of (R,R)-tartaric acid on Cu(110) does not show any surface reconstruction.[7] As discussed in our previous paper, [25] it is reasonable to expect a chiral molecule or the metal complex to adsorb on the surface and break its symmetry. Crystals of Cu(II)-malate were grown to understand this phenomenon better. The crystals were grown at pH=1.5 as it is very difficult to grow the crystals from alkaline solutions. Systematic absences indicated the monoclinic space groups: $P2_1$ for the chiral complexes and centrosymmetric $P2_1/c$ for the racemic. Figures 1A, 1B and 1C give the perspective views of the fragments of complex monomers together with the atomic labeling system.

The chiral complexes were identified as copper(II)L-malate and copper(II)D-malate based on the position of the hydrogen atoms (H2 and H6) relative to their carbon atoms at the chiral center (C2 and C6). The complexes grown from L-malic acid contain two L-malate ligands while the complexes grown from D-malic acid contain two D-malate ligand. Racemic complex molecules contain one L-malate ligand and one D-malate ligand making it a copper(II)DL-malate.

The chiral complexes of bis(malato)copper(II) dihydrate were each found to belong to the monoclinic space group $P2_1$ (#4). The structures (A) and (B) in Figure 10 represent the individual L- and D-copper(II)malate complex fragments and the lattice parameters along with other refinement data are presented in the Table 1.

Figure 11(A) represents the packing diagram showing the polymerization of a chiral Cu(II)malate dihydrate complex. Both L- and D- chiral complexes polymerize in a similar fashion. Each unit cell contains two chiral copper(II)malate dihydrate complexes

where each copper is coordinated to two malate ligands of the same chirality via one hydroxyl oxygen atom and one carboxyl oxygen atom. The ligands bond trans to each other to complete an approximate square planar geometry. One of the ligands forms a weaker bond (2.336Å) above the square coordination with the next copper(II) ion. This forms a square pyramid via one oxygen of its other carboxyl group (O4), thus linking the adjacent coppers along the b-axis in a helical fashion. The link between adjacent strands is 2.769 Å i.e. between the carboxyl (010) of one strand to the bottom of the square pyramid of the next copper(II) ion. The hydroxyl oxygen bonded to copper retains its proton. Hence, the copper - hydroxyl oxygen bond (1.962 Å) is slightly longer than the Cu - carboxyl oxygen bond (1.910 Å) and the average distance Cu-O is 1.937(2) Å. The water molecules are hydrogen bonded to the carboxyl oxygen (O2) in one ligand and hydroxyl oxygen (O8) in the other and do not participate in polymerization. Also, there is no coordination between the copper ions and water molecules in the chiral complexes.

Finally, the complex grown from racemic Cu(II)-malate crystallized in a centrosymmetric space group $P2_1/c$ (#14) with copper atoms at the inversion center. Figure 11(B) represents packing of the racemic Cu(II) malate complex monomers. Each unit cell contains two centrosymmetric copper(II)malate molecules. Unlike the chiral complexes, the structure consists of discrete molecules, in which each copper ion bonds to a D- and an L-malate ion by one hydroxyl oxygen atom and one carboxyl oxygen atom with the formation of two almost planar rings. The hydroxyl oxygen bonded to copper retained its proton just as in the case of chiral complexes. The water molecules brought the planar coordination of copper close to bipyramidal. These complexes are joined by a two-dimensional system of hydrogen bonds, and adjacent layers are arranged in a parallel fashion. Complexes within the layer are bonded strongly by the hydroxyl protons. The hydroxyl group forms a strong hydrogen bond with the oxygen atom of a neighboring complex from another layer. The dotted lines indicate hydrogen bonds and water molecules do not participate in any bonding between the complexes.

At this point the mechanism of chiral film formation is not clear. One possibility could be the chiral complexes formed in the solution are initially adsorbed on the surface and imprint chirality on the surface. Studies show the adsorption of tartaric, [7] cystiene, [41] and styerene[42] molecules on the surface of Cu, Au and Si but there have been no studies

on adsorption of copper tartrate and copper malate complexes on achiral substrates. Our x-ray crystal structures indicate that the chiral complexes form coordination polymers along the b-axis, in which the carboxyl group from each complex links to the axial site of an adjacent Cu(II) complex. In the complex produced from the racemic mixture, the coordination polymer does not form. It is a possibility that these coordination polymers of chiral complexes are adsorbed on the surface of the substrate and leave chiral imprints. In case of racemic mixture, the adsorption would be monomer by monomer instead of an entire polymer.

CONCLUSION

Chiral films of CuO were electrodeposited onto Cu(111) and Cu(110) single crystals from alkaline solutions of Cu(II) complexed with malate. Chirality to the film was directed by the chiral solution precursor present in the solution. CuO films grown on Cu(111) from L-malate had $(\bar{1}\,1\,1)$ and (311) orientations and the ones grown from D-malate had $(1\,\bar{1}\,\bar{1})$ and $(\bar{3}\,\bar{1}\,\bar{1})$ orientations. CuO films grown on Cu(110) from L-malate had (110) and $(31\,\bar{1})$ orientations while the one grown from a D-malate deposition bath had $(\bar{1}\,\bar{1}\,0)$ and $(\bar{3}\,\bar{1}\,1)$ orientations. The films grown from racemic malate bath showed $(\bar{1}\,1\,1)$ and $(1\,\bar{1}\,\bar{1})$ orientations on Cu(111) and (110) and $(\bar{1}\,\bar{1}\,0)$ orientations on Cu(110).

X-ray crystal structures of Cu(II) complexed with malic acid were grown. The crystals were grown at pH= 1.5 which is different from the solution used for the electrodeposition. In our case it is reasonable to expect malic acid or copper-malate complexes to adsorb on Cu(111) and Cu(110) surface and break the symmetry. Complexes of Cu(II)-malate were found to have polymeric structure with a symmetry that is determined by the handedness of the malate ligand. Another cause of the asymmetry could be the surface reconstruction of the underlying Cu substrate.

Acknowledgements

This work was supported by National Science Foundation grant DMR-0504715.

Notes

[a] *Department of Chemistry, and Graduate Centre for Materials Research, Missouri University of Science & Technology, Rolla, MO, 65409, USA. Fax: +1-573-341-2071; Tel: +1-573-341-6943; +1-573-202-4538; E-mail: rghy7@mail.mst.edu*

[b] *Department of Chemistry, Western Michigan University, Kalamazoo, MI, 49008, USA. Fax: +1-269-387-2909; Tel: +1-269-387-2832;*

†Electronic Supplementary Information (ESI) available: crystal data structure and refinement, atomic coordinates, isotropic displacement parameters, bond lengths, angles, anisotropic displacement parameters, and torision angle, for Cu^{2+} L-malate dehydrate, Cu^{2+} D-malate dehydrate, and Cu^{2+} DL-malate dehydrate. See DOI: 10.1039/b000000x/

REFERENCES

1. R. Noyori, Asymmetric Catalysis in Organic Synthesis, Wiley, New York, 1994.

2. J. M. Brown, A.J. Davies, *Nature*, 1994, **370**, 418.

3. C. F. McFadden, P. S. Cremer, A. J. Gellman, *Langmuir*, 1996, **12**, 2483.

4. G. A. Attard, *J. Phys. Chem. B*, 2001, **105**, 3158.

5. D. S. Scholl, *Langmuir*, 1998, **14**, 862.

6. G. A. Attard, *J. Phys. Chem. B*, 2001, **105**, 3158.

7. M. O. Lorenzo, C. J. Baddeley, C. Muryn, R. Raval, *Nature,* 2000, **404**, 376.

8. D. S. Scholl, A. Asthagiri, T. D. Power, *J. Phys. Chem. B*, 2001, **105**, 4771.

9. V. Humblot, S. Haq, C. Muryn, W. A. Hofer, R. Raval, *J. Am. Chem. Soc.*, 2002, 124, 503.

10. A. Kűhnle, T. R. Linderoth, B. Hammer, F. Besenbacher, *Nature*, 2002, **415**, 891.

11. R. Fasel, M. Parschau, K. H. Ernst, *Nature*, 2006, **439**, 449.

12. C. LeBlond, J. Wang, J. Liu, A. T. Andrews, Y. K. Sun, *J. Am. Chem. Soc.,* 1999, **121**, 4920.

13. S. Åsbrink, L. -J. Norrby, *Acta Crystallogr.*, 1970, **B26**, 8.

14. J. I. Langford, D. Louër, *J. Appl. Crystallogr.*, 1991, **24**, 149.

15. N. E. Brese, M. O'Keefe, B. L. Ramakrishna, R. B. Von Dreele, *J. Solid state Chem.,* 1990, **89**, 184.

16. I. G. Casella, M. Gatta, *J. Electroanal. Chem.*, 2000, **12**, 494.

17. K. Ogura, K. Nakaoka, M. Nakayama, S. Tanaka, *J. Electroanal. Chem.*, 2001, **122**, 511.

18. P. Poizot, C. -J. Hung, M. P. Nikiforov, E. W. Bohannan, J. A. Switzer, *Electrochem. Solid State Lett.*, 2003, **6**, C21.

19. S. C. Ray, *Sol. Energy Mater. Sol. Cells*, 2001, **307**, 68.

20. A. Catana, J. -P. Locquet, S. M. Paik, I. K. Schuller, *Phys. Rev. B*, 1992, **46**, 15477.

21. I. M. Watson, M. P. Atwood, T. J. Cumberbatch, *Thin Solid Films*, 1994, **251**, 51.

22. J. L.G. Vizkelethy, P. Revesz, J. W. Mayer, K. N. Tu, *J. Appl. Phys.*, 1991, **1020**, 69.

23. A. M. S. E. Din, R. M. A. E. Wahab, *Electrochim. Acta*, 1964, **113**, 9.

24. J. A. Switzer, H. M. Kothari, P. Poizot, S. Nakanishi, E. W. Bohannan, *Nature,* 2003, **425**, 490.

25. H. M. Kothari, E. A. Kulp, S. Boonsalee, M. P. Nikiforov, E. W. Bohannan, Poizot, P.; Nakanishi, S.; Switzer, J.A. *Chem. Mater.,* 2004, **16**, 4232.

26. E. W. Bohannan, H. M. Kothari, I. M. Nicic, J. A. Switzer, *J. Am. Chem. Soc.*, 2004, **126**, 488.

27. E. W Bohannan, I. M. Nicic, H. M. Kothari, J. A. Switzer, *Electrochimica Acta*, 2007, **53**, 155-160

28. R. Widmer, F. -J. Haung, P. Ruffieux, O. Gröning, M. Bielmann, P. Gröning, R. Fasel, *J. Am. Chem Soc.*, 2006, **128**, 14103.

29. S. K. Sarkar, N. Burla, E. W. Bohannan, J. A. Switzer, *J. Am. Chem. Soc.*, 2007, **129**, 8972.

30. T. M. Polyanskaya, V. V. Bakakin, I. I. Zviedre, *Zh. Strukt. Khim.*, 1982, **23**, 117.

31. R. J. Missavage, R. L. Belford, I. C. Paul, *J. Coord. Chem.*, 1972, **2**, 145.

32. L. Kryger, S. E. Rasmussen, *Acta Chem. Scand.*, 1972, **26**, 2349.

33. A. Karipides, A. T. Reed, *Inorg. Chem.*, 1976, **15**, 44.

34. Bruker, SMART and SAINT. Bruker AXS Inc.: 2002, Madison, Wisconsin, USA

35. G. M. Sheldrick, SADABS Program for the Empirical Absorption Correction of Area Detector; 1996, University of Gottingen: Germany.

36. G. M. Sheldrick, SHELXTL V5.0 Software Reference Manual; Bruker AXS Inc.: 2002, Madison, Wisconsin, USA.

37. J. A. Switzer, *Electrochem. Soc. Interface.*, 2004, **13**, 34.

38. J. D. Hovrath, A. Gellman, *J. Top. Catal.*, 2003, **25**, 9.

39. X. Zhao, *J. Am. Chem. Soc.*, 2000, **122**, 12584.

40. M. Schunack, E. Laegsgaard, I. Stensgaard, I. Johannsen, F. Besenbacher, *Angew. Chem., Int. Ed.*, 2001, **40**, 2623.

41. R. Nazimutdinov, J. Zhang, T. Zinkicheva, I. Manyurov, J. Ulstrup, *Langmuir*, 2006, **22**, 7556-7567.

42. A. Calzolari, A. Ruini, E. Molinari, M. J. Caldas, *Phys. Rev. B*, 2006, **73**, 125420.

Table 1. List of planes having identical d spacing for monoclinic CuO

2θ (degrees)	**d-spacing (nm)**	**planes**
35.570	0.252546	$(1\bar{1}\bar{1})$, $(\bar{1}11)$, $(11\bar{1})$, $(\bar{1}\bar{1}1)$
38.742	0.23223	(111), $(\bar{1}\bar{1}\bar{1})$, $(1\bar{1}1)$, $(\bar{1}1\bar{1})$
73.342	0.13046	(311), $(3\bar{1}1)$, $(\bar{3}\bar{1}\bar{1})$, $(\bar{3}1\bar{1})$

Table 2. Crystal data for L-, D- and DL- bis(malato)copper(II) dehydrate

Complexes / Parameters	Copper(II) L-malate	Copper(II) D-malate	Copper(II) DL-malate
Empirical Formula	$C_8H_{14}O_{12}Cu$	$C_8H_{14}O_{12}Cu$	$C_8H_{14}O_{12}Cu$
Cell weight	365.73	365.73	365.73
Symmetry, Space Group	Monoclinic, $P2_1$ (#4)	Monoclinic, $P2_1$ (#4)	Monoclinic, $P2_1/c$(#14)
Unit Cell Dimensions	a = 7.587(14)Å b =10.222(19)Å c = 8.169(15)Å β = 92.796(3)°	a = 7.584(2)Å b =10.219 (3) Å c = 8.173(2)Å β = 92.786(5)°	a = 8.474(19)Å b = 7.424(17)Å c = 10.291(2)Å β = 102.586(4)°
Cell Volume	632.7(2) $Å^3$	632.6(3) $Å^3$	631.8(3) $Å^3$
Z	2	2	2
Density, g/cm^3 (calculated)	1.920	1.920	1.922
Absorption Coefficient, mm^{-1}	1.792	1.793	1.795
F(000)	374.0	374.0	374.0
Crystal dimensions(mm)	0.40x0.20x0.20	0.40x0.30x0.35	0.7x0.50x0.5
Θ (min-max)	2.69 - 28.42 °	2.69 - 28.45 °	3.41 - 28.37 °
Index Range	$-9 \le h \le 10$; $-13 \le k \le 13$; $-10 \le l \le 10$;	$-10 \le h \le 10$; $-13 \le k \le 13$; $-10 \le l \le 10$;	$-11 \le h \le 11$; $-9 \le k \le 9$; $-13 \le l \le 13$;
Reflections collected	6550	3900	6162
No. of independent reflections, R(int)%	3108 $R_{(int)} = 1.94$	2083 $R_{(int)} = 2.72$	1561 $R_{(int)} = 2.25$
Absorption correction method	SADABS	SADABS	SADABS
Goodness-of-fit on F^2	1.057	1.008	1.150
Final R indices, % [$I \ge 2\sigma(I)$]	$R_1 = 2.26$; $wR_2 = 5.83$	$R_1 = 2.70$; $wR_2 = 6.39$	$R_1 = 2.88$; $wR_2 = 7.69$
R indices, % (all data)	$R_1 = 2.30$; $wR_2 = 5.86$	$R_1 = 2.73$; $wR_2 = 6.41$	$R_1 = 3.09$; $wR_2 = 8.04$
Occupancy sum of asymmetric unit	21 Non-H atoms, 14 H atoms	21 Non-H atoms, 14 H atoms	21 Non-H atoms, 14 H atoms

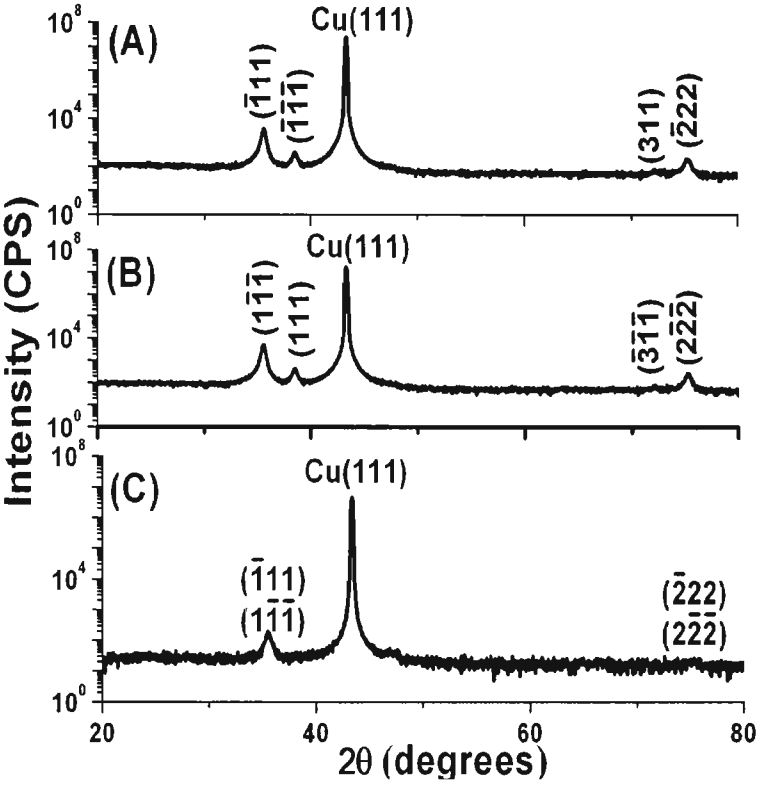

Fig. 1 X-ray diffraction θ-2θ scan for a CuO film on Cu (111) from a solution of (A) L-malate (B) D-malate and (C) DL-malate

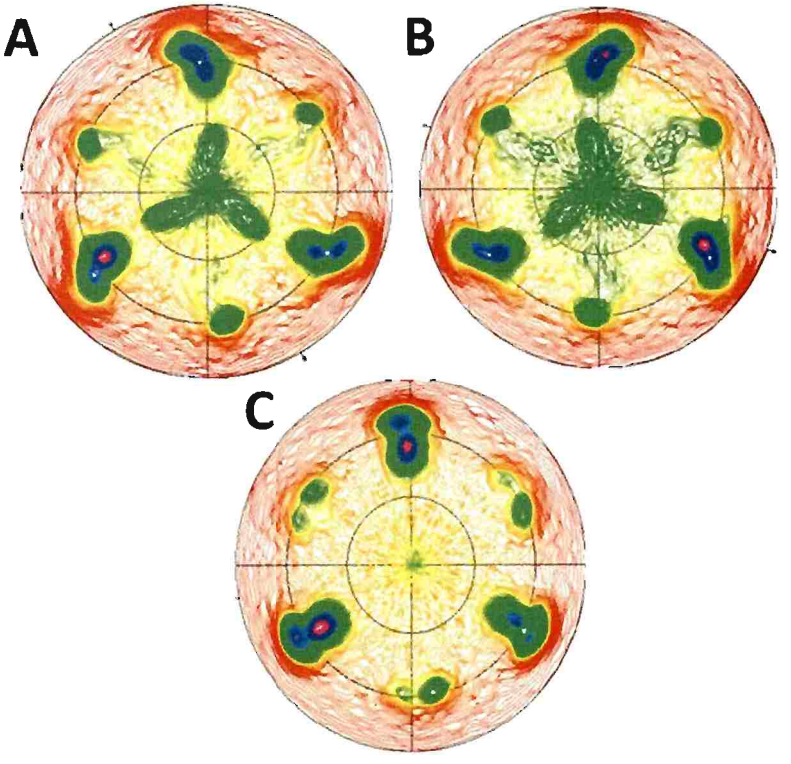

Fig. 2 CuO (111) pole figures for films of CuO on Cu (111) grown from solutions of (A) L-malate and (B) D-malate and (C) DL-malate. The films are grown at a constant potential of +350mV vs. SCE at 30°C for 900s.

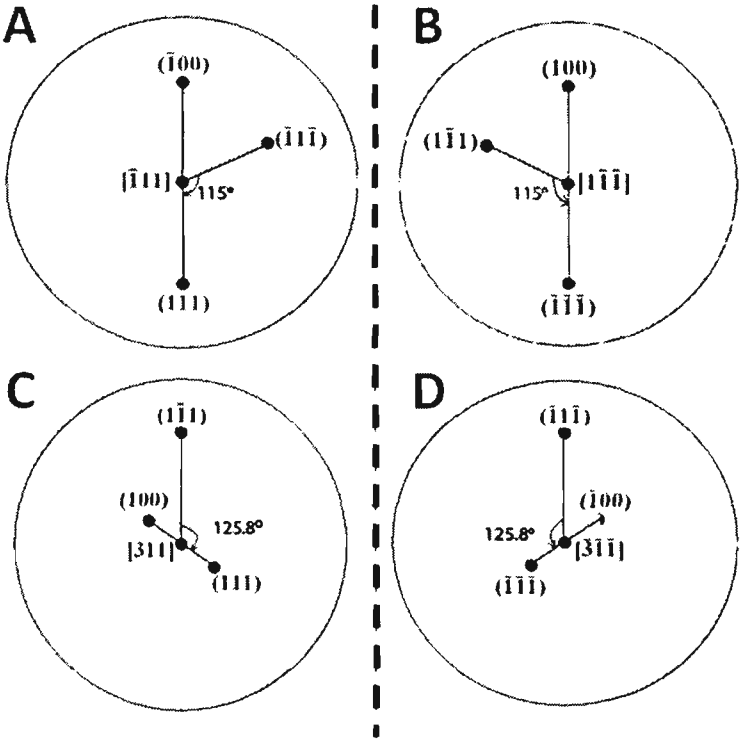

Fig. 3 Stereographic projections for (A) $(\bar{1}\,1\,1)$, (B) $(1\,\bar{1}\,\bar{1})$, (C) $(3\,1\,1)$ and (D) $(\bar{3}\,\bar{1}\,\bar{1})$ orientations indicating the positions where the (111) type and (100) type reflections should be observed in the pole figures. For the $(\bar{1}\,1\,1)$ orientation, reflections from the $(\bar{1}\,1\,\bar{1})$ plane at $\chi = 57^{\circ}$ and the $(1\,1\,1)$ plane at $\chi = 63^{\circ}$ are separated azimuthally by 115° rotated clockwise. For the $(3\,1\,1)$ orientation the $(1\,\bar{1}\,1)$ plane is at $\chi = 68.14^{\circ}$, the $(1\,1\,1)$ planes at $\chi = 27.41^{\circ}$ and (100) planes at $\chi = 27.19^{\circ}$. For the $(1\,\bar{1}\,\bar{1})$ orientation the $(1\,\bar{1}\,1)$ plane is at $\chi = 57^{\circ}$ and the $(\bar{1}\,\bar{1}\,\bar{1})$ plane is at $\chi = 63^{\circ}$ are separated azimuthally by 115° rotated counterclockwise. For the $(\bar{3}\,\bar{1}\,\bar{1})$ orientation the $(\bar{1}\,1\,\bar{1})$ plane at $\chi = 68.14^{\circ}$, the $(\bar{1}\,\bar{1}\,\bar{1})$ plane at $\chi = 27.41^{\circ}$ are separated azimuthally by 125.8°.

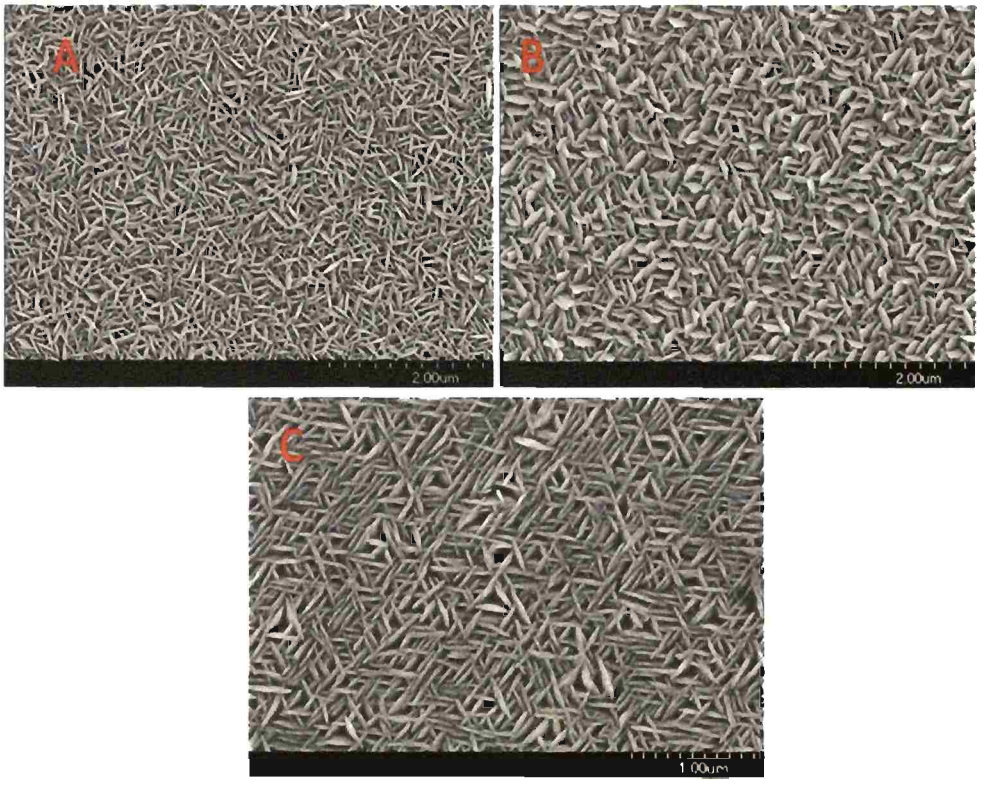

Fig. 4 SEM images of CuO films on Cu(111) grown from solutions of (A) L-malate, (B) D-malate and (C) DL-malate.

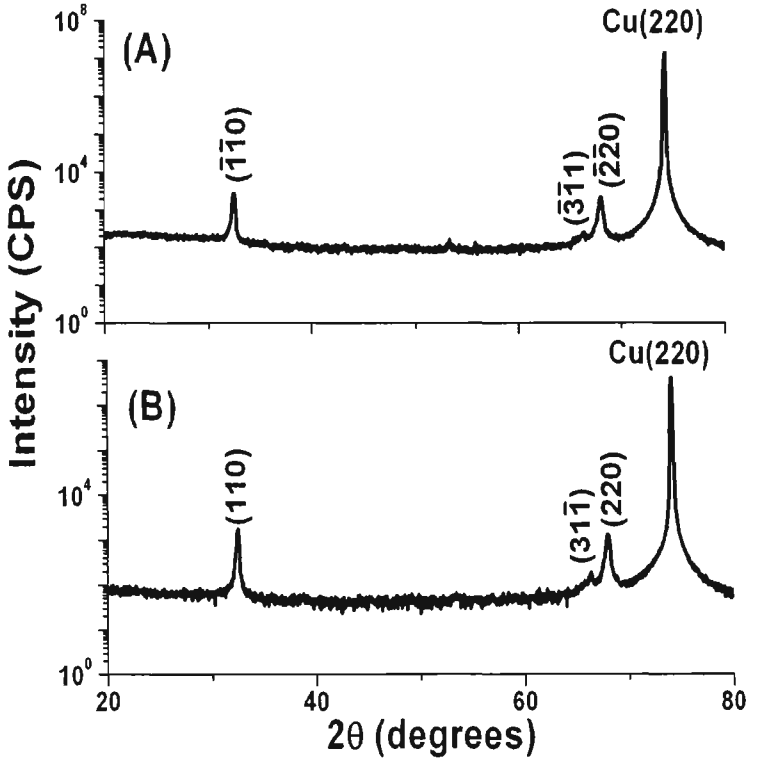

Fig. 5 θ-2θ scans for films of CuO on Cu(110) from solutions of (A) L-malate and (B) D-malate. Intense peaks are seen at 2θ = 32.4° and 67.9° corresponding to CuO$(\bar{1}\,\bar{1}\,0)$, CuO(110), and CuO$(\bar{2}\bar{2}0)$, CuO(220) respectively. A small peak at 2θ = 66.28° is also observed which corresponds to CuO$(\bar{3}\,\bar{1}\,1)$, and CuO$(31\,\bar{1})$.

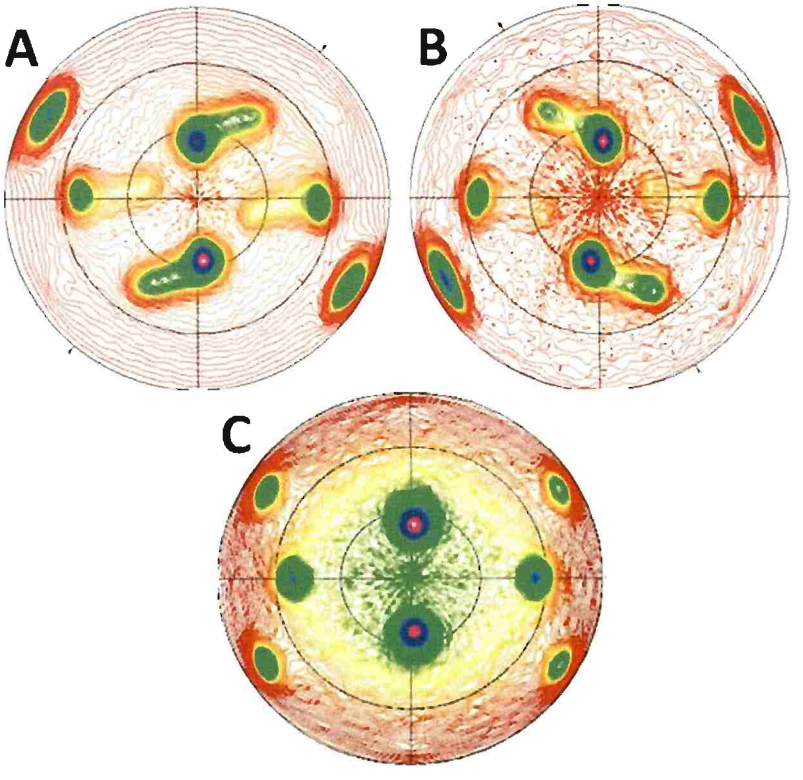

Fig. 6 CuO(111) Pole figures of films deposited on Cu(110) single crystal from solutions of (A) L-malate, (B) D-malate and (C) DL-malate at constant potential of 350 mV for 1800 sec at 30 °C.

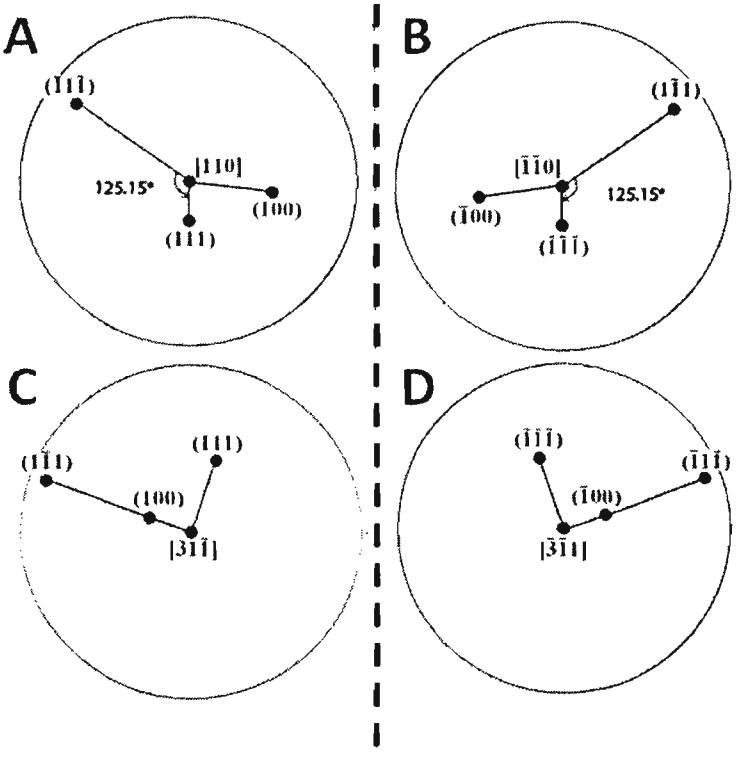

Fig. 7 Stereographic projections for (A) (110) (B) $(\bar{1}\,\bar{1}\,0)$ (C) $(3\,1\,\bar{1})$ and (D) $(\bar{3}\,\bar{1}\,1)$ orientations indicating the positions where the (111) type and (100) type reflections should be observed in the pole figures. For the (110) orientation, reflections from the $(\bar{1}\,1\,\bar{1})$ plane at $\chi = 78.54^{\circ}$ and the (111) plane at $\chi = 27.16^{\circ}$ are separated azimuthally by 125.15° rotated counterclockwise. For the $(\bar{1}\,\bar{1}\,0)$ orientation the $(1\,\bar{1}\,1)$ plane is at $\chi = 78.54^{\circ}$ and the $(\bar{1}\,\bar{1}\,\bar{1})$ plane is at $\chi = 27.16^{\circ}$ are separated azimuthally by 125.14° rotated clockwise. For the $(3\,1\,\bar{1})$ orientation, reflections from the $(1\,\bar{1}\,1)$ plane at χ=84.19° and the (111) plane is at $\chi = 48.84^{\circ}$ are separated azimuthally by 85.37°. Similarly in $(\bar{3}\,\bar{1}\,1)$ orientation the planes $(\bar{1}\,1\,\bar{1})$ and $(\bar{1}\,\bar{1}\,\bar{1})$ are separated azimuthally by 85.37°.

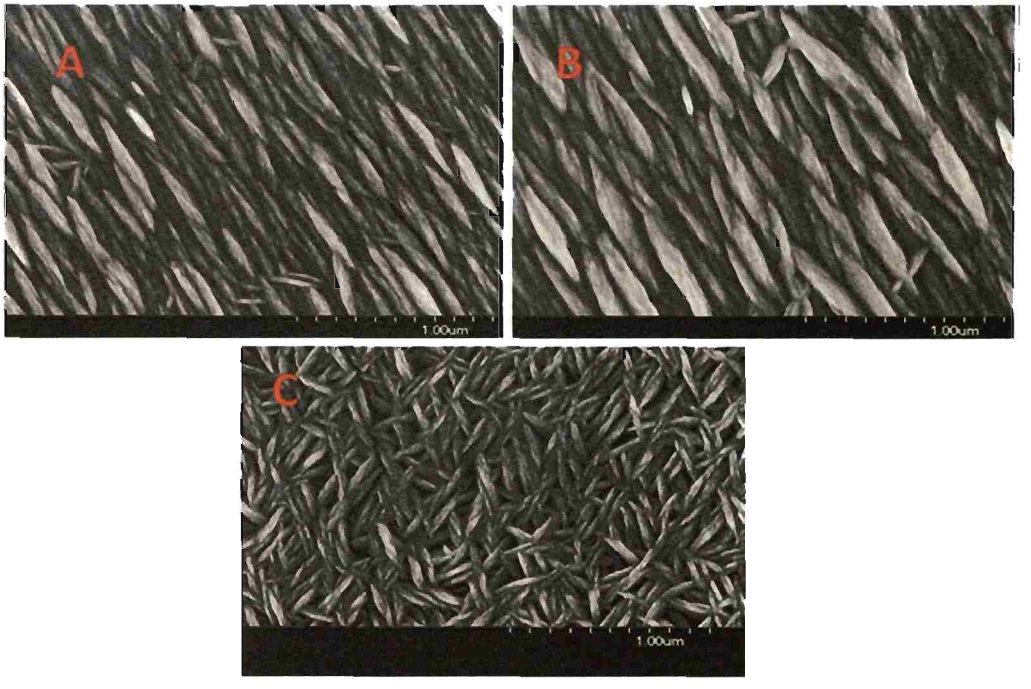

Fig. 8 SEM images of CuO films on Cu(110) grown from solutions of (A) L-malate, (B) D-malate and (C) DL-malate.

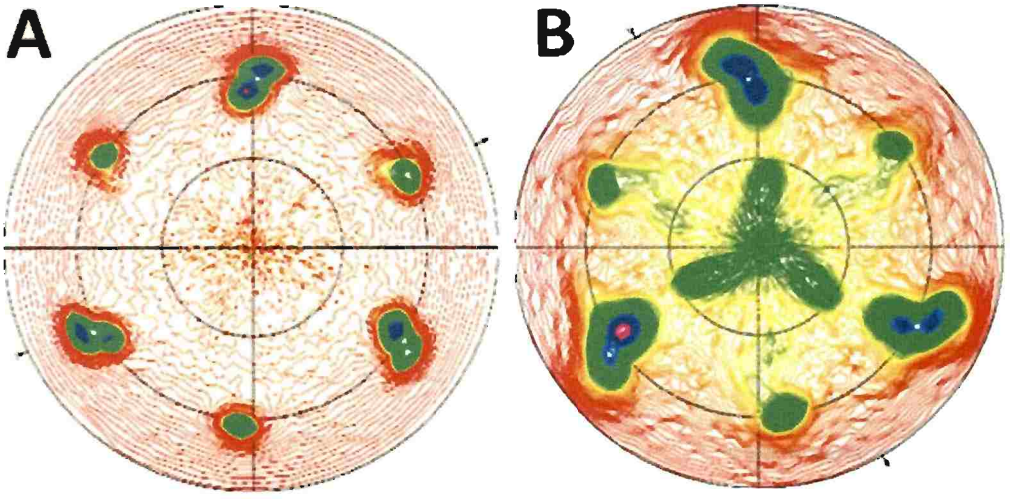

Fig. 9 CuO(111) pole figure of a film deposited on Cu(111) single crystal from (A) L (+)-tartaric acid and (B) L(-) – malic acid.

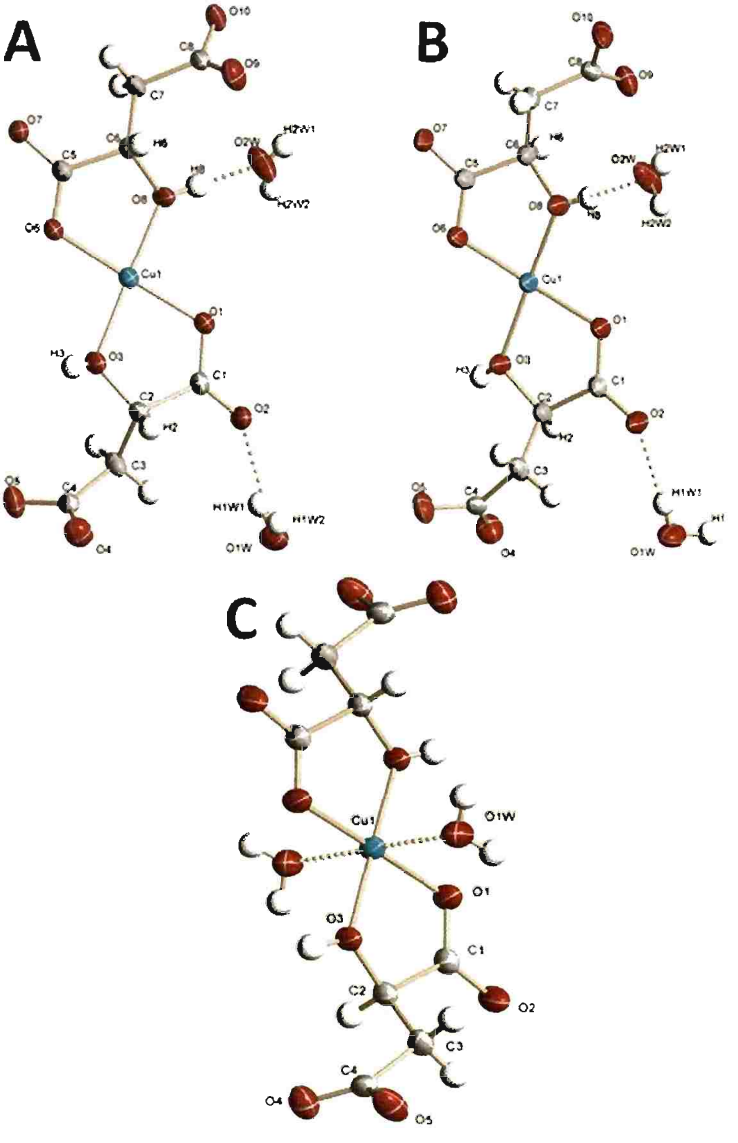

Fig. 10 Monomeric fragments of the structures of (A) bis(L-malate) Cu(II) dihydrate complex, (B) bis(D-malate)Cu(II) dihydrate complex, , and the molecular structure (C) bis(DL-malate) Cu(II) dihydrate complexes. The ellipsoids show the thermal motion of the atoms with a probability of 50%. The positions of the hydrogen atoms (H2 and H6) relative to their carbon atoms (C2 and C6) determines the chirality of these complexes.

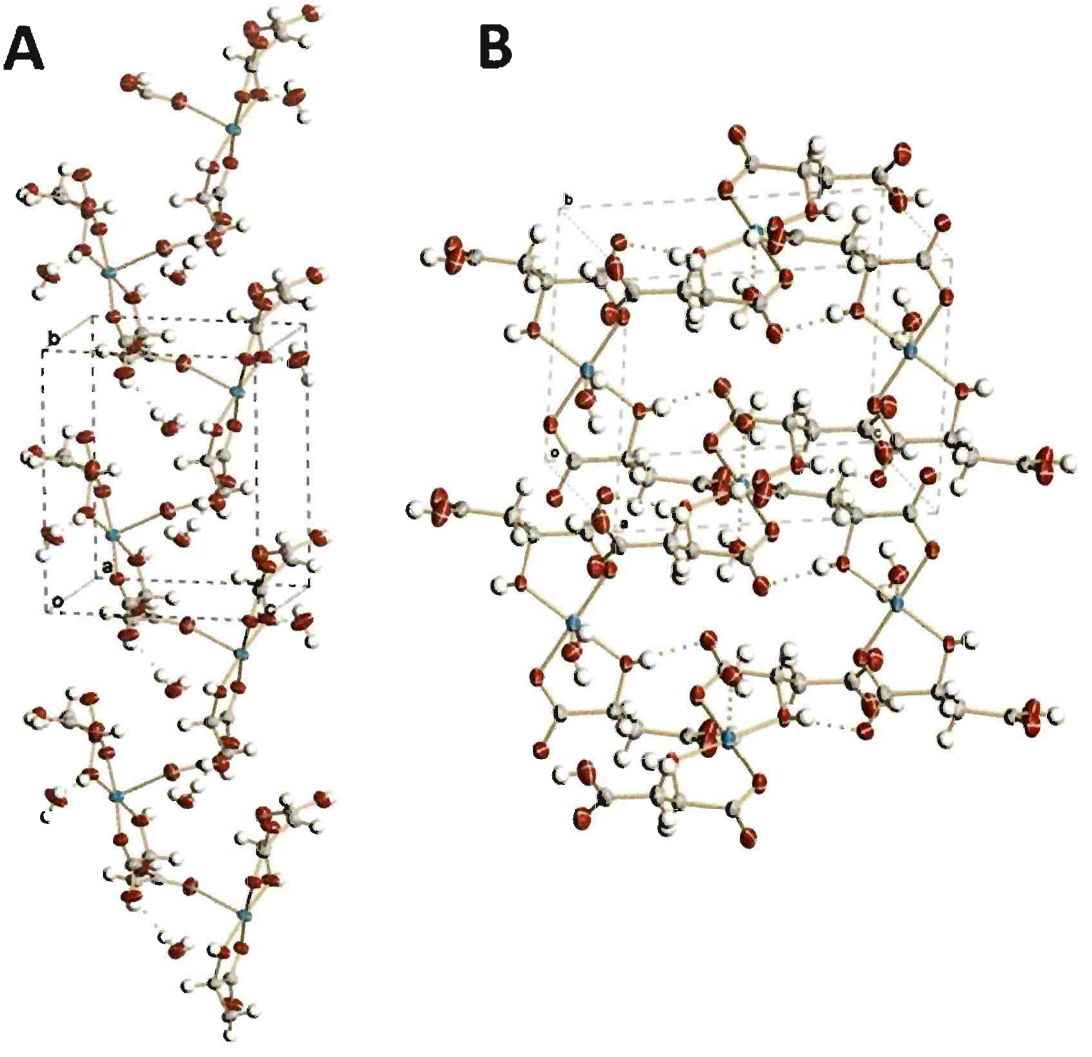

Fig. 11 Packing diagrams showing the polymerization of (A) L- and (B) racemic bis(malato) Cu(II) dihydrate complexes. Both L- and D- chiral complexes polymerize in a similar fashion.

APPENDIX A.

SUPPORTING INFORMATION FOR PAPER I

Jay A. Switzer,* Rakesh V. Gudavarthy, Elizabeth A. Kulp, Guojun Mu, Zhen He, and Andrew J. Wessel

*To whom correspondence should be addressed. E-mail: jswitzer@mst.edu

Materials and Methods

A. Deposition Solutions

The deposition bath for the magnetite films and superlattices contained 87 mM Fe(III), 100 mM TEA, and 2 M NaOH. The solution was prepared by dissolving 2.6 grams of iron(III) sulfate pentahydrate in 15 ml of 1 M triethanolamine (TEA), resulting in a deep red-colored solution. It was diluted with 50 ml of deionized water. The diluted solution was then added to a second solution that was produced by adding 12.0 g of NaOH pellets to 85 ml of deionized water. The resulting 150 mL of gray-green solution was heated to 80 °C and stirred at a rate of 200 rpm.

The deposition bath for zinc ferrite films and superlattices contained 87 mM Fe(III), 30 mL Zn(II), 100 mM TEA, and 2 M NaOH. It was prepared by the procedure described above, and adding 1.34 grams of zinc nitrate hexahydrate before heating the solution to 80 °C. All chemicals were ACS reagent grade and purchased from Sigma-Aldrich. The water was produced in house by a Millipore system (18 MΩ-cm).

B. Electrochemical Methods

The electrodeposition was performed using a Brinkmann PGSTAT 30 Autolab potentiostat controlled with GPES software version 4.9. Epitaxial deposition was performed on a Au(111) single crystal with a geometric area of 0.786 cm^2, wrapped with a Au wire around the perimeter of the crystal for electrical contact. A Pt wire served as the counter electrode, and an Ag/AgCl (KCl sat'd) electrode was the reference electrode. The Au crystals were electropolished with a solution of 100 ml of ethanol, 50 ml of ethylene glycol, and 50 ml of concentrated hydrochloric acid heated to 55 °C. Each gold crystal was positioned in this stirred solution to form a meniscus. An anodic constant current density of 1.6 A/cm^2 was applied for 45 s.

Linear sweep voltammograms were run on an Au polycrystalline rotating disk electrode at 100 rpm in order to determine whether Zn(II) was electroactive in the potential range used to electrodeposit superlattices. As shown in Fig. S1, the Zn(II) to Zn(0) reduction is shifted to negative potentials outside of the deposition positions due to the highly alkaline solution. Linear sweep voltammograms for the magnetite and zinc

ferrite films are nearly identical, because the observed current is due only to the reduction of Fe(III).

The epitaxial magnetite films were deposited onto Au(111) by applying constant potentials of -1.01, -1.02, -1.03, -1.04, -1.05, -1.06, -1.07, and -1.08 V. The total charge passed through the electrode was controlled to be 1 C/cm^2 to obtain a film that was 2 μm thick. The magnetite superlattices were deposited by pulsing potentials between -1.01 and -1.065 V (see Fig. S2). By changing the dwell time at each potential, superlattices with different modulation wavelengths were deposited. The epitaxial zinc ferrite films were deposited by applying constant potentials of -0.97, -0.99, -1.01, -1.03, -1.05, and -1.07 V. The zinc ferrite superlattices were deposited by pulsing potentials between -0.99 and -1.05 V (see Fig. S2). The dwell times and potentials used to deposit superlattices with different modulation wavelengths are shown in Table S1.

C. Electron microscopy and X-ray diffraction

A dual FEI Helios NanoLab 600 FIB/FESEM was used to image the cross-section of a superlattice in the magnetite/zinc ferrite system that had a modulation wavelength of 70 nm. The duality of this instrument allows for site-specific FIB cross-sectioning and high resolution SEM imaging. For this work, the FIB was used to prepare a TEM lift-out. Prior to milling, a platinum layer was deposited to protect an area of the superlattice from the ion bombardment of the gallium source for the FIB milling. Two trenches were milled on either side of the protective Pt layer. The lift-out site was then mounted to the omniprobe. An undercut was milled to release the sample from the bulk. The freed sample was then lifted from the bulk and attached with Pt to a special TEM grid. The attached sample was milled to a thickness of 100 nm. This FIB prepared lift-out was then imaged with the high angle annular dark field (HAADF) STEM detector to improve the visualization of the layered structure of the superlattice (maximizing the Z contrast).

X-ray analysis of magnetite and zinc ferrite superlattices was performed using a high-resolution Philips X-Pert MRD x-ray diffractometer with a Cu $K_{\alpha 1}$ radiation source (λ = 0.154056 nm). The symmetric x-ray diffraction patterns were obtained using the line focus mode. The primary optics consisted of a combination Göbel mirror and a two crystal Ge(220) two-bounce hybrid monochromator (PW3147/00) producing pure $CuK\alpha_1$

radiation on the incident beam side. A 0.18° parallel plate collimator (PW3098/18) was used as the secondary (diffracted beam) optics. Scans were run from 2θ values of 76° to 81° to obtain improved statistics around the satellite positions for the superlattice. The lattice parameter of each film was determined by Rietveld analysis using RIQAS software from Materials Data Inc.

The in-plane orientation of the zinc ferrite superlattice relative to the Au single crystal was determined by x-ray pole figures and azimuthal scans. For these measurements, the diffractometer was operated in the point focus mode with a crossed slit collimator module (PW3084/62) as the primary optics. A 0.27° parallel plate collimator (PW3098/27) equipped with a flat graphite monochromator (PW3121/00) was used as the secondary optics. To perform the pole figure analysis, the 2θ angle of the diffractometer was set to the angle of the Fe_3O_4(311) plane (2θ = 35.426°) and to that of the Au(311) plane (2θ = 77.547°) for the substrate. The sample was moved through a sequence of tilt angles, χ, from 0° to 90°, and at each χ, the sample was rotated azimuthally, ϕ, from 0° to 360°. Data were collected in the continuous mode over 3° intervals for both χ and ϕ, with a count time of 5 seconds per point.

D. Measurement of Electrical Properties

The Verwey transition temperatures of the films and superlattices were measured by determining the temperature dependence of resistance of Fe_3O_4 on Au(111) with the Quantum Design Physical Property Measurement System (PPMS, San Diego, CA) (see Fig. S3). One silver wire was attached to the film surface by using indium metal, the other connected to the gold (see Fig. S4). The contact area of indium was approximately 1 mm^2, and the diameter of the silver wire was 0.1 mm.

Current-voltage curves of Fe_3O_4 on Au(111) were measured at 77 K (in liquid N_2) using an EG&G Princeton Applied Research PARSTAT 2273 potentiostat/galvanostat controlled with Powersuit software version 2.58. One silver wire was attached to the film surface with indium metal, the other connected to the gold (see Fig. S4). The working electrode and sensor leads from the potentiostat were connected to the film surface. The reference and counter electrode leads from the potentiostat were connected to the gold substrate. Both current and voltage scans were performed (see Figs. S5 and S6). The

current was scanned at 50 mA/s, and the voltage was scanned at 100 mV/s. Both types of scans were plotted as current *vs.* bias. The instrumental limits for the PARSTAT 2273 potentiostat/galvanostat are ±2 A and ±10V.

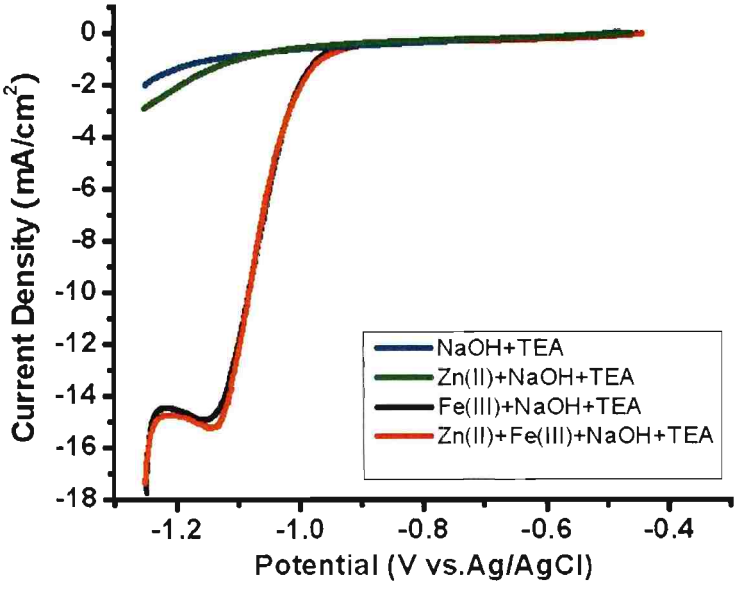

Fig. S.1. Linear sweep voltammograms at 80 °C on an Au rotating disk electrode in the magnetite deposition solution (black), zinc ferrite deposition solution (red), alkaline Zn(II) solution containing TEA (green), and alkaline TEA solution (blue). The concentrations are [Fe(III)] = 87 mM, [Zn(II)] = 30 mM, [NaOH] = 2 M, and [TEA] = 100 mM. The voltammograms show that Zn(II) is electrochemically inactive at the potentials used to deposit the superlattices.

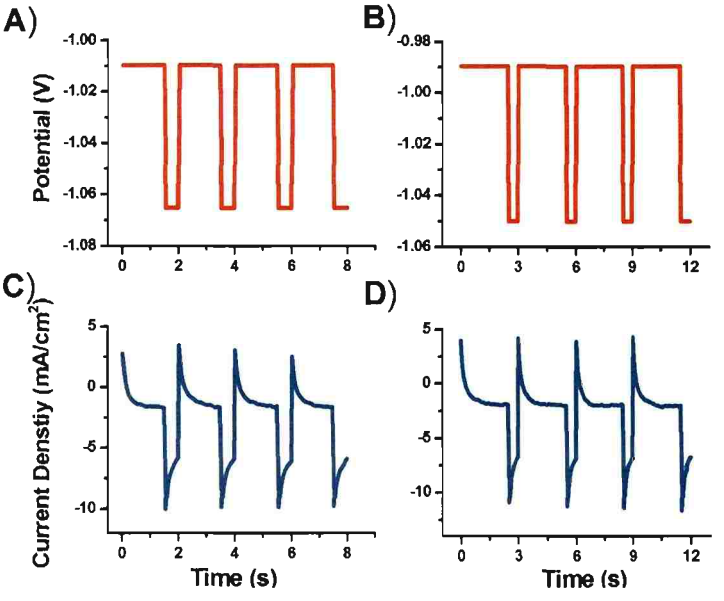

Fig. S.2. Comparison of the applied voltage/time waveforms (A, B) to the measured current-time transients (C, D) for the electrodeposition of superlattices on a Au(111) substrate. The magnetite superlattice (A, C) was deposited from the solution of 87 mM Fe(III), 100 mM TEA, and 2 M NaOH at 80 °C by pulsing the applied potential between -1.01 V for 1.5 sec, and -1.065 V for 0.5 sec. The zinc ferrite superlattice (B, D) was deposited from the solution of 87 mM Fe(III), 30 mM Zn(II), 100 mM TEA, and 2 M NaOH at 80 °C by pulsing the applied potential between -0.99 V for 2.5 sec, and -1.05 V for 2.5 sec.

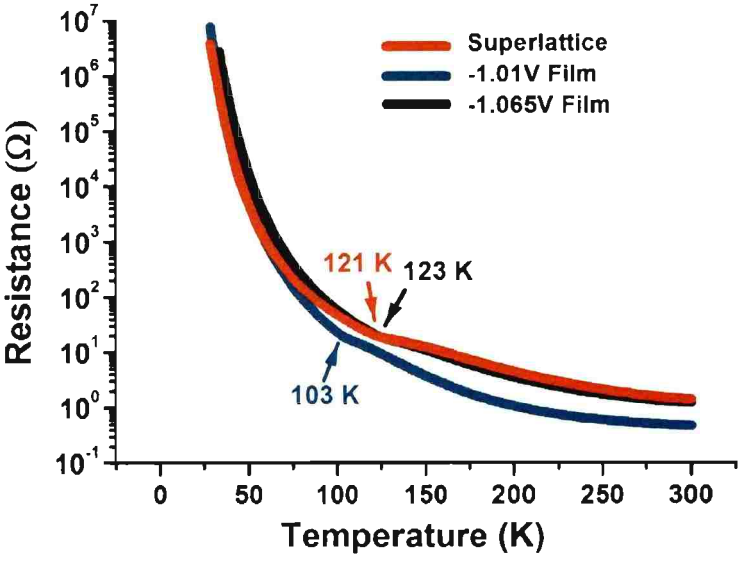

Fig. S.3. Determination of the Verwey transition temperature for magnetite films and a magnetite superlattice from a plot of log(resistance) versus temperature. The magnetite films were deposited at potentials of -1.01V and -1.065V *vs.* Ag/AgCl (sat'd KCl). The magnetite superlattice was deposited by pulsing -1.01 V for 1.5 sec, and -1.065 V for 0.5 sec. It had a modulation wavelength of 12.2 nm and a total of 354 bilayers.

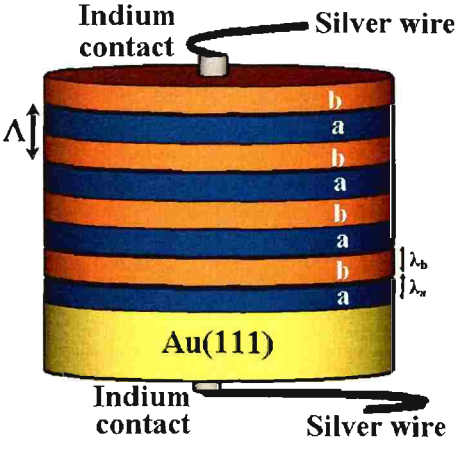

Fig. S.4. Schematic of the configuration for perpendicular transport measurements for magnetite films and superlattices. One silver wire was attached to the film surface using an indium metal pressed contact, and the other was attached to the Au(111). The contact area is approximately 1 mm^2. The diameter of the silver wire is 0.1 mm. The surface area of Au(111) is 0.786 cm^2, and the thickness of the Au(111) is 2 mm.

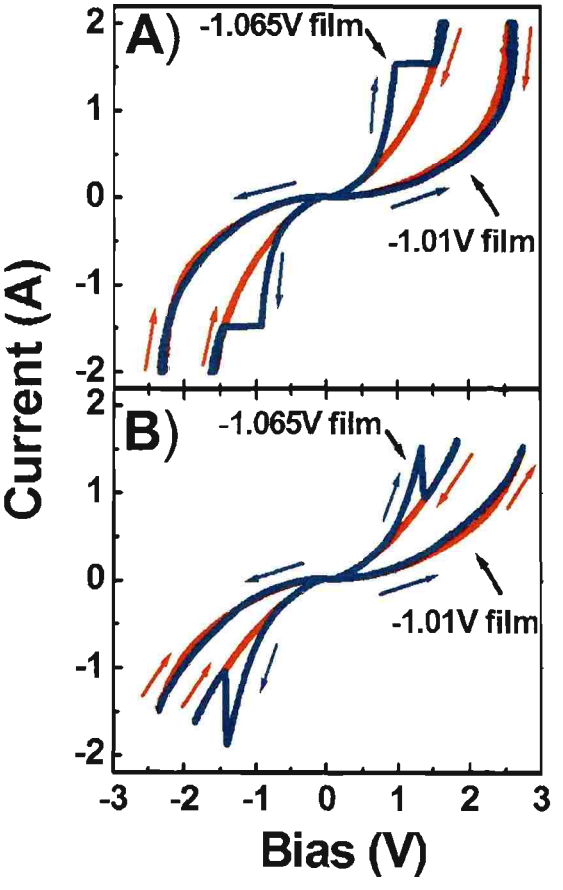

Fig. S.5. Resistance switching of magnetite films on Au(111) at 77 K. The iV curves were run by scanning the current at 50 mA/s **(A)** or by scanning the voltage at 10 mV/s **(B).**

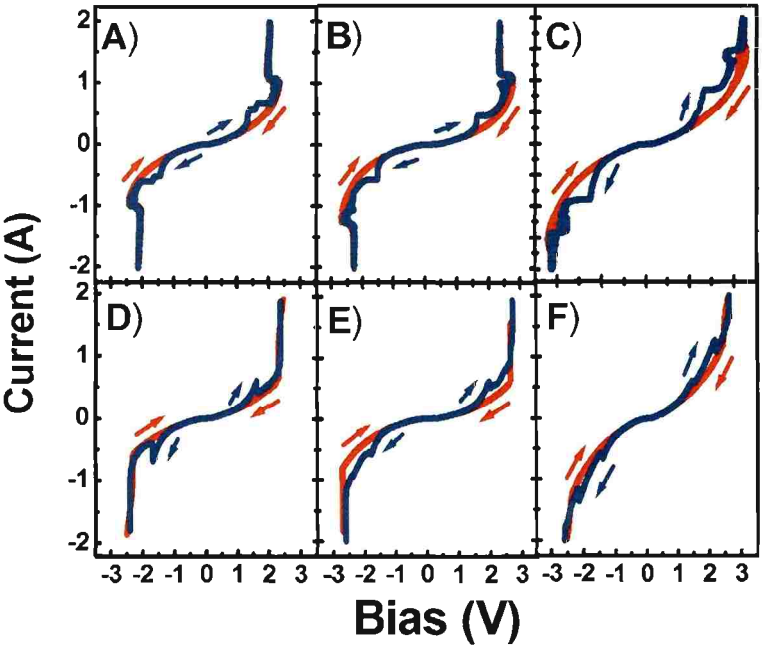

Fig. S.6. Resistance switching of magnetite superlattices with different modulation wavelengths on Au(111) at 77 K. The iV curves were run by scanning the current at 50 mA/s **(A, B, C)** or by scanning the voltage at 10 mV/s **(D, E, F)**. The superlattices measured had modulating wavelengths of 9.4 nm (total of 708 bilayers) **(A, D)**, 12.2 nm (total of 354 bilayers), **(B, E)**, and 20.6 nm (total of 243 bilayers) **(C, F)**.

Table S.1. Dwell times and potentials used for deposition of magnetite defect-chemistry superlattices (left) and compositional superlattices in the zinc ferrite/magnetite system (right) with their corresponding modulation wavelengths (Λ_x).

Dwell Time (sec)		Λ_x **(nm)**
-1.01 V	**-1.065 V**	
0.75	0.25	9.4
1.5	0.5	12.2
3	1	20.6
4	1	25.8

Dwell Time (sec)		Λ_x **(nm)**
-0.99 V	**-1.05 V**	
2.5	0.5	12.5
5	1	16.8
7.5	1.5	29.2

APPENDIX B.

SUPPORTING INFORMATION FOR PAPER II

Rakesh V. Gudavarthy, Andrew S. Miller, Eric W. Bohannan, Elizabeth A. Kulp, Zhen He and Jay A. Switzer*

*To whom correspondence should be addressed. E-mail: jswitzer@mst.edu

A. Linear sweep voltammogram

Linear sweep voltammograms were run on a stainless steel (SS) polycrystalline electrode in the stirred (200 rpm) deposition bath. As shown in Figure **S1 A**, the reduction starts at around -0.99 V and reaches the mass transport limit at -1.2 V vs. Ag/AgCl. If we apply any potential between -1.0 V and -1.1 V vs. Ag/AgCl black films of magnetite are obtained. The polycrystalline magnetite films were deposited onto SS substrates by applying constant potentials of -1.01, -1.02, -1.03, -1.04, -1.05, -1.06, -1.07, and -1.08 V. The total charge passed through the electrode was controlled to be 1 C/cm^2 to obtain a film that was 2 μm thick.

B. X-ray diffraction

X-ray analysis of polycrystalline magnetite films was performed using a high-resolution Philips X-Pert MRD x-ray diffractometer with a Cu $K_{\alpha 1}$ radiation source (λ = 0.154056 nm). The lattice parameter of each film was determined by Rietveld analysis using RIQAS software from Materials Data Inc. The lattice parameter was plotted as a function of applied potential, as shown in Figure **S1 B**. The symmetric x-ray diffraction patterns were obtained using the line focus mode. Figure **S1 C** shows the XRD pattern obtained for a -1.05 V (vs. Ag/AgCl) Fe_3O_4 film deposited on SS substrate. The film has a (200) preferred out-of-plane orientation. X-ray pole figures were obtained in a point focus mode. To perform the pole figure analysis, the 2θ angle of the diffractometer was set to the angle of the Fe_3O_4(311) plane (2θ = 35.426°). Figure **S1 D** shows the Fe_3O_4(311) pole figure for a -1.05 V (vs. Ag/AgCl) Fe_3O_4 film deposited on the SS substrate. The pole figure indicates that the film has (200) fiber texture.

C. Measurement of electrical properties

Current-voltage curves of Fe_3O_4 on SS substrates were measured at 77 K (in liquid N_2) using an EG&G Princeton Applied Research PARSTAT 2273 potentiostat/galvanostat controlled with Powersuit software version 2.58. The working electrode and sensor leads from the potentiostat were connected to the film surface. The reference and counter electrode leads from the potentiostat were connected to the SS substrate. Both current and voltage scans were performed for different studies. Voltage scans were performed to understand the scan rate dependence of the resistance jumps, as

shown in Figures **S2 A** and **B**. Both types of scans were plotted as current *vs.* bias. The instrumental limits for the PARSTAT 2273 potentiostat/galvanostat are ±2 A and ±10V.

To study the retention of the resistance jumps, voltage scans were run between two fixed biases for 100 cycles and the magnitude of the current was recorded, as shown in Figures S2 C and D. Two different films were selected for this study. For the high-to-low resistance jump, a Fe_3O_4 film deposited at -1.03 V vs. Ag/AgCl was selected and for the high-to-low resistance jump, a Fe_3O_4 film deposited at -1.07 V vs. Ag/AgCl was selected. In the case of the low-to-high resistance jump, the bias was pulsed between 0 V and -1.5 V, and for the high-to-low resistance jump, the bias was pulsed between 0 V and – 1.8 V.

To study the effect of the top contact on resistance switching, two different types of contacts were chosen. Indium contacts were made by simply pressing the metal on top of the film. Gold contacts were made by sputtering the Au on top of the film. During the sputtering, only a small area of the film was exposed and rest of the film was masked. Figure **S3** shows the resistance switching curves obtained by sweeping current for both types of contacts.

A commercial magnetite (111) single crystal purchased from Commercial Crystal Laboratories, Inc was 5 x 5 mm in size and contacts were made to the front and back of the crystal by pressing In metal. Resistance switching experiments were performed by sweeping the current from 0 to 0.7 A and measuring the bias, as shown in Figure **S4 A.**

Epitaxial films were deposited on Au(111) single-crystal by applying constant potentials of -1.03 V and -1.07 V vs. Ag/AgCl. Resistance switching experiments were performed by attaching one contact to the film surface with In metal, the other connected to the gold. The iV curves were obtained by sweeping the current from 0 to 2 A and measuring the bias, as shown in Figures **S4 B** and **C**.

The single crystal and epitaxial films do not exhibit the high-to-low resistance jump that is observed in the polycrystalline films. The low-to-high resistance switch is most pronounced in the non-stoichiometric film deposited at -1.03 V vs Ag/AgCl.

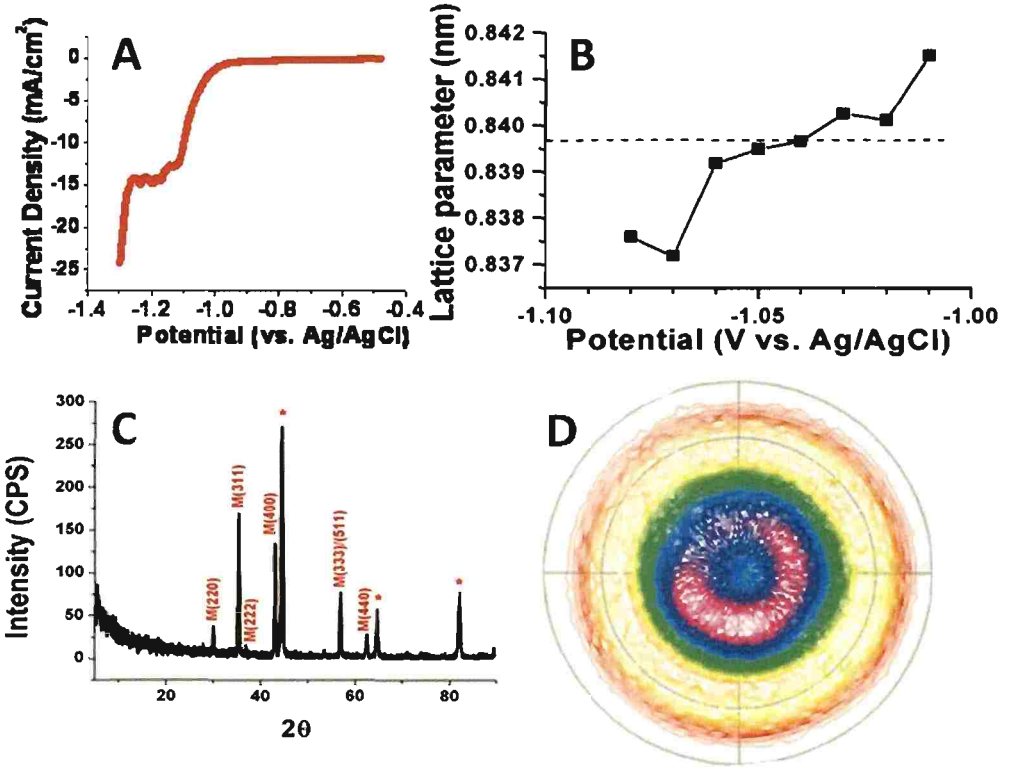

Figure S1.1. (A) Linear sweep voltammogram at 50 mV/s on SS electrode in the Fe(III)-TEA bath used to produce magnetite films. (B) Plot of the lattice parameter of magnetite as a function of potential. The literature value for the lattice parameter of stoichiometeric Fe_3O_4 is shown as black horizontal dashed line. (C) X-ray 2θ scan showing the out of plane orientation of the Fe_3O_4 film produced at -1.05 V on SS substrate. The film has a (200) out of plane orientation. The asterisks (*) used in the pattern represents the substrate peaks and M represents the Fe_3O_4 peaks. (D) (311) pole figure of a Fe_3O_4 film produced at -1.05 V on SS substrate. The pole figure shows that the film has a (200) fiber texture.

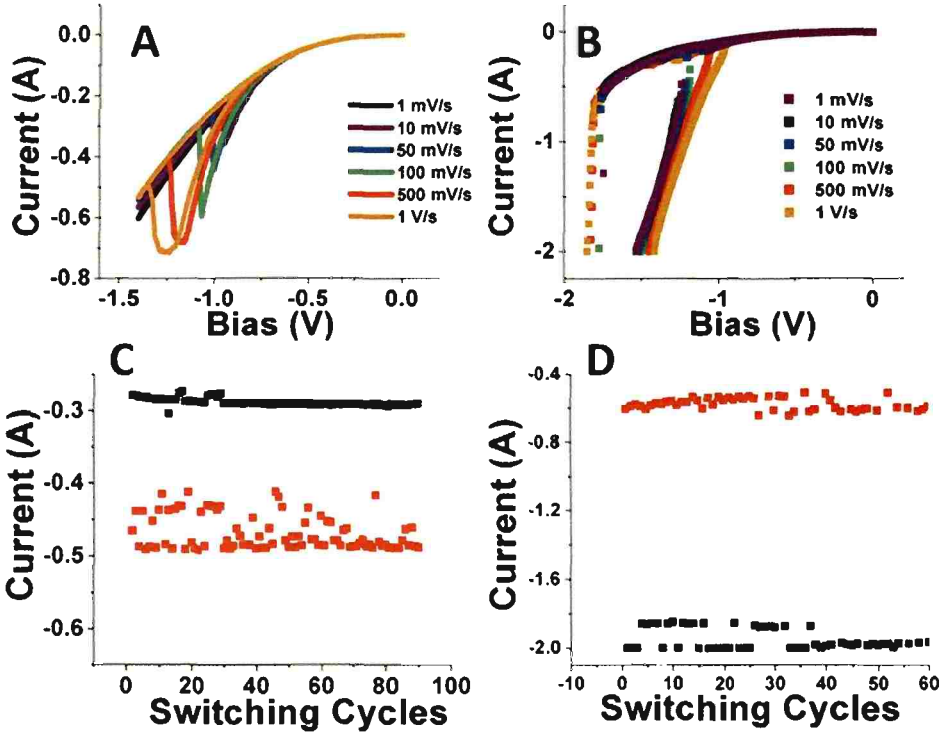

Figure S2.2 Scan rate dependence of the iV curves obtained at 77 K by sweeping the bias and measuring the current for Fe_3O_4 films electrodeposited on SS substrates. (A) iV curve of the low-to-high resistance jump at different scan rates for a Fe_3O_4 film produced at -1.03 V on SS substrate. (B) iV curve of the high-to-low resistance jump at different scan rates for a Fe_3O_4 film produced at -1.07 V on SS substrate. Plot of current as a function of switching cycle (C) for low-to-high resistance jump and (D) for high-to-low resistance jump.

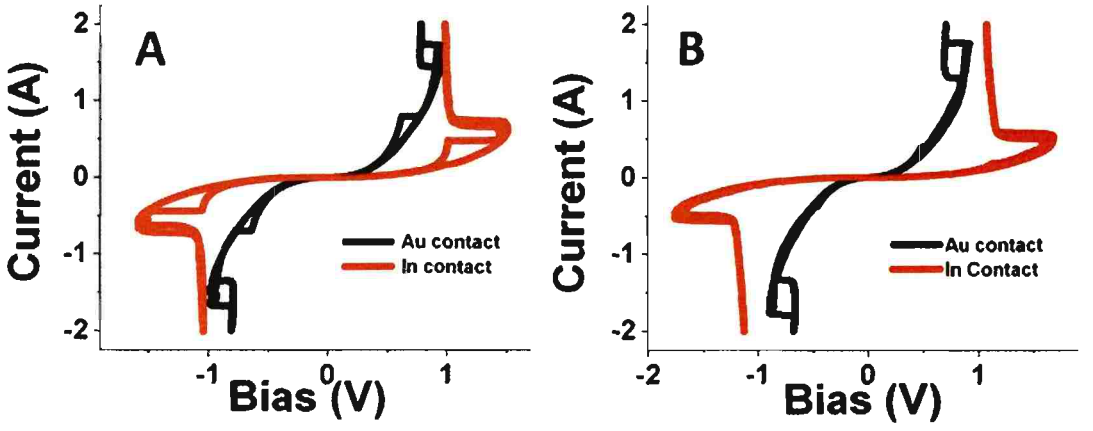

Figure S3.3. Effect of the top contact on resistance switching on Fe_3O_4 films at 77 K obtained by sweeping the current at 50 mA/s and measuring the bias. (A) iV curves of Fe_3O_4 film produced at -1.03 V and (B) iV curves of Fe_3O_4 film produced at -1.07 V. The curve in the black represents iV curve with a Au top contact and the curve in the red represents iV curve with a In top contact.

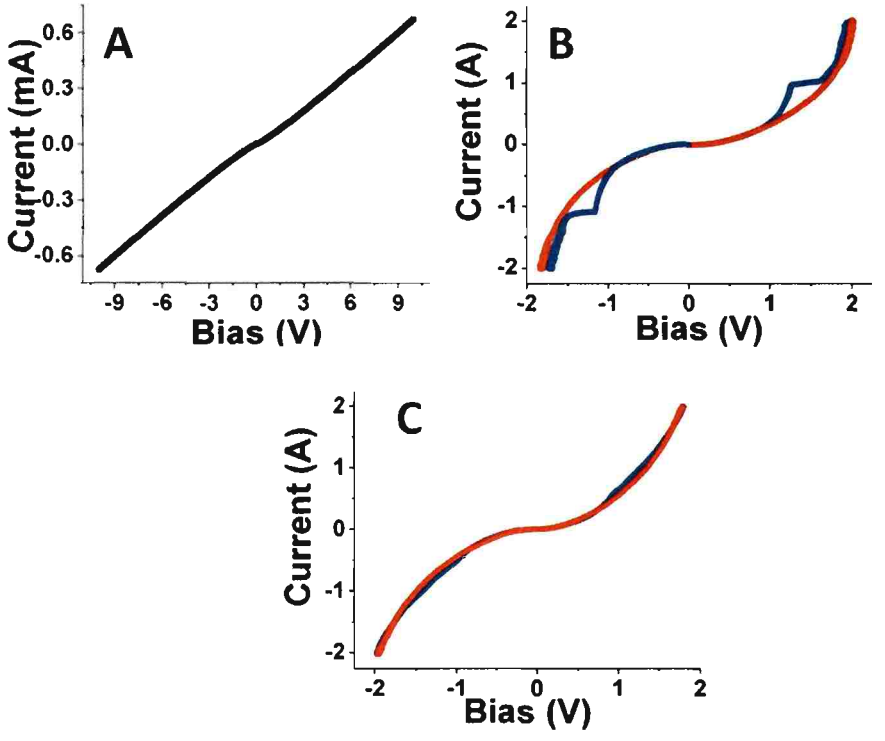

Figure S4.4. Current-voltage curves at 77 K on Fe_3O_4, obtained by sweeping the current and measuring the bias for (A) (111) commerical single crystal (B) epitaxial film on Au(111) produced at -1.03 V and (C) epitaxial film on Au(111) produced at -1.08 V vs Ag/AgCl. The single crystal and epitaxial films do not exhibit the high-to-low resistance jump that is observed in the polycrystalline films. The low-to-high resistance switch is most pronounced in the non-stoichiometric film deposited at -1.03 V vs Ag/AgCl.

APPENDIX C.

MAGNETIC CHARACTERIZATION OF MAGNETITE, ZINC FERRITE FILMS AND SUPERLATTICES

Experimental Section

Magnetic measurements were carried out with a Quantum Design Physical Property Measurement System (PPMS). A vibrating sample magnetometer (VSM) Model P525 was used for magnetization and hysteresis measurements. A sample mounted on a quartz tube was vibrated using a linear motor at 40 Hz while the pick-up coils located around the sample detected its magnetization. The applied magnetic field was parallel to the plane of the substrate. The measurements were carried out by sweeping the temperature at 5 K/min at the desired magnetic field while continuously monitoring the magnetization. Hysteresis measurements were carried out at a fixed temperature by sweeping the magnetic field at 50 Oe/sec. The discontinuities in the magnetization data caused by the sample centering operation performed on the VSM accessory at every 10 K increments in the temperature.

Magnetoresistance measurements were carried out in the PPMS using the resistivity option for the instrument. Contacts were made to the top of the film and the Au/glass substrate using pressed In metal. The sample was then mounted on a Cu sample puck using varnish purchased from Lakeshore Cryotonics Inc. so as to ensure good thermal contact with the puck. The magnetoresistance ratio is defined as $MR = (R_{Hs} - R_0)/ R_{Hs}$. Where R_0 is the resistance measured without any magnetic field applied at a fixed temperature, and R_{Hs} is the resistance measured at the same temperature with applied magnetic field of R_{Hs}.

Current-voltage (iV) measurements were carried out in the PPMS using the ACT option for the instrument. Instead of using four contacts on the film, two contacts were used and the scheme for attaching the wires to the puck was slightly modified.

Results and Discussions

Magnetic characterization was carried out on a commercial $Fe_3O_4(111)$ single crystal purchased from Commercial Crystal Laboratories, Inc. Figure C.1 (A) shows the magnetic hysteresis loop at 300 K on the crystal. A saturation magnetization value of 81.6 emu/g was obtained for the crystal. Figure C.1 (B) shows the resistance variation as a function of temperature. The resistance increases abruptly at temperatures below 119 K. This temperature is referred to as the Verwey transition temperature. Above the Verwey

transition temperature magnetite has a cubic structure and is highly conducting. Magnetite undergoes a phase transformation below the Verwey temperature and becomes insulating. Figure C.1 (C) shows the FC and ZFC curves on the crystal. The ZFC and FC magnetization curves on the single crystal show a sudden jump in the moment around the Verwey transition for Fe_3O_4. Figure C.1 (D) shows the MR scan on the crystal at 300 K. A magnetoresistance value of ~-1.5% was obtained at 300 K in a magnetic field of 90000 Oe (9 T).

Further, magnetic characterization was also carried at different temperatures to study the behavior of the single crystal. Figure C.2 shows the magnetic hysteresis loops obtained at 5 K and 45 K. There was no noticeable change in the saturation magnetization from that obtained at 300 K at these temperatures. The saturation magnetization value obtained was 85.6 emu/g. Figure C.3 shows the MR scans obtained at 77 K and 119 K. A magnetoresistance value of ~-2.2 % was obtained at 77 K. A magnetoresistance plot was also obtained near the Verwey transition temperature by holding the temperature at 119 K and varying the magnetic field. A magnetoresistance value of ~-2.2 % was obtained at this temperature. There were no drastic changes in resistance by varying magnetic field at the Verwey transition temperature.

Films of Fe_3O_4 were prepared by electrochemical reduction of Fe(III)-TEA complex at 80 ^{o}C. The films were deposited onto Au wire, Au/glass substrate, and Au(111) single crystals for different measurements. Fe_3O_4 films were deposited with 10 mV increments using potentials ranging between -1.01 V to -1.07 V vs. Ag/AgCl. Figure C.4 shows the magnetic hysteresis loops at 300 K for Fe_3O_4 films deposited at different potentials on Au(111) single crystal. All the films were grown to a thickness of 2 μm by passing 1 C/cm^2 charge. Figure C.5 shows the coercivity and saturation magnetization of all the films as a function of deposition potential. All the films reach saturation magnetization at fields around 1000 Oe or lower. The saturation magnetization of -1.065 V Fe_3O_4 film was slightly higher (~30 emu/g) than the films grown at other potentials but the value was not comparable to the commercial magnetite (111) single crystal (~82 emu/g) as shown in Figure A.5 the coercivity of the films decreases with increasing potential. Figure C.6 shows the coercivity calculation for a -1.065 V Fe_3O_4 film. Diamagnetism of Au substrate becomes a major factor and the moment starts to decrease

at higher fields. For saturation magnetization, the amount of the material electrodeposited on the substrate was determined using the following equation.

$$T = w/AD \quad (1)$$

Where, T = thickness of the film

w = weight of the deposited film

A = area of the deposit

D = density of the film

Fe_3O_4 films were electrodeposited at different potentials on Au(111) substrate for resistivity measurements. Resistance measurements on the films were carried out using two point contacts. Since the films are resistive the contact resistance was ignored. Two silver wires were attached, one to the top of the Fe_3O_4 film and the other to the Au(111) substrate using indium metal. The resistance was measured as a function of the temperature. The temperature was ramped from 300 K to 10 K and the data was collected at every 10 K. To get a precise value of the Verwey temperature, the data was collected at every 1 K near the Verwey transition region. Figure C.7. shows the resistance vs. temperature plot of films deposited at different potentials. Figure C.7 (G) shows the resistance vs. temperature plot for the Fe_3O_4 film deposited at -1.065 V vs. Ag/AgCl. The plot shows that the Verwey transition temperature is ~123 K which is very close to the theoretical value for a stoichiometric magnetite film. It is observed that the Verwey transition temperature is shifted to lower temperatures for non-stoichiometric films. There was no particular trend observed in the Verwey temperature for the films grown at different potentials.

Films of zinc ferrite ($Zn_xFe_{2-x}O_4$) were deposited from a solution containing 87 mM Fe(III), 30 mM Zn(II), 100 mM TEA, and 2 M NaOH. 30 mM Zn(II) was added to a solution containing Fe(III)-TEA and the solution was stirred for 2-3 hours before use. Films of $ZnFe_2O_4$ were deposited at 80 ^{o}C at different potentials vs. Ag/AgCl. All chemicals were ACS reagent grade and purchased from Sigma-Aldrich. $ZnFe_2O_4$ films were deposited with 10 mV increments from potentials ranging between -0.97 V to -1.06 V vs. Ag/AgCl. Figure C.8 shows the magnetic hysteresis loops at 300 K for $ZnFe_2O_4$ films deposited on Au(111) substrate.

Superlattices in the magnetite/zinc ferrite system were deposited as described in paper I of this thesis. In the case of magnetite superlattices, the potentials used were -1.01 V and -1.065 V vs. Ag/AgCl. A detailed magnetic study has been performed on the individual films deposited on Au(111) at these potentials. Figure C.9 shows the magnetic hysteresis at 300 K, 77 K, 45 K and 5 K for the Fe_3O_4 films grown at -1.01 V and -1.065 V on Au(111) single crystal. As we go to lower temperatures the hysteresis loops becomes squarer. One of the defect chemistry superlattices in the magnetite system with 12.2 nm modulation wavelength was selected for magnetic measurements. Figure C.10 shows the magnetic hysteresis of the superlattice at 300 K, 77 K, and 45 K. Hysteresis loops for the individual films and superlattice have similar features and do not show any noticeable differences.

Magnetization measurements on the films were carried out using the vibrating sample magnetometer (VSM) accessory on the PPMS. Zero field cooled (ZFC) measurements were run by cooling the sample to 4 K in zero applied field and heating the sample in the presence of a small magnetic field. Field cooled (FC) measurements were run by cooling the sample to 4 K in the presence of an applied magnetic field and then heating the sample to room temperature in the presence of the same magnetic field. The measurements for all the samples were carried out with an applied magnetic field of 100 Oe. Measurements taken at other magnetic fields did not show any noticeable changes. Figure C.11 shows the FC and ZFC curves for an Fe_3O_4 films electrodeposited on Au(111) substrate at (A) -1.01 V and (B) -1.065 V vs. Ag/AgCl. The FC curves of both the films do not give much information. The moment in the FC curve in Figure C.11 (B) decreases sharply after the Verwey transition temperature of 123 K. This temperature is consistent with the resistivity measurements on the film. Whereas, the FC curve in Figure C.11 (A) has no features and is flat. The shape of the FC curve is very sensitive to the stoichiometry of the films. The ZFC data shows a sharp decrease in moment for -1.065 V film after 123 K and has a gradual decrease in moment for -1.01 V film. The broad transition of -1.01 V Fe_3O_4 films can be attributed to the non-stoichiometry.[1-4]

Similarly, FC and ZFC curves for individual layers of $ZnFe_2O_4$ superlattice were run. The individual films of $ZnFe_2O_4$ were electrodeposited on Au(111) substrate at -0.99 V and -1.05 V vs. Ag/AgCl. Figure C.12 (A) and (B) shows the FC and ZFC curves for

-0.99 V and -1.05 V $ZnFe_2O_4$ films. Unlike Fe_3O_4 films, $ZnFe_2O_4$ FC and ZFC curves do not show any sharp increase in the moment at lower temperatures.

Magnetoresistance (MR) measurements on the individual layers in the magnetite superlattice electrodeposited on Au(111) single crystal were carried out in the PPMS in the resistivity option mode. Figure C. 13 (A) shows the MR scan at 300 K for a Fe_3O_4 film electrodeposited on Au(111) at -1.01 V vs. Ag/AgCl at 80 °C. A low magnetoresistance value of ~-0.25 % was obtained. Figure A.13 (B) shows the MR scan for a film deposited at -1.05 V. A magnetoresistance value of ~-0.4% was obtained. In the case of a superlattice, with a modulation wavelength of 12.2 nm, a magnetoresistance value of ~-1.2% was obtained. MR scans at 300 K for the films and superlattice are not very symmetrical and very noisy. This can be attributed to either the oxidation of the films, which changes the resistance of the film or to the temperature instability near the surface of the film. MR scans were also obtained on these films and superlattice at other temperatures. Figure C.14 (A) shows the MR plot for a Fe_3O_4 film electrodeposited at -1.01 V on Au(111). The resistance of the film initially increases with the increase in the magnetic field. At 3500 Oe (0.3 T) the resistance switches and decreases on further increase of magnetic field. Approximately a positive magnetoresistance of 0.05% and a negative magnetoresistance of 0.8% are obtained for the -1.01 V Fe_3O_4 film. For a film grown at -1.05 V, a similar behavior is seen where the resistance of the film increases initially and switches at around 5000 Oe (0.5 T) after which it decreases. Approximately a positive magnetoresistance of 0.13% and a negative resistance of 0.85% are obtained for the film. In the case of a superlattice, the behavior remained the same with a switch at around 5500 Oe (0.55 T). A positive magnetoresistance of 0.16% and a negative magnetoresistance of 0.7% were obtained. When the temperature was further lowered to 45 K, the positive magnetoresistance of the films and superlattice increased dramatically. Figure C. 15 (A) shows the MR scan for the film electrodeposited at -1.01 V at 45 K. A positive MR of 0.2% and a negative MR of 0.9% were obtained with a switching happening at around 7000 Oe (0.7 T). In case of -1.05 V Fe_3O_4 film, a positive MR of 1.1% and negative MR of 1.3% were obtained with switching happening at around 7000 Oe (0.7 T). For a superlattice with modulation wavelength of 12.2 nm, a positive MR of

~0.5 % and negative MR of ~1% were obtained with switching happening at around 5800 Oe (0.58 T).

The increase in resistance followed by a decrease was also observed in the case of $(Fe_xSn_{1-x})_{1-y}(SiO_2)_y$ films fabricated by RF magnetron sputtering.[5] The variation in MR was attributed to anisotropic magnetoresistance (AMR).[5] We did not do in plane MR measurements on the electrodeposited magnetite films. All the measurements were out of plane of the film. It is possible that we may get completely different results with the field parallel to the film.

Similarly, MR scans for zinc ferrite films were obtained at various temperatures. Figure C.16 shows the MR scans at 300 K for zinc ferrite films electrodeposited at (A) -0.99 V and (B) -1.05 V vs. Ag/AgCl. Figure C.16 (C) shows the MR scan at 300 K for a zinc ferrite superlattice with a modulation wavelength of 16.6 nm. The MR scan for both the films and the superlattice at 300 K are not symmetrical and are very noisy. One reason why this can be happening is due to the instability of temperature near the film. A magnetoresistance of ~-4.5% was measured for a -0.99 V film. On the other hand, a magnetoresistance of ~-7% was measured for the -1.05 V zinc ferrite film. Superlattice produced by pulsing the potentials between -0.99 V and -1.05 V gave a magnetoresistance of ~-3.5%. MR scans were also done at lower temperature to study the behavior of the films. Figure C.17 shows the MR scans for the zinc ferrite films at 100 K. Unlike the magnetite films, zinc ferrite films do not show any positive magnetoresistance. Figure C. 17 (A) shows the MR scan at 100 K for the zinc ferrite film electrodeposited at -0.99 V. The MR scan shows that the resistance decreases with increase in magnetic field till about 0.1 T and then it stabilizes till 0.65 T and on further increase in magnetic field the resistance decreases. However, the zinc ferrite film deposited at -1.05 V does not show such a behavior. Both the films showed ~-3.5 % MR. Similarly, the MR scans obtained at 45 K (Figure C.18) for these films show a similar behavior and have a %MR of about ~-5%. Incorporation of zinc ion into the Fe_3O_4 lattice may affect the magnetic interactions and might result in such behaviors. Similar MR curves were observed by Batle et.al for $Co_{34}Fe_8$–$Ag_{54}Cu_4$ thin films.[6, 7] The double peak in the MR scan was attributed to the interplay between the size of the particles and anisotropic

magnetoresistance in the film.[3] In our electrodeposited films we did not check for the AMR behavior but it is certainly possible that it might be a cause for such behavior.

REFERENCES

1. S. B. Ogale, K. Ghosh, R. P. Sharma, R. L. Greene, R. Ramesh, and T. Venkatesan, Phys. Rev. B 57, 7823 (1998).

2. D. T. Margulies, F. T. Parker, f. E. Spada, R. S. goldman, J. Li, R. Sinclair, and A. Berkowitz, Phys. Rev. B 53, 9175 (1996).

3. J. B. Yang, x. d. Zhou, W. B. Yelon, W. J. James, Q. Cai, K. V. Gopalakrishnan, S. K. Malik, X. C. Sun, and D. E. Nilkes, J. Appl. Phys. 95, 7540 (2004).

4. J.P. Hong, s. B. Lee, Y. W. Jung, J. H. Lee, K. s. Yoon, K. W. Kim, C. Q. Kim, C. H. Lee, and M. H. Jung, Appl. Phys. Lett. 83, 1590 (2003).

5. J. Wang, W. Zou, Z. Lu, Z. Lu, X. Liu, J. Xu, Y. Lin, L. Lv, F. Zhang, and Y. Du, J. Phys. D: Appl. Phys. 40, 2425 (2007).

6. V. Franco, X. Batlle, and A. Labarta, Eur. Phys. J. B 17, 43 (2000).

7. X. Batle, and A. Labarta, J. Phys. D: Appl. Phys. 35, R15 (2002).

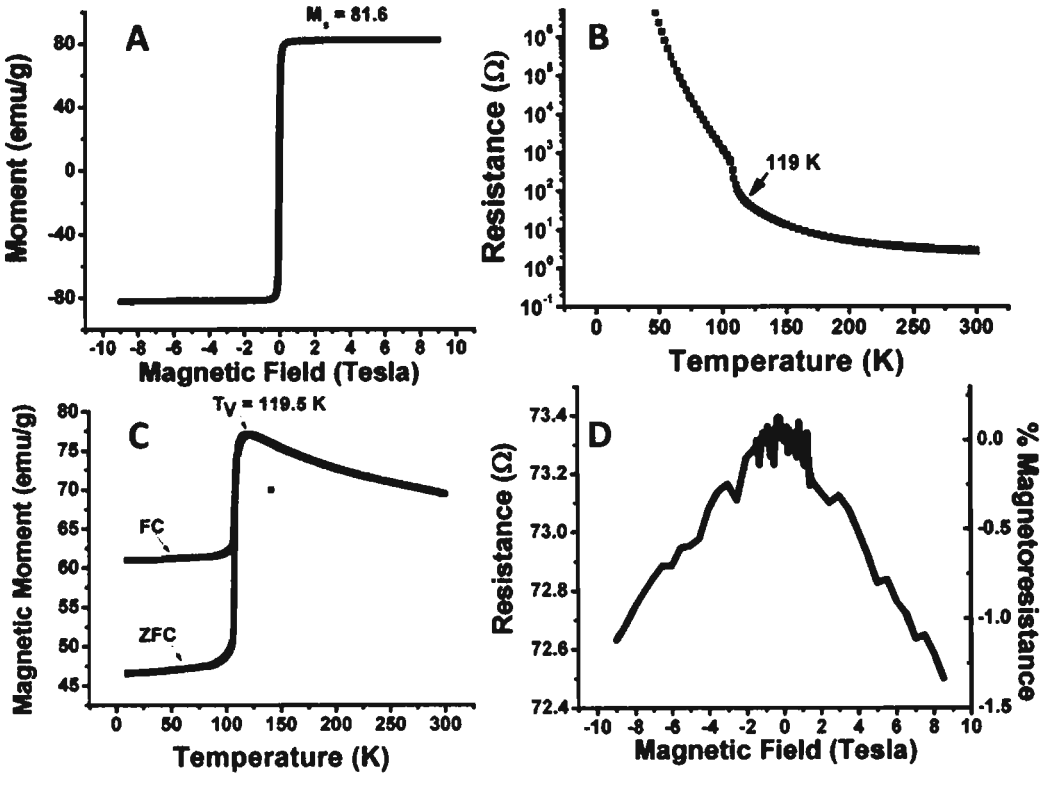

Figure C.1. Magnetic data for a commercial magnetite (111) single crystal. (A) Magnetic hysteresis data for the commercial magnetite (111) crystal at 300 K. The saturation magnetization obtained is about 81.6 emu/g. (B) Resistance vs temperature plot showing the Verwey transition at 119 K. (C) FC and ZFC magnetization data indicating a Verwey transition temperature of 119.5 K. (D) Magnetoresistance plot at 300 K showing ~-1.25% magnetoresistance.

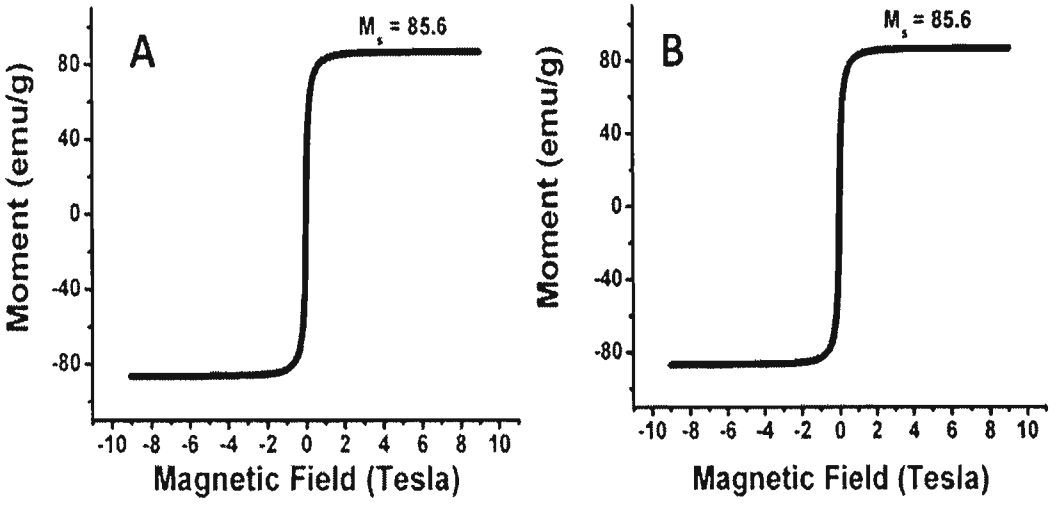

Figure C.2. Magnetic hysteresis data for commercial magnetite (111) single crystal at different temperatures (A) At 5 K and (B) At 45 K.

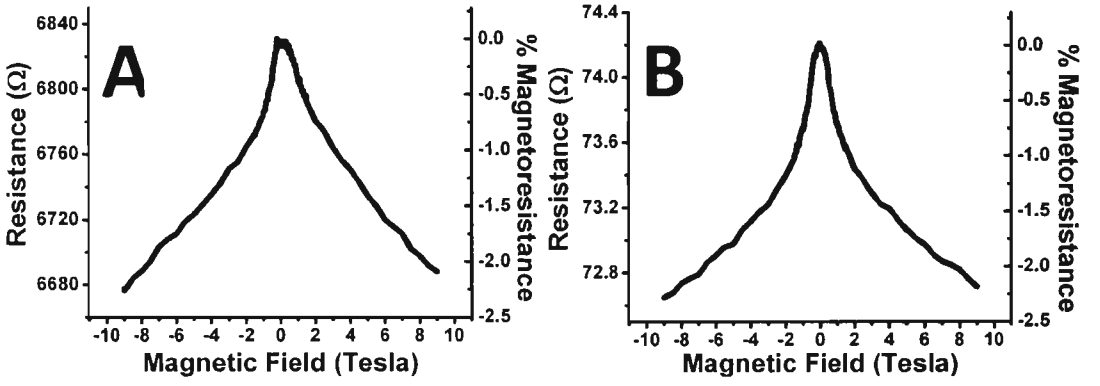

Figure C.3. Magnetoresistance measurement on commercial magnetite (111) single crystal at different temperatures. (A) At 77 K and (B) At 119 K.

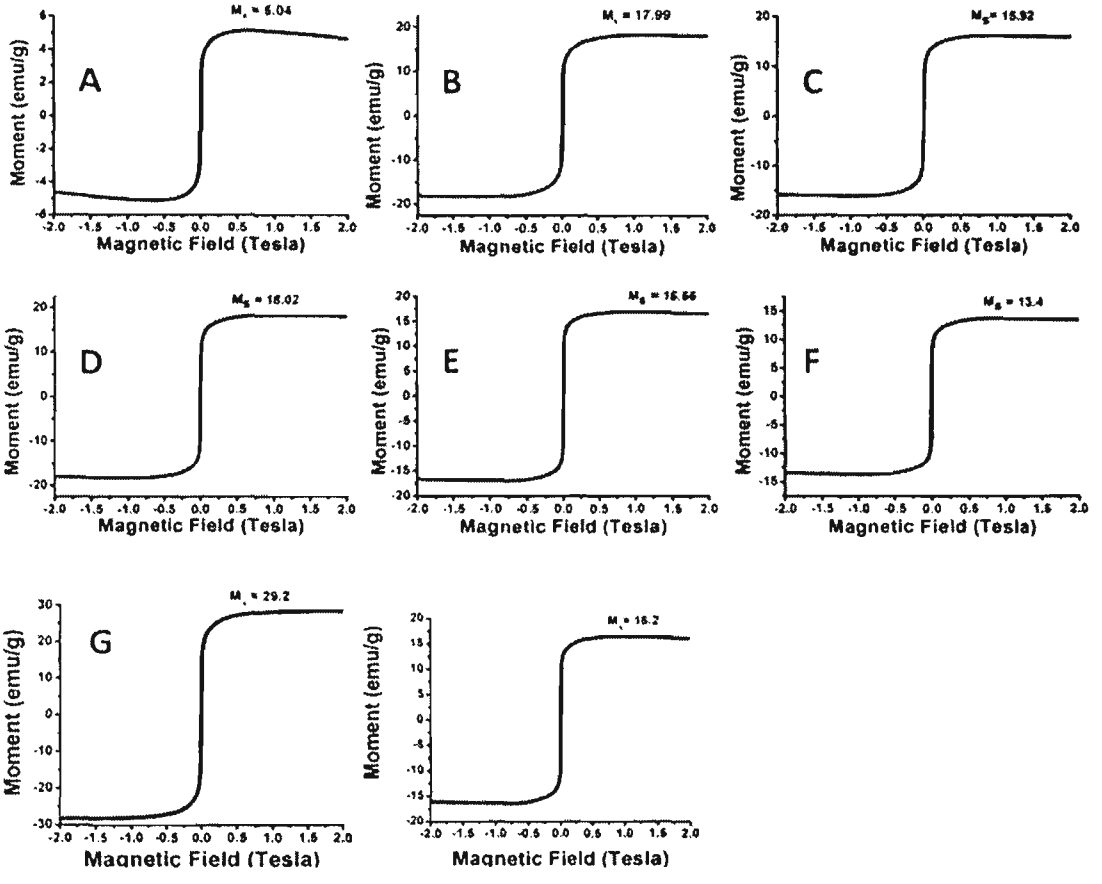

Figure C.4. Magnetic hysteresis data for the electrodeposited Fe_3O_4 films on Au(111) at different potentials at 300 K. (A) -1.01 V (B) -1.02 V (C) -1.03 V (D) -1.04 V (E) -1.05 V (F) -1.06 V (G) -1.065 V (H) -1.07 V.

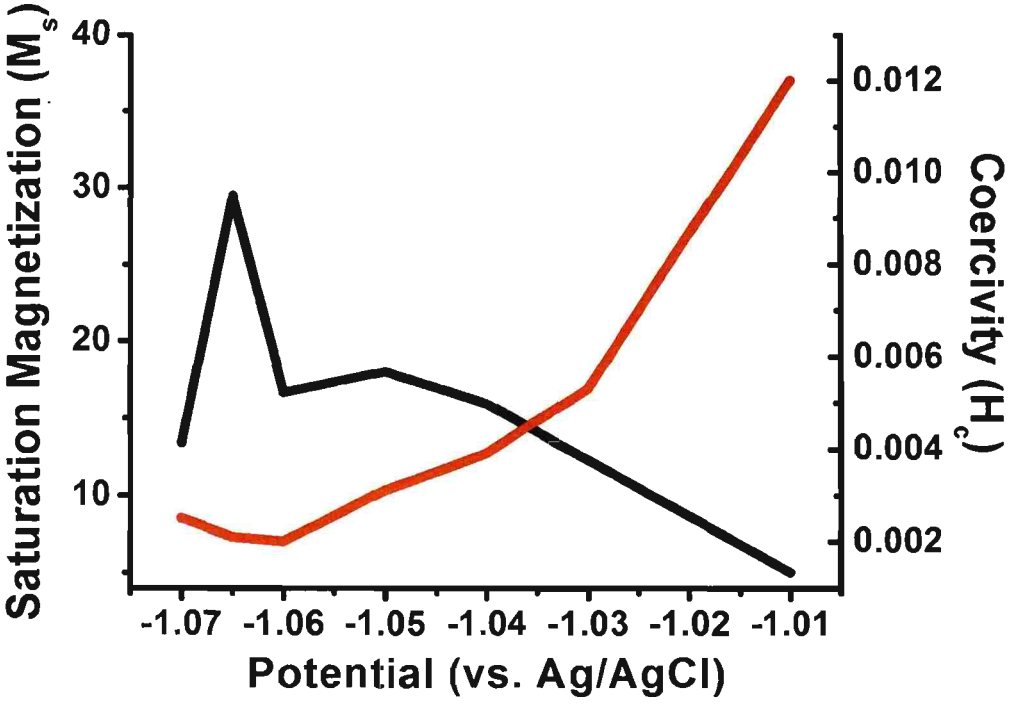

Figure C.5. Plot showing saturation magnetization (black) and coercivity (red) with respect to applied potential for electrodeposited Fe_3O_4 films on Au(111) single crystal at different potentials.

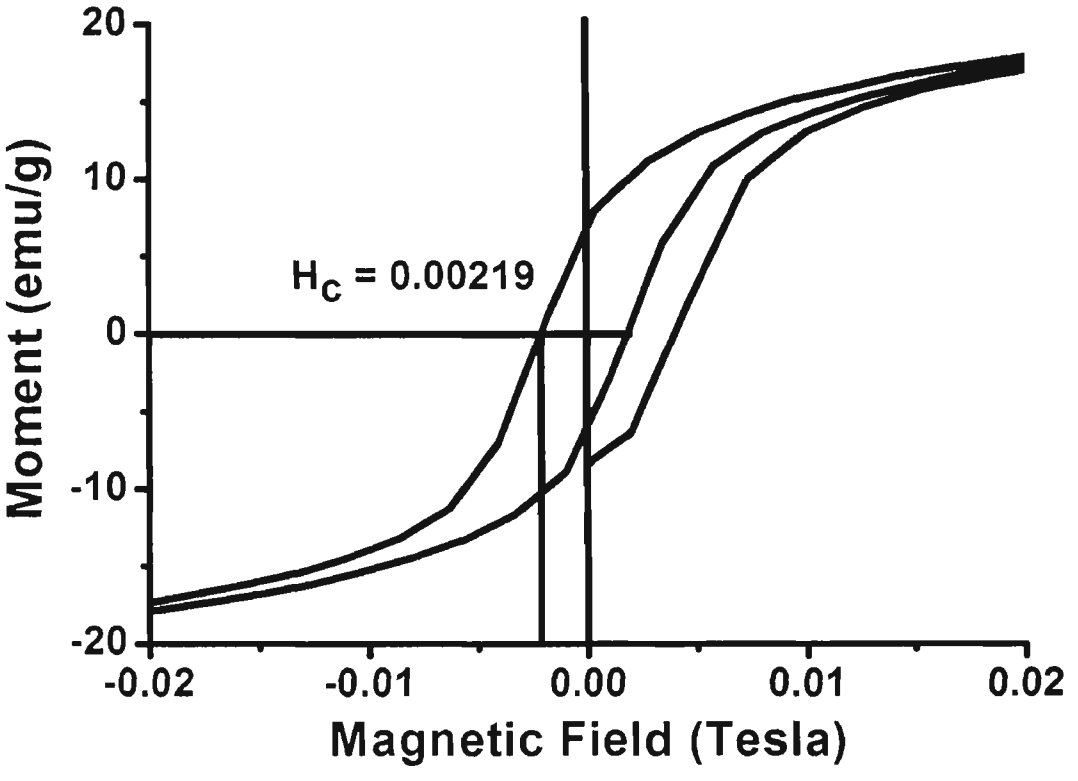

Figure C.6. Plot showing the coercivity determination for a electrodeposited -1.065 V Fe_3O_4 film on Au(111).

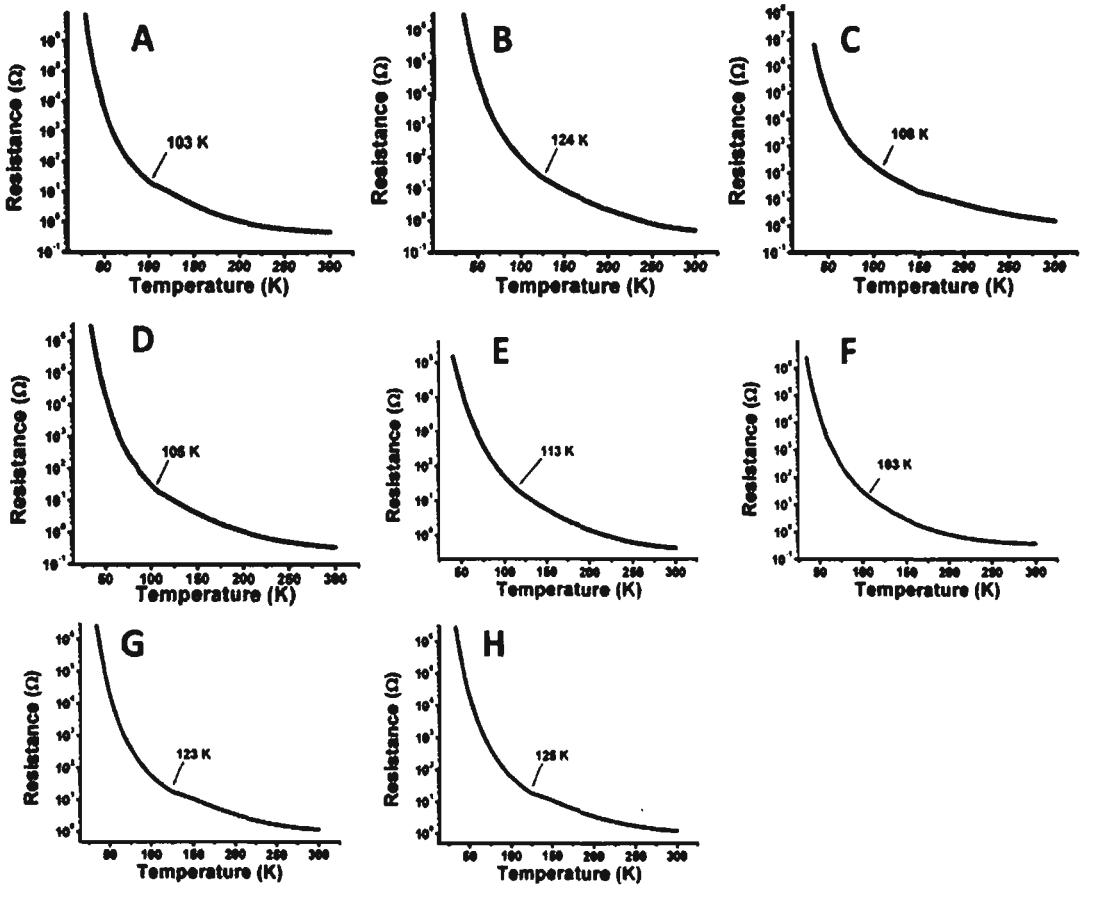

Figure C.7. Resistance vs. temperature plot for Fe_3O_4 films electrodeposited on Au(111) single crystal at different potentials. (A) -1.01 V (B) -1.02 V (C) -1.03 V (D) -1.04 V (E) -1.05 V (F) -1.06 V (G) -1.065 V (H) -1.07 V. Arrow on each plot shows the Verwey transition temperature.

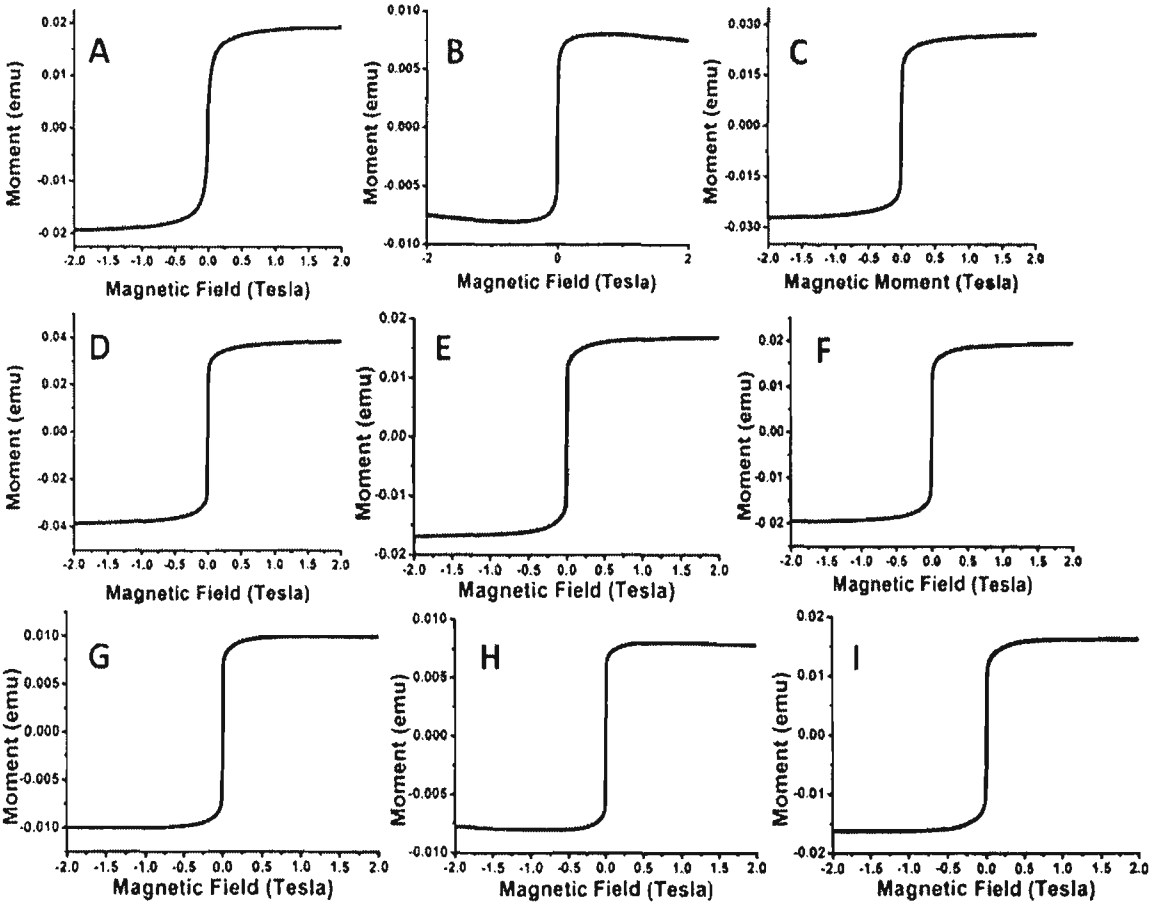

Figure C.8. Magnetic hysteresis data for the electrodeposited zinc ferrite films on Au(111) at different potentials at 300 K. (A) -0.97 V (B) -0.98 V (C) -0.99 V (D) -1.0 V (E) -1.01 V (F) -1.02 V (G) -1.03 V (H) -1.04 V and (I) -1.05 V.

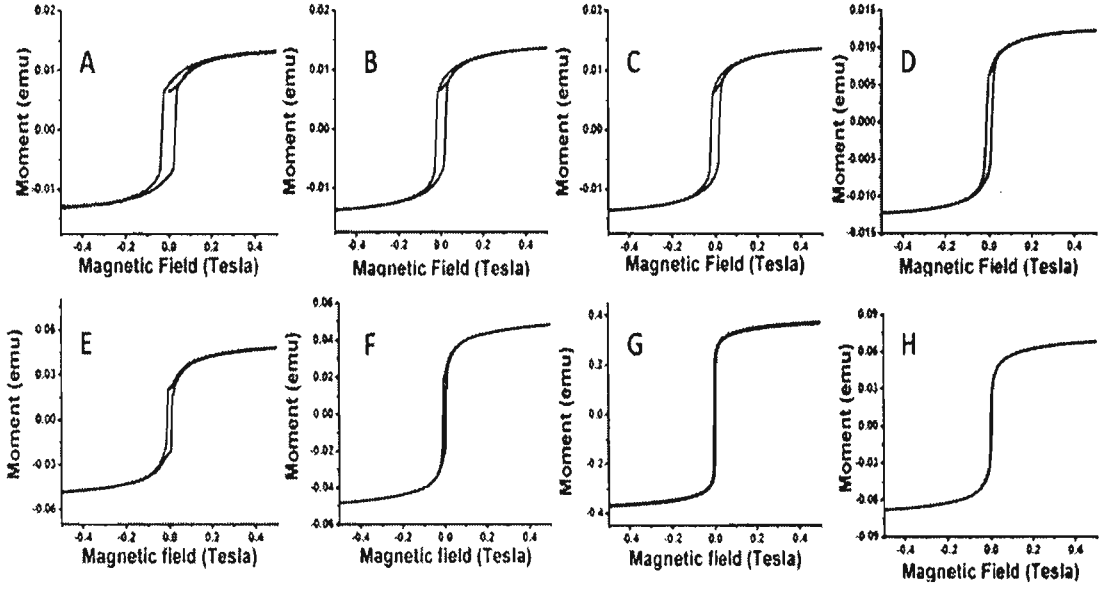

Figure C.9. Magnetic hysteresis loops at (A) 5 K, (B) 45 K, (C) 77 K, (D) 300 K for a Fe_3O_4 film electrodeposited on Au(111) at -1.01 V vs. Ag/AgCl and hysteresis loop at (E) 5 K, (F) 45 K, (G) 77 K, and (H) 300 K for a Fe_3O_4 film electrodeposited at -1.065 V vs. Ag/AgCl.

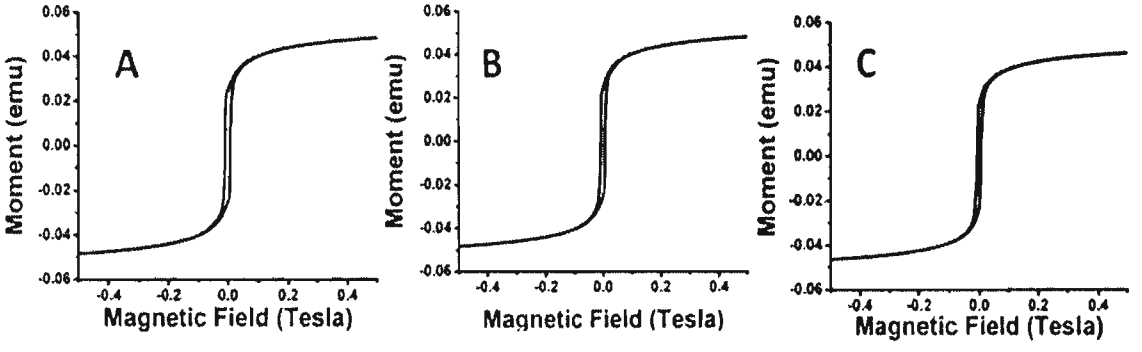

Figure C.10. Magnetic hysteresis loops at (A) 45 K, (B) 77 K, and (C) 300 K for a magnetite superlattice with a modulation wavelength of 12.2 nm on Au(111) single crystal.

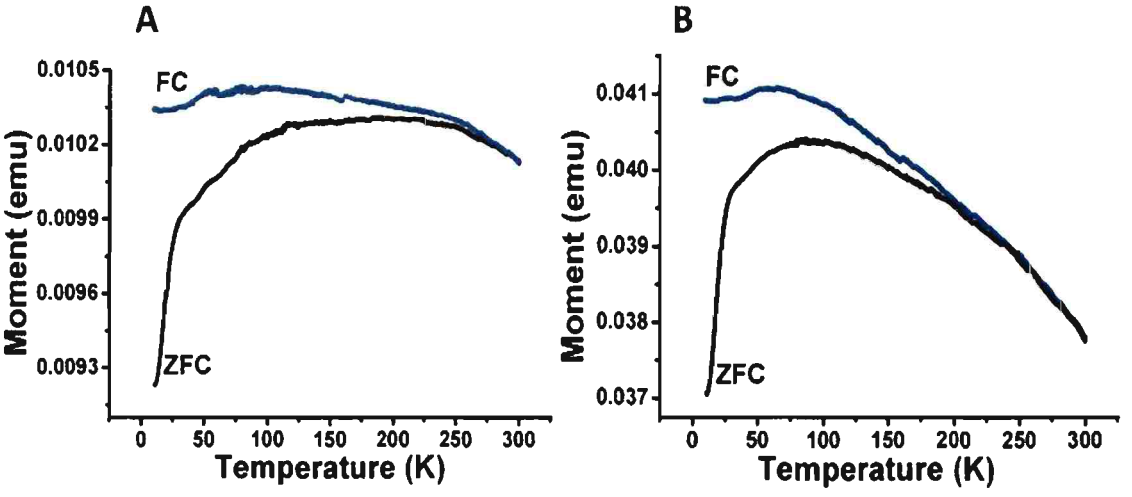

Figure C.11. ZFC and FC magnetization data for electrodeposited Fe_3O_4 films on Au(111) at (A) -1.01 V and (B) -1.05 V vs. Ag/AgCl. The scans were obtained at an applied field of 100 Oe.

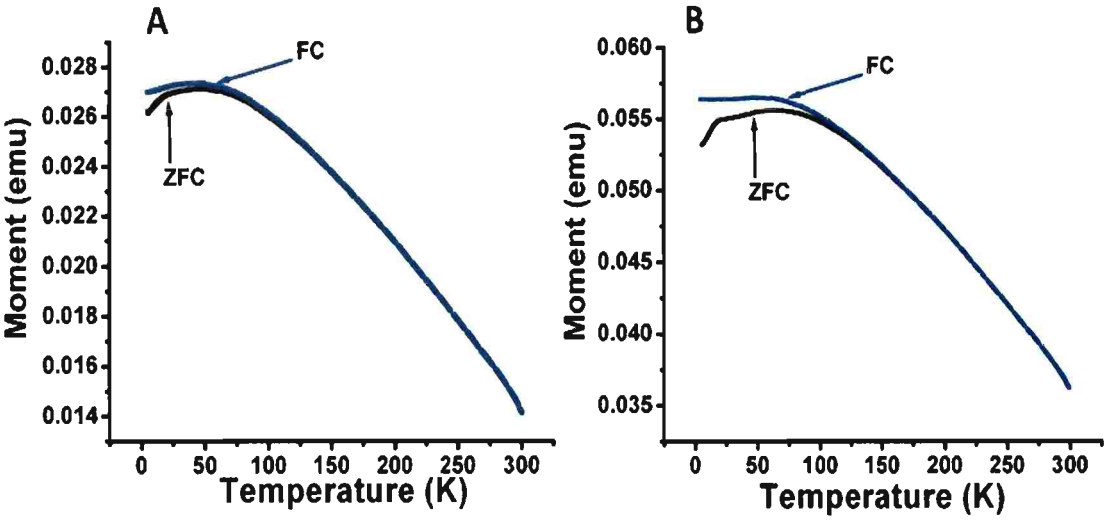

Figure C.12. ZFC and FC magnetization data for electrodeposited zinc ferrite films on Au(111) at (A) -0.99 V and (B) -1.05 V vs. Ag/AgCl. The scans were obtained at an applied field of 100 Oe.

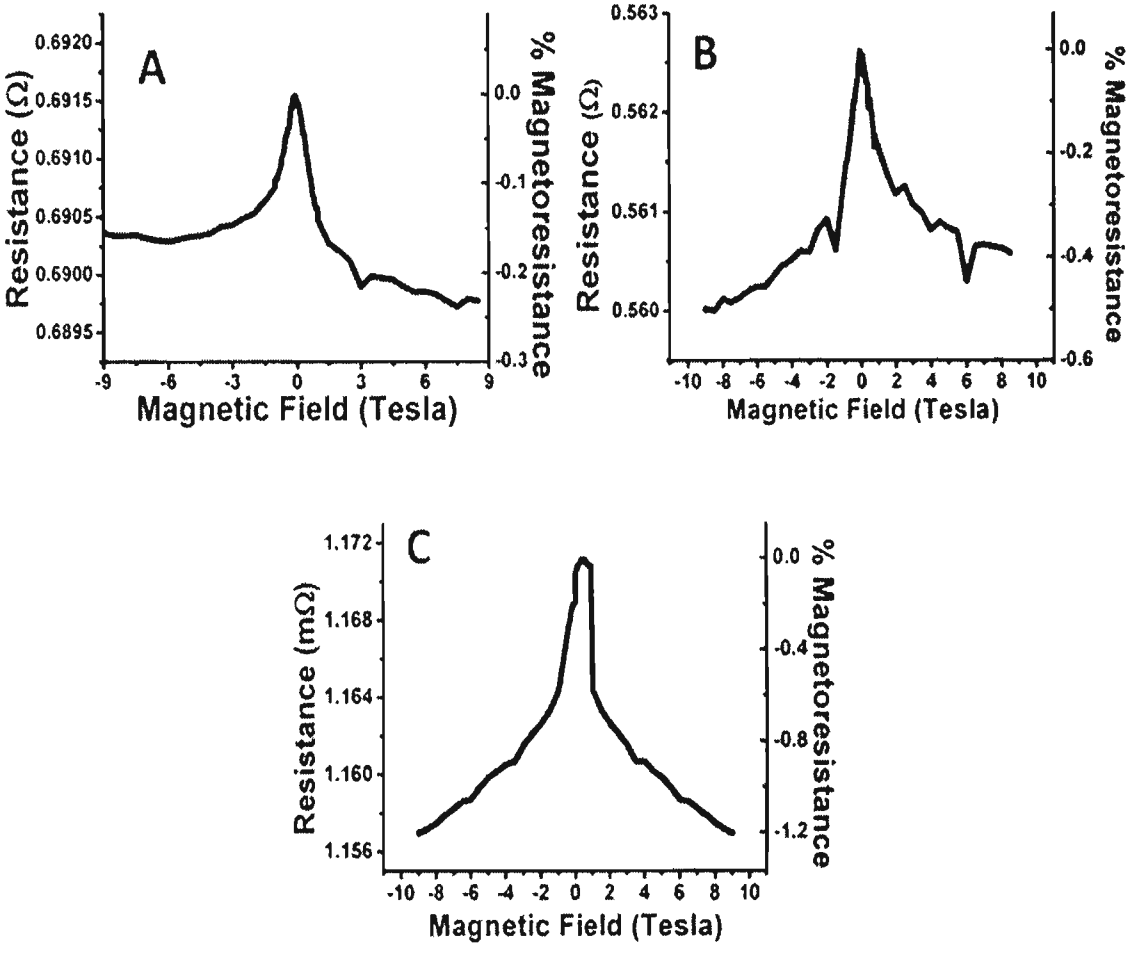

Figure C.13. Magnetoresistance measurement at 300 K for magnetite films electrodeposited at (A) -1.01 V (B) -1.05 V vs. Ag/AgCl and (C) magnetite superlattice with a modulation wavelength of 12.2 nm obtained by pulsing the potential at -1.01 V for 2 s and -1.05 V for 0.5 s.

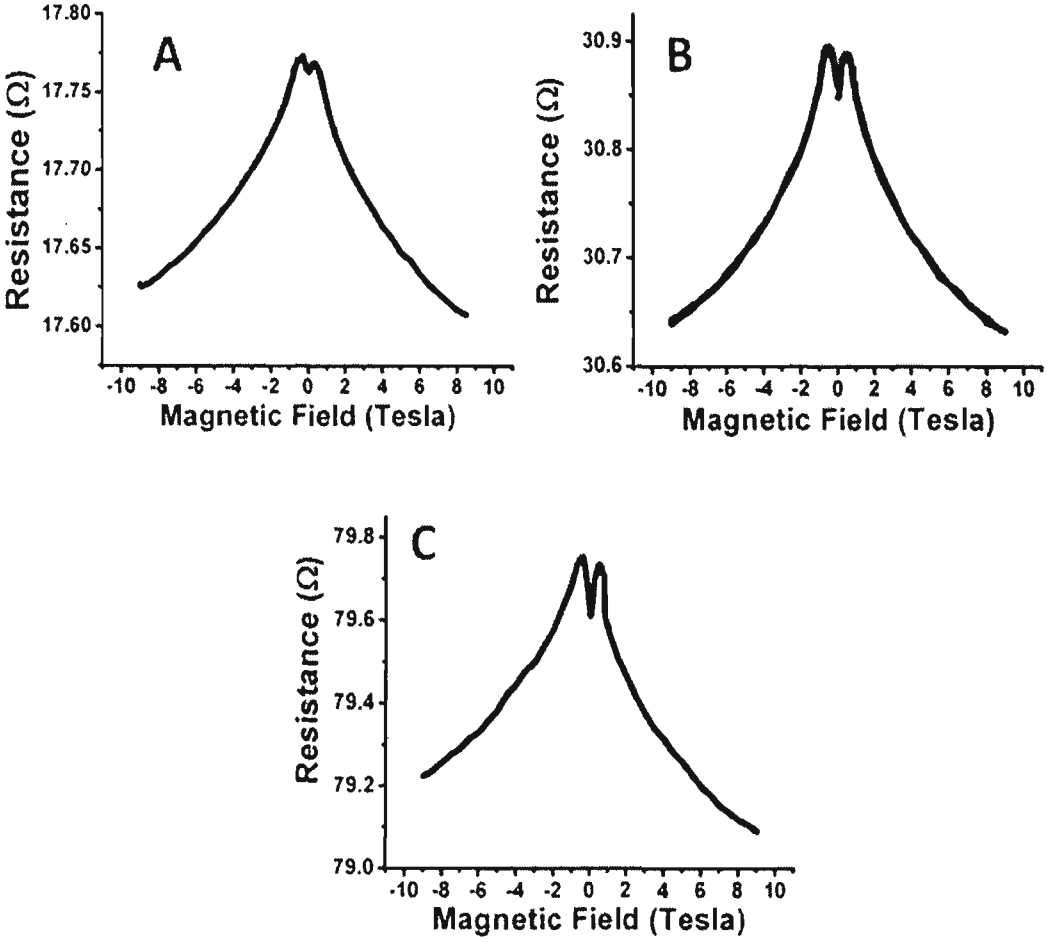

Figure C.14. Magnetoresistance measurement at 100 K for magnetite films electrodeposited at (A) -1.01 V (B) -1.05 V vs. Ag/AgCl and (C) magnetite superlattice with a modulation wavelength of 12.2 nm obtained by pulsing the potential at -1.01 V for 2 s and -1.05 V for 0.5 s.

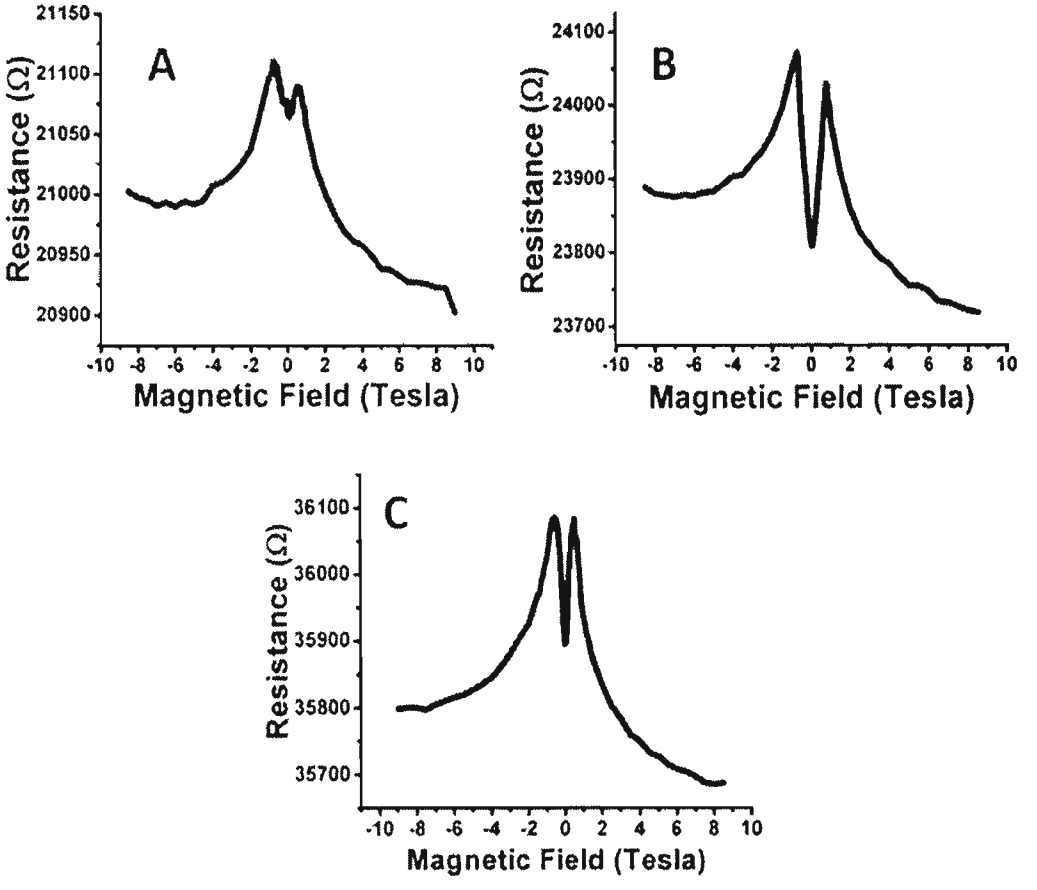

Figure C.15. Magnetoresistance measurement at 45 K for magnetite films electrodeposited at (A) -1.01 V (B) -1.05 V vs. Ag/AgCl and (C) magnetite superlattice with a modulation wavelength of 12.2 nm obtained by pulsing the potential at -1.01 V for 2 s and -1.05 V for 0.5 s.

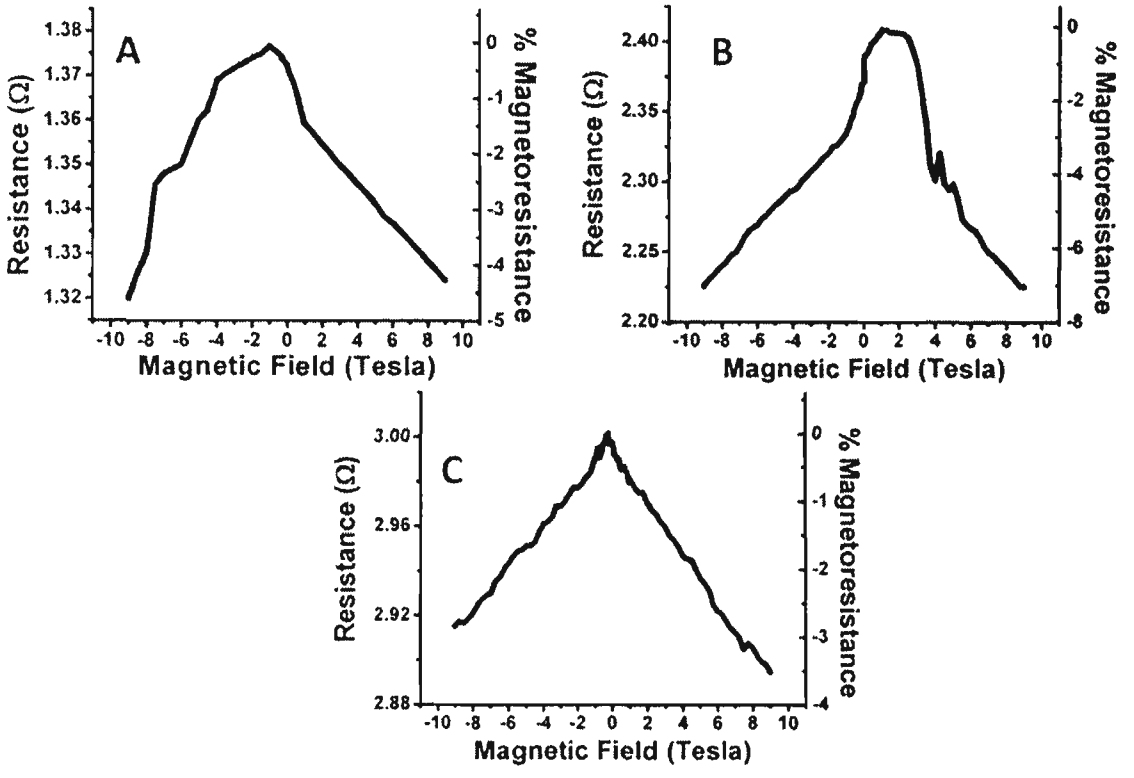

Figure C.16. Magnetoresistance measurement at 300 K for zinc ferrite films electrodeposited at (A) -0.99 V (B) -1.05 V vs. Ag/AgCl and (C) zinc ferrite superlattice with a modulation wavelength of 16.6 nm obtained by pulsing the potential at -0.99 V for 2 s and -1.05 V for 0.5 s.

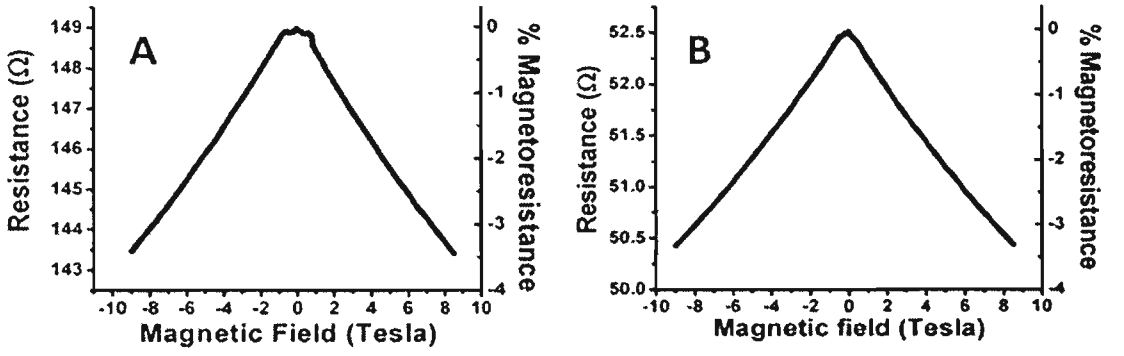

Figure C.17. Magnetoresistance measurement at 100 K for zinc ferrite films electrodeposited at (A) -0.99 V and (B) -1.05 V vs. Ag/AgCl.

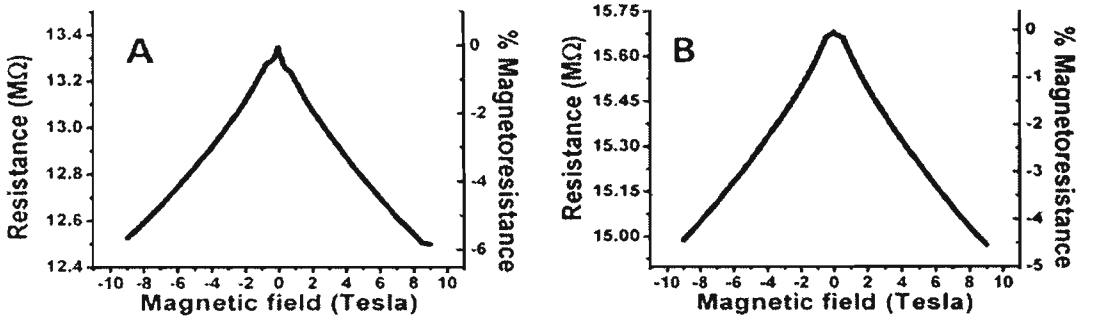

Figure C.18. Magnetoresistance measurement at 45 K for zinc ferrite films electrodeposited at (A) -0.99 V and (B) -1.05 V vs. Ag/AgCl.

APPENDIX D.

CHARACTERIZATION OF COMPOSITIONAL SUPERLATTICES IN THE MAGNETITE/ZINC FERRITE SYSTEM

Superlattices are good examples for non-equilibrium structures produced during electrodeposition.[1-4] The basic criterion for superlattices to grow uniformly is low mismatch between the layers and also epitaxy.[5] Bauer and van der Merwe have reviewed the requirement to grow a superlattice such as growth mode, lattice fit, supersaturation, and surface energies between the film and substrate.[6] The electrochemical growth of superlattices has been reported in metallic systems, semiconductors, and metal oxides.[1-4, 7-13] Electrodeposition of superlattices results in lesser inter-diffusion between the A and B layers as they are formed at or near room temperature.[14] Electrodeposition technique was used to deposit defect chemistry superlattices in the Tl_2O_3,[15] and Fe_3O_4[16] system. Compositional superlattices have been electrodeposited in Pb-Tl-O[17], Bi_2Te_3/ $(Bi_{0.3}Sb_{0.7})_2Te_3$[18] and zinc ferrite[16] systems.

Here, we characterize the films and compositional superlattices formed in the zinc ferrite system. The deposition bath for zinc ferrite films and superlattices contained 87 mM Fe(III), 30 mM Zn(II), 100 mM TEA, and 2 M NaOH. The solution was prepared by dissolving 2.6 grams of iron(III) sulfate pentahydrate in 15 ml of 1 M triethanolamine (TEA), resulting in a deep red-colored solution. It was diluted with 50 ml of deionized water. The diluted solution was then added to a second solution that was produced by adding 12.0 g of NaOH pellets to 85 ml of deionized water. To this bath 1.34 gm of zinc nitrate hexahydrate is added. The resulting 150 mL of gray-green solution was heated to 80 ^{o}C and stirred at a rate of 200 rpm. All chemicals were ACS reagent grade and purchased from Sigma-Aldrich. The water was produced in house by a Millipore system (18 MΩ-cm).

Zinc ferrite films were deposited on Au covered glass substrates at different potentials and lattice parameter was calculated at each potential. Figure D.1 shows the dependence of lattice parameter as a function of applied potential. The lattice parameter of the films approaches the literature value of $ZnFe_2O_4$ at more positive potentials. The zinc concentration in the films was measured by the energy dispersive spectroscopy (EDS). The current densities, measured Zn content and the lattice parameter at different potentials for the zinc ferrite films are listed in Table D.1. To determine the resistance of the films, the zinc ferrite films were electrodeposited on Au covered glass substrates and then peeled of on to a microscopic glass slides using super glue. The measured four-

probe resistivity of the freshly stripped films is shown in Table D.2. The sheet resistance of the films decreases with increasing potential.

X-ray diffraction experiments were carried out with a Philips X'Pert Materials Research Diffractometer (MRD) system. The Cu tube source was operated at 45 kV and 40 mA. Three types of experiments were performed. Phase analysis using 2θ scans to evaluate the film texture and modulation wavelength were carried out using a two-bounce Ge(220) asymmetric hybrid monochromator 2X (PW3147/00, Philips) on the incident beam side (primary optic) and 0.18° parallel plate collimator (PW3098/18, Philips) as the secondary optic on the detector side. The hybrid monochromator consists of a Göbel X-ray mirror and a two-crystal channel cut Ge(220) two-bounce monochromator. The parabolic-shaped graded multilayer X-ray mirror collimates the divergent beam from a line focus of the X-ray tube to a quasi-parallel beam. The hybrid monochromator gives pure Cu Kα1 radiation with a divergence of 25 arcseconds. The scans were acquired with a 2θ step size of 0.01° and a dwell time of 1 s/step. To obtain improved statistics around the satellite positions for the superlattice, the scans were acquired around the Bragg peaks with 2θ step size of 0.01° and a dwell time of 25 s/step. X-ray pole figures and azimuthal scans were obtained using an adjustable crossed slit collimator (PW3094/62, Philips), 2 x 2 mm, as the primary optic and a 0.27° parallel plate collimator (PW3098/27) with a graphite monochromator (PW3121/00) as the secondary optic.

Compositional superlattices in the zinc ferrite system were produced by pulsing the potential between -0.99 V and -1.05 V for different dwell times.[15] Figure D.2 shows the X-ray 2θ scan of superlattices in the zinc ferrite system with different modulation wavelengths. The 2θ scan for all the superlattices shows that they have (111) out of plane orientation. To determine the in-plane orientation of the films, x-ray pole figures were run on the films. Figure D.3 shows the (311) pole figures for the superlattices with different modulation wavelengths. Figure D.3 (A) shows the pole figure for the zinc ferrite superlattice with a modulation wavelength of 12.2 nm. The pole figure has sharp peaks at tilt angles of 29.5, 58.5, and 80°, corresponding to the (311) reflections of the (111) orientation. On the other hand, Figure D.3 (B) and (C) have extra peaks at tilt angles of 9, 40 and 67°, corresponding to (511) planes. The d-spacings for (333) and (511) planes are identical and hence the (511) reflection is not seen as a separate peak in

the 2θ scan. However, the pole figure proves the existence of the (511) orientation. It was shown earlier that (511) occur as a result of twinning of {111} peaks. Figure B.4 shows the (311) pole figures of the Au substrate. The epitaxial relationship which can be derived using the pole figures in Figure D.3 and Figure D.4 is as follows $Fe_3O_4(111)[01\bar{1}]//Au(111)[0\bar{1}1]$. Rocking curves were also run on the superlattices to determine the quality of epitaxy. Figure B. 5 shows the rocking curves of the (444) planes for the superlattices with different modulation wavelengths. The full width at half maximum (FWHM) for the 12.2 nm modulation wavelength superlattice is the lowest (0.33^{o}) and is comparable to the substrate FWHM (0.30^{o}), indicating that the superlattice is highly epitaxial with very small mosaic spread. In the case of superlattices with 29.2 nm and 16.5 nm modulation wavelengths, the rocking curve for the substrate was very broad with FWHM values of 0.68 and 1^{o} respectively. This resulted in broad rocking curves for the superlattices. X-ray 2θ scan can be used to determine the coherence length.[13, 19] The equation used for the coherence length calculation is as follows

$$L = 2\pi/\Delta q \tag{1}$$

Where q is the scattering vector given by $q=2\pi/d$, d is the lattice parameter in Å, and Δq is the peak width in the radial scan.[13, 20] Instrumental broadening was taken into account for the calculation as described by Kothari et al.[13] Table D.3 shows the coherence length for the three superlattices with varying modulation wavelengths. The coherence length of the superlattice with modulation wavelength 12.2 nm is ~5 times the modulation wavelength. As the modulation wavelength increases the coherence length decreases. This was also seen earlier with Pb-Tl-O superlattices and metallic superlattices.[13, 21]

The artificially imposed superperodicity manifests itself as satellite peaks around the Bragg reflection. The peak position of the satellites can be used to determine the modulation wavelength of the superlattices using the following equation.

$$\Lambda = \frac{\lambda(L_1 - L_2)}{2(\sin\theta_1 - \sin\theta_2)} \tag{2}$$

Where L_1 and L_2 are the order of the satellites, λ is the wavelength of the incident X-rays, and θ_1 and θ_2 are the positions of the high angle and low angle satellites on the 2θ scan. Figure D.6 shows a slow scan around the (444) reflection for a zinc ferrite superlattice with a modulation wavelength of 12.2 nm. The figure shows all the terms used in the equation for modulation wavelength calculation. Figure D.7 shows the slow scans around the (444) Bragg peak for zinc ferrite superlattices with different modulation wavelengths.

High angle annular dark field image shown in Figure D.8 clearly shows the layered structure in the zinc ferrite superlattice. In this case, the film was intentionally grown with a larger modulation wavelength of 70 nm, so that it can be easily imaged in the FIB. The superlattices with smaller modulation wavelengths were characterized using transmission electron microscopy (TEM). Figure D.9 shows the high angle annular dark field image of the zinc ferrite superlattice with a modulation wavelength of 16.5 nm. Figure D. 9 (A) shows the layered structure at low magnification. The layered structure is not readily apparent from the image at low magnification. Figure D.9 (B) shows the high magnification of the superlattice. The figure shows the bright and dark layers in the superlattice. The modulation wavelength determined from the image agrees with the calculated modulation wavelength from the satellite peak position from XRD. Further, to determine the composition in each layer of the superlattice, energy dispersive spectroscopy (EDS) line scan was performed on the selected region from the superlattice. Figure D.10 (A) shows the low magnification dark field STEM image of the compositional superlattice with 16.5 nm modulation wavelength. The image shows the selected region where the EDS scan was performed. Figure D.10 (B) shows the compositional profile in the selected region. The blue dots correspond to the Fe composition in the layer and the red dots correspond to the Zn composition. The EDS scan shows the composition variation in approximately 8 bilayers. The bright region in the image has a Zn concentration of ~25% and the dark region has ~20% Zn concentration. These numbers are in agreement with the EDS results obtained for the individual bulk films deposited at -0.99 V and -1.05 V. Figure D.11 shows the high resolution TEM (HR-TEM) image of the superlattice. The HR-TEM image shows big white spots which are artifacts formed during the sample preparation. These white spots made it harder to look at the individual layers of the superlattice as evident from Figure

D.12 (A). Besides the white spots, there were other artifacts like white patterns and black spots formed during the milling of the film in the FIB (Figure D.12 (B) and (C)). To avoid some of these problems, nano milling was performed on the sample. After nano milling, the sample looked much better and the individual layers in the superlattice were easily observable. Figure D.13 shows the high magnification image of the superlattice after nano milling. The inset in the figure shows the low magnification STEM image. It is not readily apparent from the high magnification image to mark out the individual layers. We tried to guess the individual layer based on the modulation wavelength obtained from the XRD experiments. Superlattices may be electrodeposited by pulsing between two potentials or two currents. Ross [21] showed that the pulsing between potentials results in sharper interfaces, but the layer thickness may vary. Our TEM experiments also suggests that the thickness of the layers is not very uniform, making it difficult to look through HR-TEM. One way to get around it is to use current pulses instead of potential pulses.

Resistance switching experiments were performed on the individual bulk films and the superlattices of zinc ferrite deposited on Au(111) substrate. In the resistance switching experiments, a contact is made to the top of the film and another contact is made to the Au(111) single crystal using In contacts. The sample is immersed in liquid nitrogen and all the measurements are done at 77 K. During the measurements, the applied current is swept from 0 to 2 A at 50 mA/s and the bias is measured. Figure D.14 (A) shows an iV curve for a zinc ferrite film deposited at -990 mV vs. Ag/AgCl. The iV curve is non-ohmic with multiple low-to-high jumps at positive biases of +3.8 V and +5.8 V and at negative biases of -3.7 V and -5.5 V. The iV curve for -1.05 V zinc ferrite film shown in Figure D. 14 (B) also shows a single low-to-high jump at applied bias of + 1.8 V and -1.6 V. Similarly, a zinc ferrite superlattice with a modulation wavelength of 12.2 nm had only low-to-high jump as shown in Figure D.14 (C). A similar transition has been observed before and has been attributed to oxidation of Fe_3O_4 to γ-Fe_2O_3.[16, 22] In this case, we do not clearly understand the mechanism for the low-to-high jump but we think that the jump might be occurring due to the oxidation of Fe^{2+} in the zinc ferrite to Fe^{3+}. At this point we do not have any evidence to prove the above reaction. Unlike the magnetite superlattices, zinc ferrite films and superlattices do not exhibit high-to-low resistance

switch corresponding to the insulator-to-metal phase transition. However, all the films exhibit oscillation of the bias voltage, followed by a negative differential resistance.

Compositional superlattices in the zinc ferrite system were also produced by choosing other potentials. In this case, the superlattices were produced by pulsing the potential between -0.96 V and -1.05 V for different dwell times as shown in Table D.4. These potentials were chosen because the difference in the zinc concentration in both the films was vastly different as shown Table D.1 and Table D.2. The film grown at -0.96 V had ~32% (atomic percentage) Zn concentration, close to pure zinc ferrite. On the other hand, -1.05 V film had ~20% (atomic percent) Zn concentration. The sheet resistance of the films was also vastly different as shown in Table 1. However, the lattice parameter was still close enough to deposit superlattices. Figure D.15 shows the 2θ scans for the superlattices electrodeposited on Au(111) with different modulation wavelengths. All the films have (111) out of plane orientation. To determine the in-plane orientation of the films, x-ray pole figures were run. Figure D.16 shows the satellites obtained from the slow scan around the (333) and (444) Bragg peaks of zinc ferrite superlattices with different modulation wavelengths.

Further characterization has not been done in these superlattices. Due to a large variation in the properties of the individual layers in the superlattice, they might produce some interesting results during the magnetic measurements.

REFERENCES

1. J. A. Switzer, M. J. Shane, and R. J. Philips, Science, 247, 444 (1990).
2. J. A. Switzer, R. P. Raffaelle, R. J. Philips, C. -J. Hung, and T. D. Golden, Science, 258, 1918 (1992).
3. T. D. Golden, R. P. Raffaelle, and J. A. Switzer, Appl. Phys. Lett. 63, 1501 (1993).
4. J. A. Switzer, and T. D. Golden, Adv. Mater, 5, 474 (1993).
5. R. J. Phillips, T. D. Golden, M. G. Shumsky, E. W. Bohannan and J. A. Switzer, Chem. Mater., 9, 1670 (1997).
6. E. Bauer, and J. H. van der Merwe, Phys. Rev. B., 33, 3657 (1986).
7. D. M. Tench, and J. T. White, J. Electrochem. Soc., 137, 3061 (1990).
8. D. S. Lashmore, and R. Thomson, J. Mater. Res., 7, 2379 (1992).
9. T. Torimoto, A. Obayashi, S. Kuwabata, H. Yoneyama, Electrochem. Comm., 2, 359 (2000).
10. R. Vaidyanathan, S. M. Cox, U. Happek, D. Banga, M. K. Mathe, J. L. Stickney, Langmuir, 22, 10590 (2006).
11. X. Dou, G. Li, H. Lei, Nano. Lett. 8, 1286 (2008).
12. S. Zou, M. J. Weaver, Chem. Phys. Lett. 312, 101 (1999).
13. H. M. Kothari, A. A. Vertegel, E. W. Bohannan, J. A. Switzer, Chem. Mater. 14, 2750 (2002).
14. F. Imai, K. Kunimori, and T. Uchijima, Thin Solid Films, 228, 158 (1993).
15. J. A. Switzer, C. –J. Hung, B. E. Breyfogle, M. G. Shumsky, R. V. Leeuwen, and T. D. Golden, Science, 264, 1505 (1994).
16. J. A. Switzer, R. V. Gudavarthy, E. A. Kulp, G. Mu, Z. He, and A. Wessel, J. Am. Chem. Soc., 132, 1258 (2010).
17. J. A. Switzer, M. J. Shane, and R. J. Philips, Science, 247, 444 (1990).
18. B. Yoo, F. Xiao, K. N. Bozhilov, J. Herman, M. A. Ryan, and N. V. Myung, Adv. Mater., 19, 296 (2007).

19. Y. Fujii, *Metallic Superlattices: Artificially Structured Materials;* T. Shinjo, T. Takada, Eds.; Elsevier, Amsterdam, 1987.

20. F. J. Lamelas, H. D. He, and R. Clarke, Phys. Rev. B, 43, 12296 (1991).

21. C. A. Ross, Annu. Rev. Mater. Sci. 24, 159 (1994).

22. Odagawa, Y. Katoh, Y. Kanzawa, Z. Wei, T. Mikawa, S. Muraoka, and T. Takagi, Appl. Phys. Lett., 91, 133503 (2007).

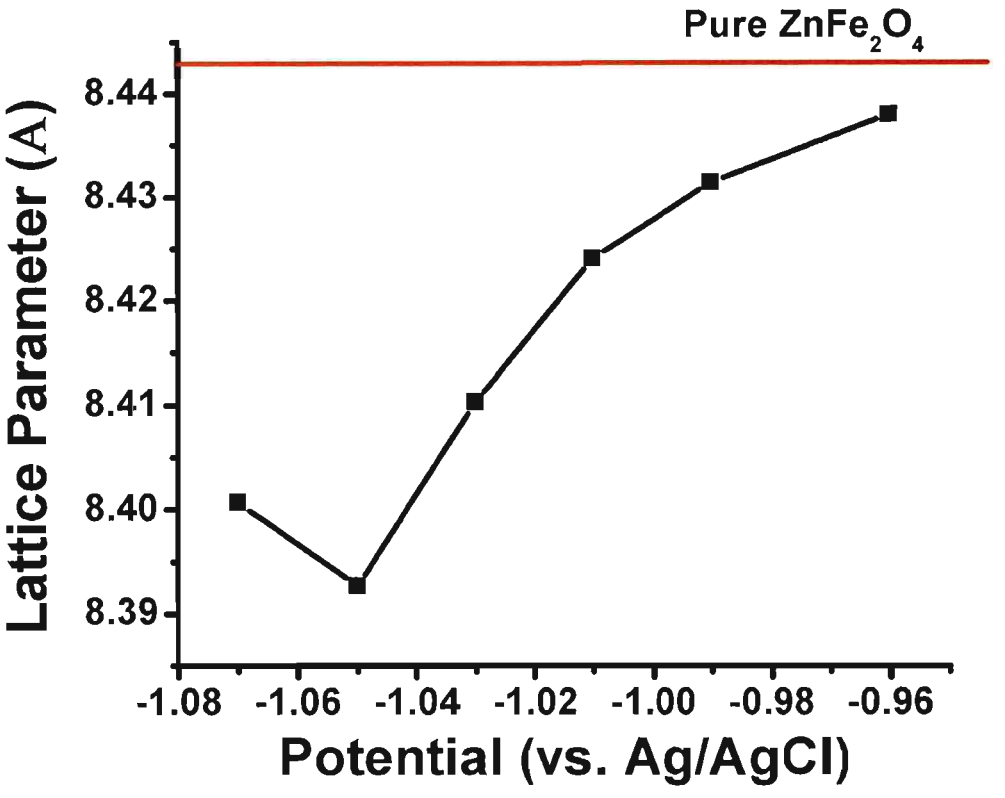

Figure D.1. Lattice parameter as a function of applied potential for zinc ferrite films deposited on Au covered glass substrate.

Table D.1. Table showing the current densities, Zn concentrations at different potentials, and the lattice parameter at different potentials for zinc ferrite films.

Applied potential (V vs. Ag/AgCl)	Current density (mA/cm^2)	Atomic percent of Zn^{2+} from EDS Ideal: 33.33%	Lattice parameter (A) Ideal: 8.4410 A
-0.96	0.8	32.1	8.4380
-0.99	1.2	28.9	8.4314
-1.01	1.5	28.5	8.4241
-1.03	3.5	25.9	8.4103
-1.05	4.5	24.3	8.3927
-1.07	7	10.7	8.4007

Table D.2. Sheet resistance of zinc ferrite films at different potentials. The four probe measurements were done by peeling the film on to a glass slide using super glue.

Potential	Sheet resistance (Ω/square)
-0.96 V	6.17×10^6
-0.99 V	3.2×10^6
-1.01 V	3.32×10^5
-1.03 V	2.4×10^5
-1.05 V	1.49×10^5

Table D.3. Coherence length data for zinc ferrite superlattices with different modulation wavelengths

Dwell time at -0.99 V	**Dwell time at -1.05 V**	**Λ_x (X-ray data) (nm)**	**Coherence length (L) (nm)**
7.5	1.5	29.2	47.41
5	1	16.8	43.82
2.5	0.5	12.5	58.35

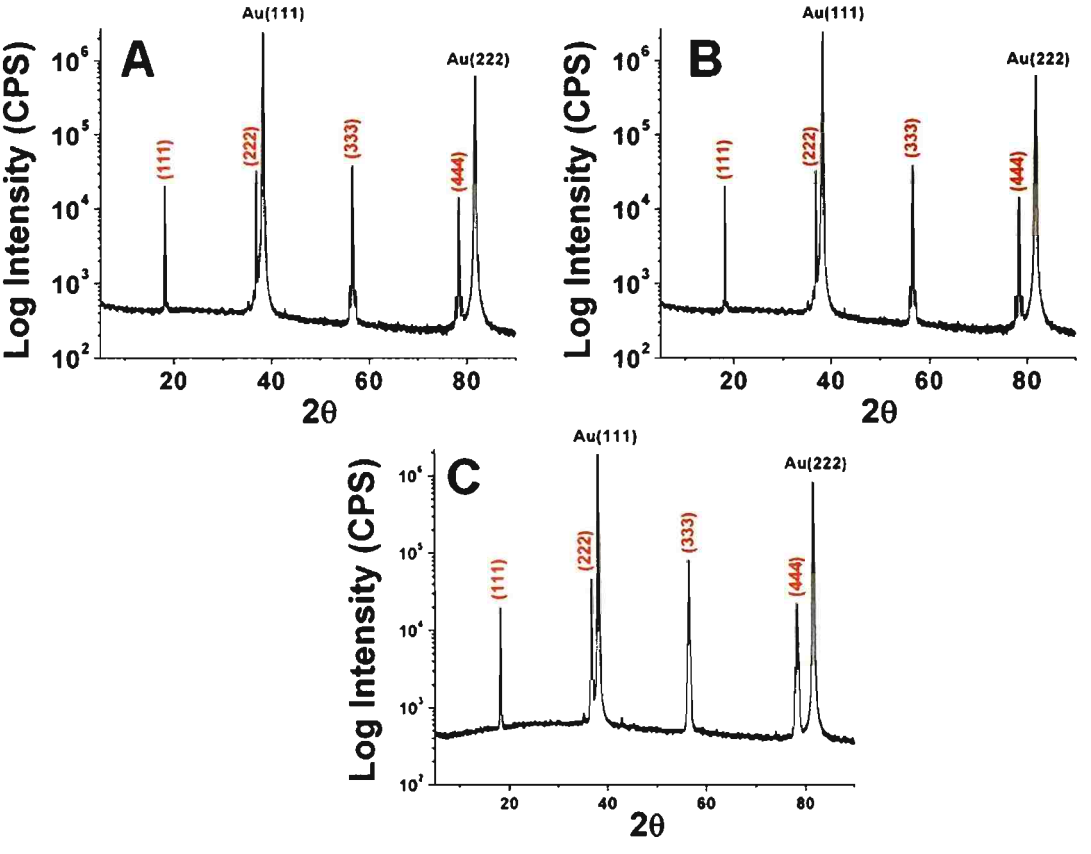

Figure D.2. X-ray θ-2θ scans for the zinc ferrite superlattices with different modulation wavelength electrodeposited on Au(111). (A) Modulation wavelength of 12.2 nm, (B) 16.5 nm and (C) 29.2 nm.

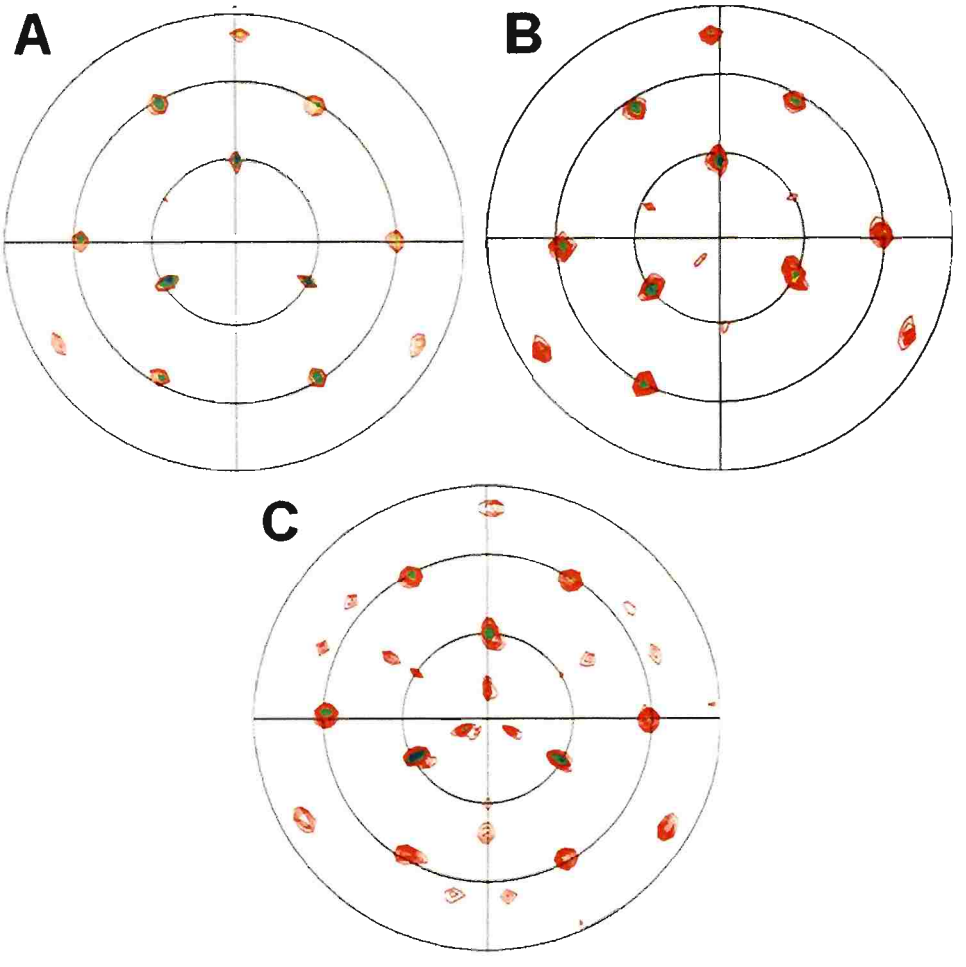

Figure D.3. (311) pole figures of zinc ferrite superlattices with different modulation wavelengths. (A) 12.2 nm, (B) 16.5 nm and (C) 29.2 nm.

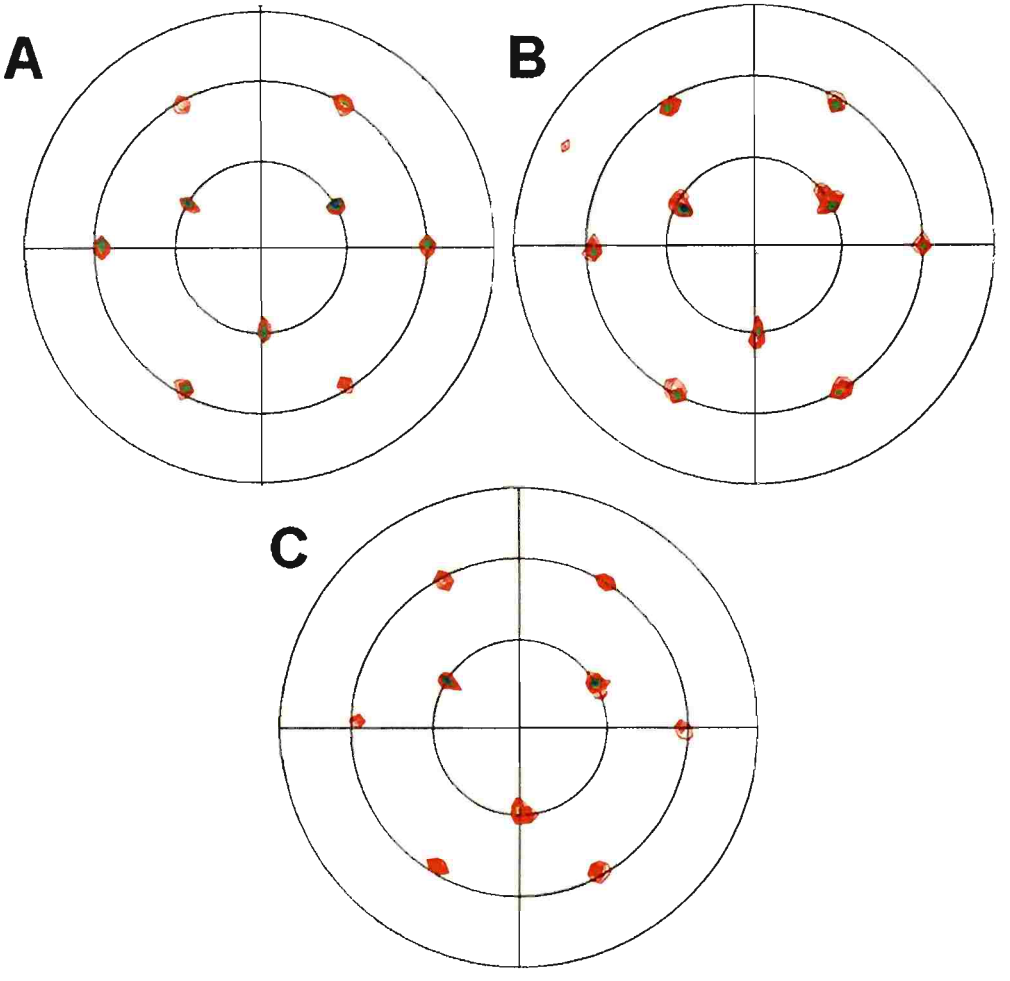

Figure D.4. (311) Au substrate pole figures for the zinc ferrite superlattices with different modulation wavelengths. (A) 12.2 nm (B) 16.5 nm and (C) 29.2 nm.

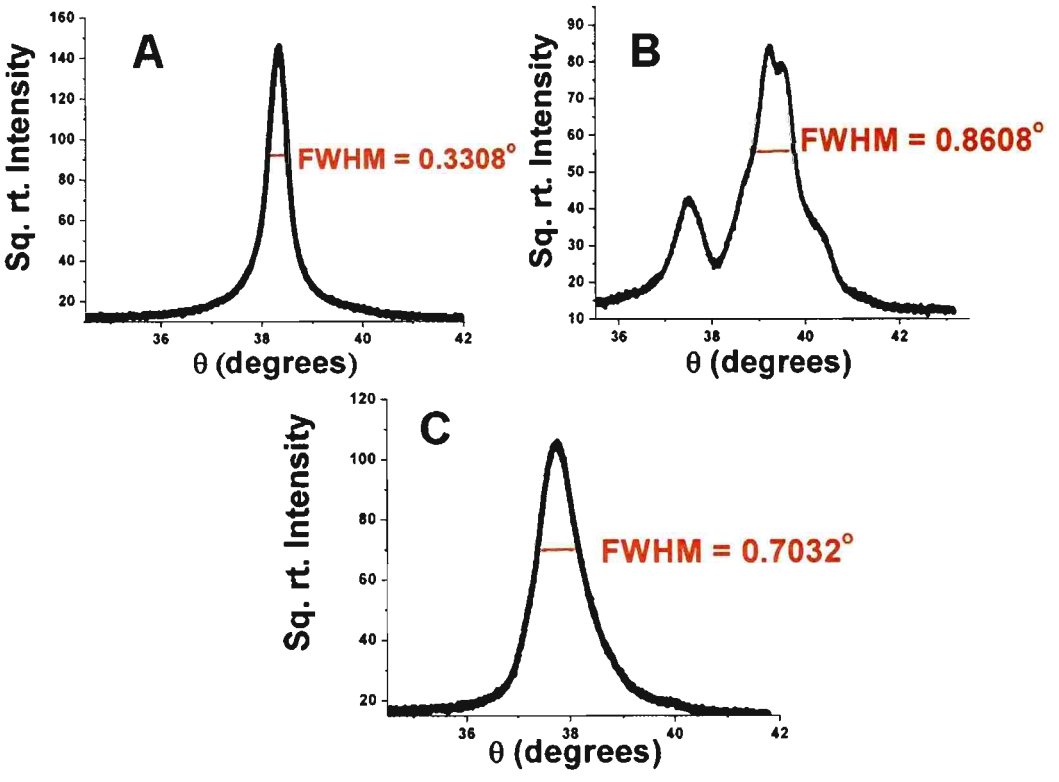

Figure D.5. Rocking curves for the superlattices of zinc ferrite with different modulation wavelengths. (A) 12.2 nm (B) 16.5 nm and (C) 29.2 nm.

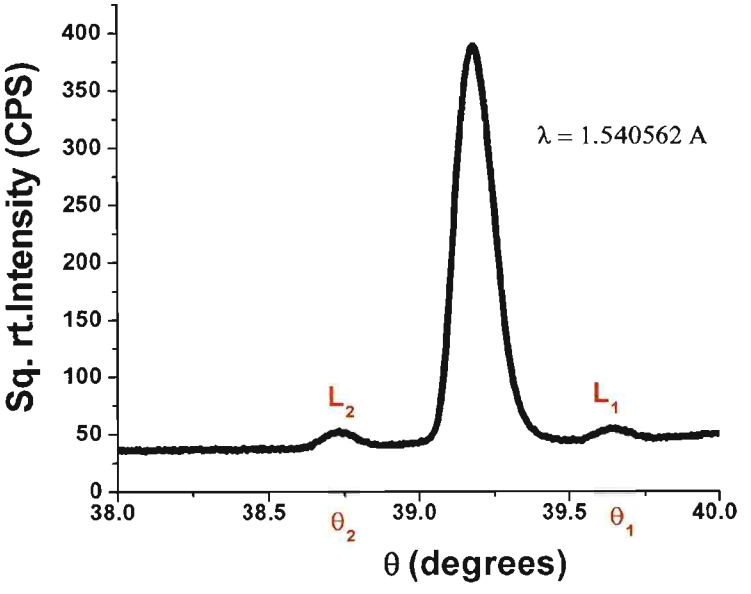

Figure D.6. X-ray 2θ scan for zinc ferrite superlattice with 12.2 nm modulation wavelength. The scan shows the terms used in the equation for calculation of modulation wavelength.

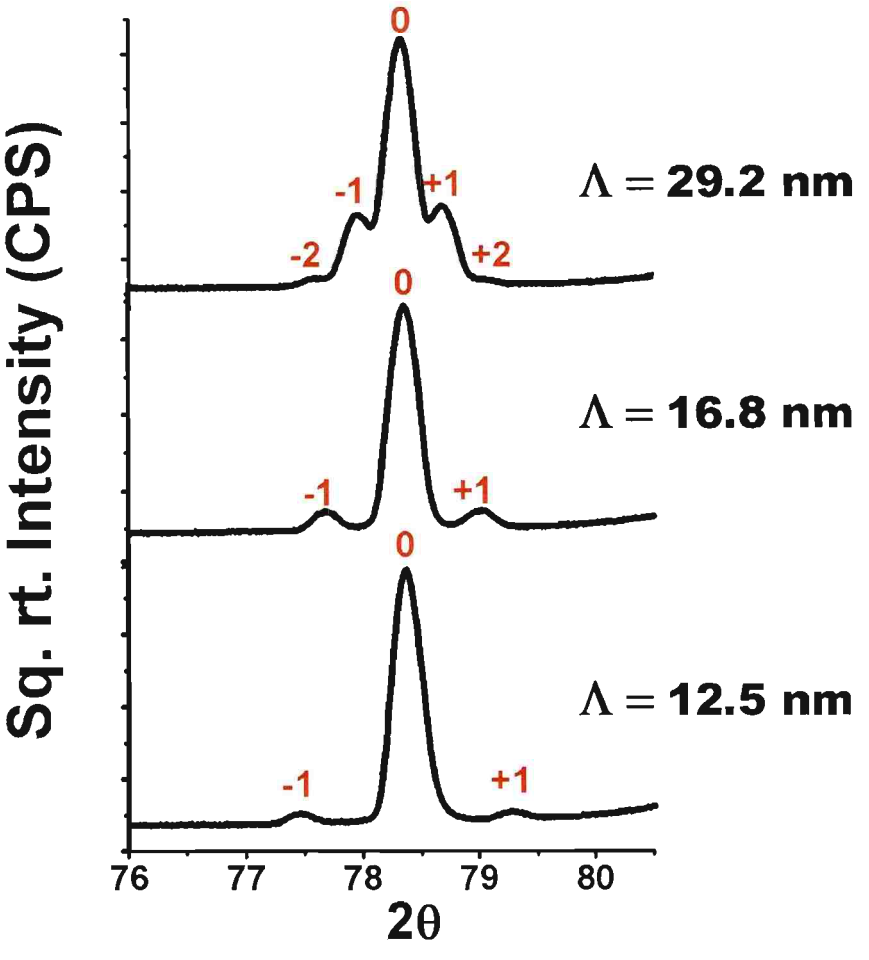

Figure D.7. X-ray 2θ scan showing slow scan around the (444) peak for zinc ferrite superlattices with different modulation wavelengths

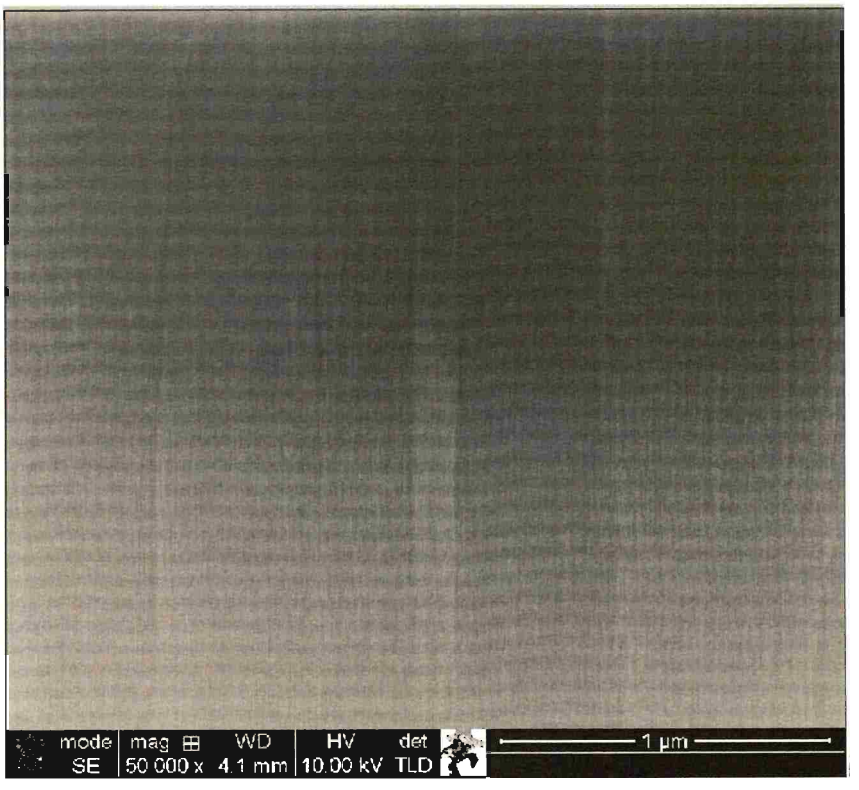

Figure D.8. High angle annular dark field image of zinc ferrite superlattice with a modulation wavelength of 70 nm.

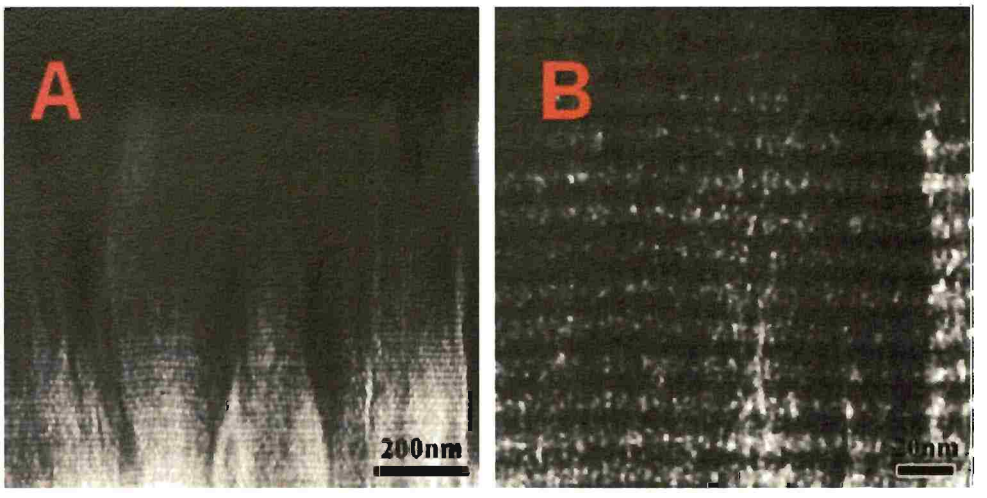

Figure D.9. High angle annular dark field image of the zinc ferrite superlattice with a modulation wavelength of 16.5 nm (A) HAADF image of the whole film and (B) high magnification HAADF image of the film.

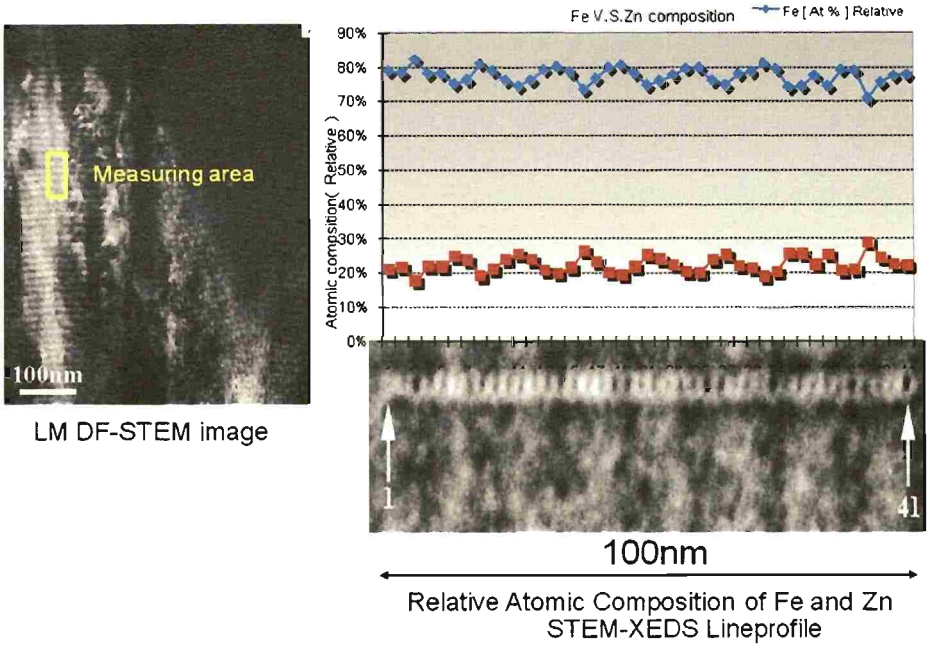

Figure D.10. X-ray energy dispersive spectroscopy on a zinc ferrite superlattice with a modulation wavelength of 16.5 nm. The scan shows the composition variation in the layered structure of a superlattice.

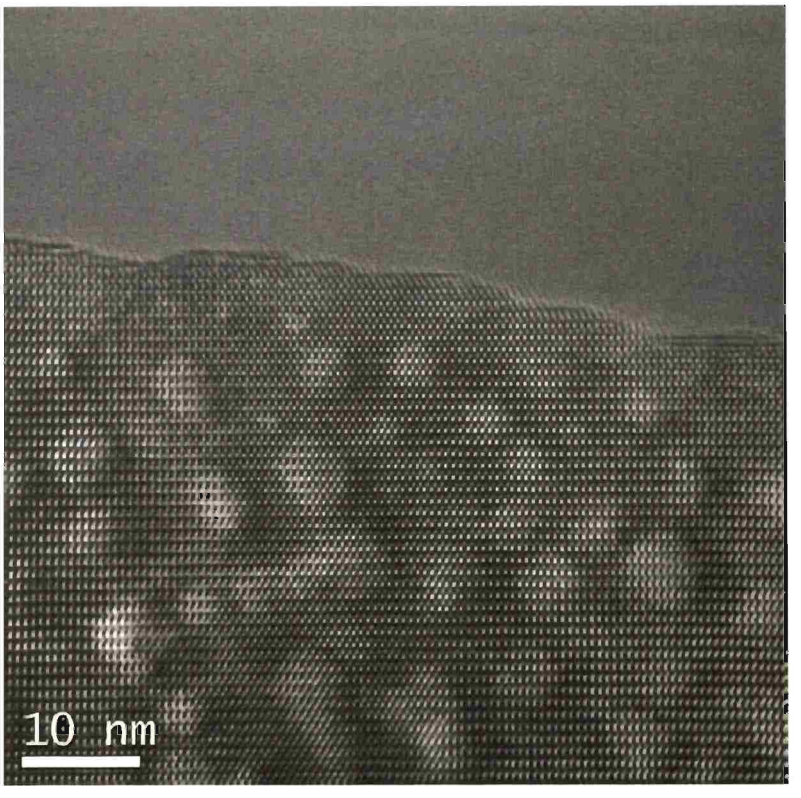

Figure D.11. High resolution TEM image showing lattice fringes in a 12.2 nm zinc ferrite superlattice

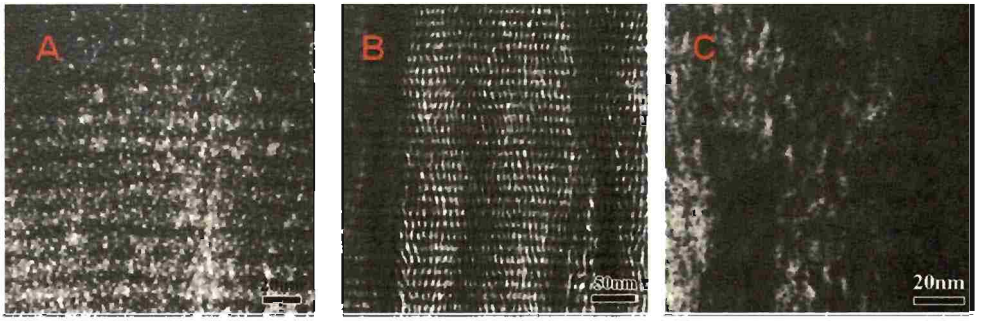

Figure D.12. High angle annular dark field image of the zinc ferrite superlattice with a modulation wavelength of 16.5 nm. Images show the problems during the sample preparation. (A) White spots, (B) white patterns coming from milling process, probably an artifact, and (C) black spots due to milling process.

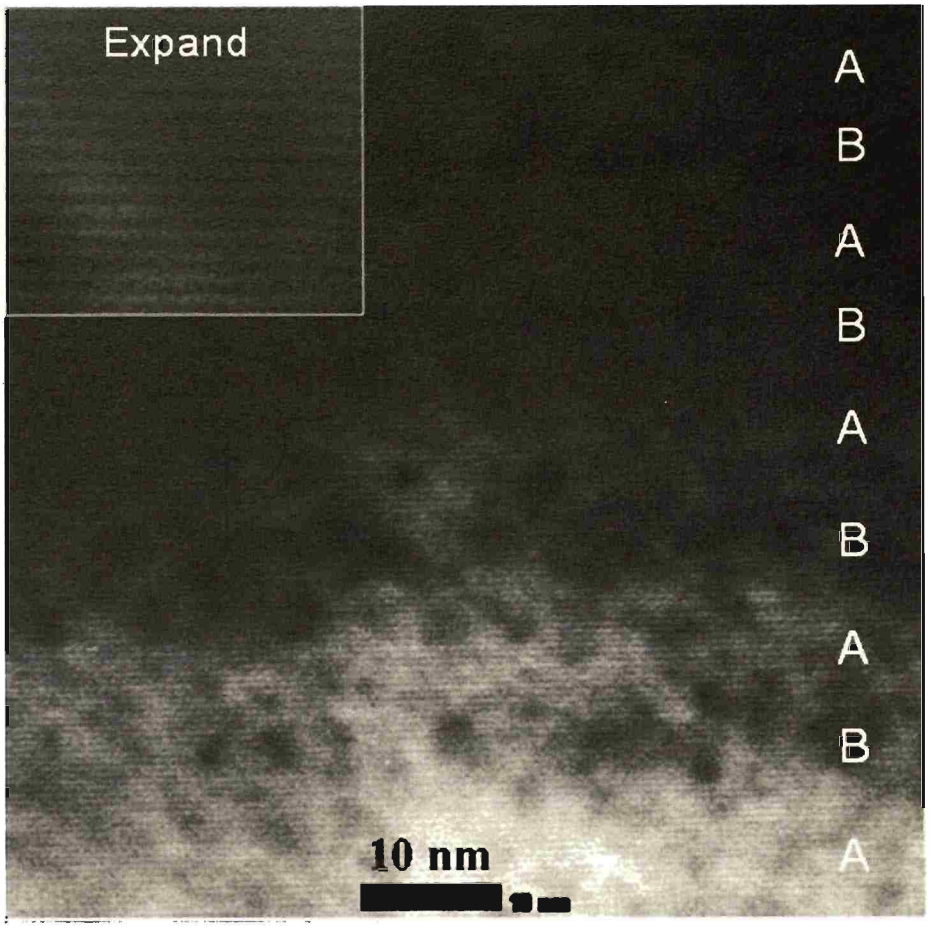

Figure D.13. High resolution TEM image of a zinc ferrite superlattice with modulation wavelength of 16.5 nm. The image shows the alternating layers in the superlattice marked as A and B. The inset shows the overall image of the superlattice with alternating layers at lower magnification.

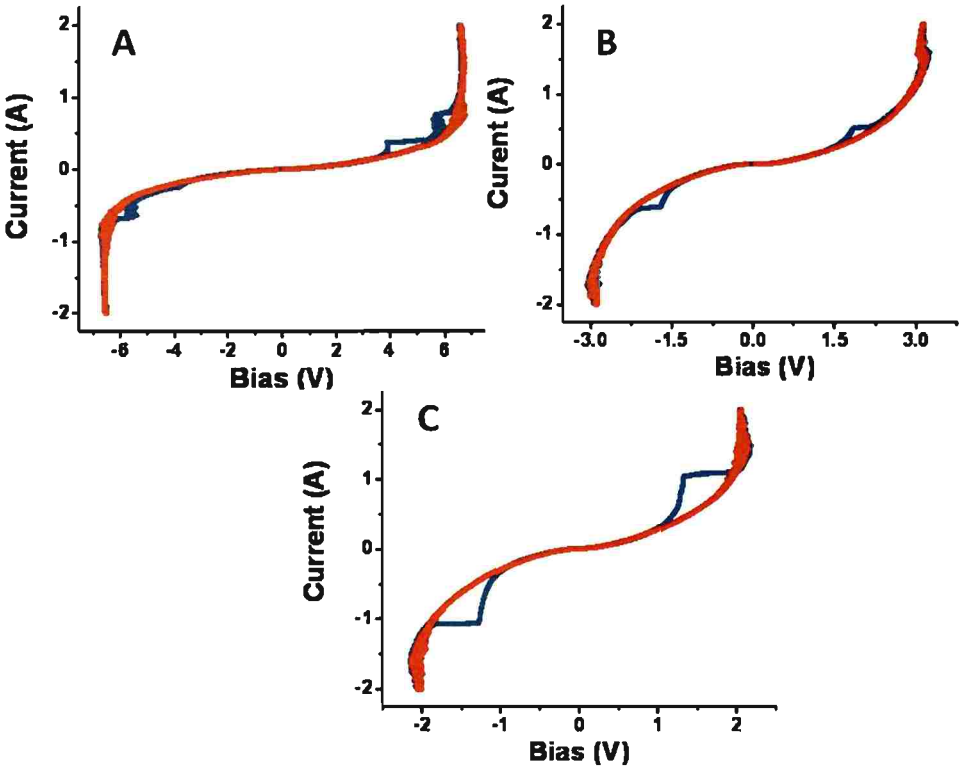

Figure D.14. Resistance switching of (A) -990 mV zinc ferrite film, (B) -1.05 V zinc ferrite film, and (C) a zinc ferrite superlattice on Au(111) at 77 K. The iV curves were obtained by scanning the current at 50 mA/s. In each curve the blue line corresponds to the forward scan and the red line corresponds to the reverse scan.

Table D.4. Deposition conditions for the zinc ferrite superlattices on Au(111).

Dwell time -0.96 V	Dwell time -1.05 V	Λ_x (x-ray data nm)
30	1	26.4
20	1	21
10	1	18.6

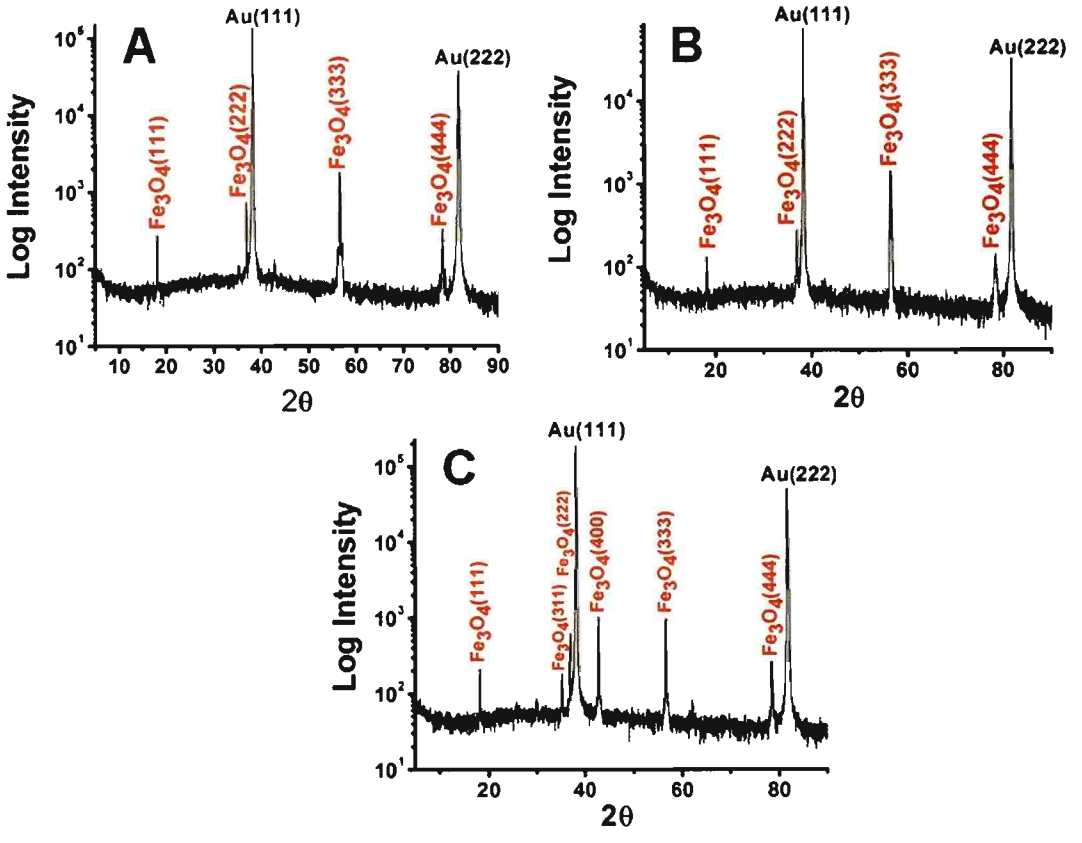

Figure D.15. X-ray θ-2θ scans for the zinc ferrite superlattices with different modulation wavelength electrodeposited on Au(111). (A) Modulation wavelength of 26.4 nm, (B) 21 nm and (C) 18.6 nm.

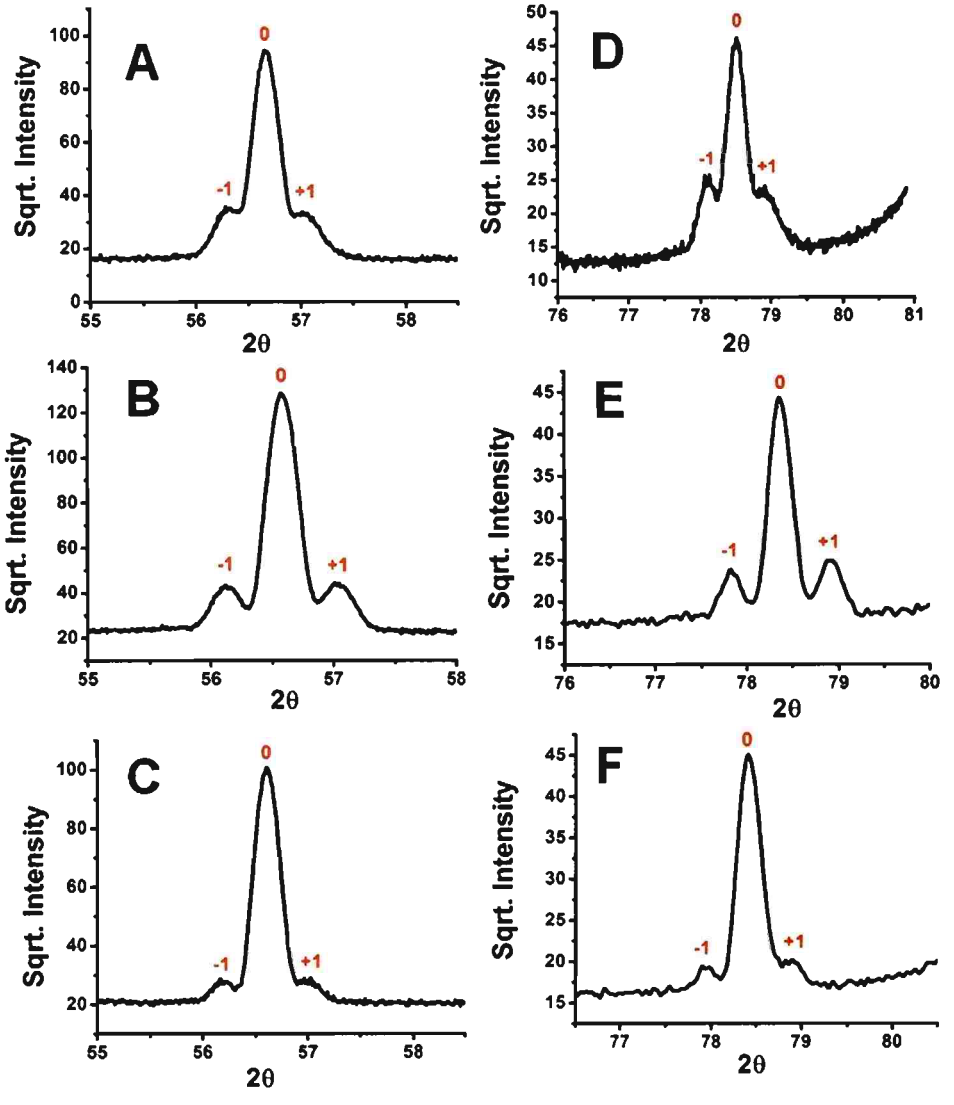

Figure D.16. X-ray 2θ scan showing slow scan around the (333) (A), (B), and (C) and (444) peak (D), (E), and (F) for zinc ferrite superlattices with 29.4, 21, and 18.6 nm modulation wavelengths.

APPENDIX E.

EPITAXIAL ELECTRODEPOSITION OF CHIRAL CuO ON Cu(111) SUBSTRATE USING DIFFERENT AMINO ACIDS.

Experimental Section

The deposition solution contained 0.005 M $CuSO_4$, 0.05 M amino acid, and 0.2 M NaOH. Water was HPLC-grade (Aldrich), and other chemicals were reagent-grade (Aldrich). The solution was prepared by dissolving NaOH pellets in water in a separate beaker and letting it cool to room temperature before adding it to a solution containing amino acid and $CuSO_4$. The deposition was carried out at room temperature. Working electrodes consisted of 1 cm diameter Cu(111) single crystals purchased from Monocrystals company. A copper wire fitted around the edge of the single crystals served as electrical contact during the deposition. The counter electrode was a platinum wire and the reference electrode was a saturated calomel electrode (SCE). The deposition was performed at a fixed potential of 0.45 V vs. SCE for 45 min with an EG&G Princeton Applied Research model 273 A potentiostat/galvanostat. The thickness of the deposited films was approximately 300 nm.

X-ray diffraction (XRD) experiments were performed with a high-resolution Philips X'Pert MRD diffractometer. Pole figures were obtained in point-focus mode using crossed-slit collimator as the primary optics and a 0.27^{o} parallel plate collimator and flat graphite monochromator as the secondary optics. A 2θ value of 38.742^{o} was used to probe the (111) reflection of CuO.

Results and Discussion

Table 1 shows different chiral reagents used for depositing CuO films. The table also indicates their handedness in different conventions.[1] Usually, there are three different types of conventions which are followed for chiral molecules. Optical activity (+/-) is based on the direction in which the enantiomer rotates the plane polarized light. The (+) and (-) enantiomer are also identified as dextrorotatory (d) and levorotatory (l). This notation can be easily confused with D and L labeling. The D/L labeling is unrelated to +/- notation; it does indicate which enantiomer is dextrorotatory or levorotatory. Rather, it says that the compound's stereochemistry is related to the stereochemistry of the dextrorotatory and levorotatory enantiomer of glyceraldehydes. Another convention which is generally used is the R/S configuration. In this convention, each chiral center in the molecule is either named R or S according to a system by which its substituent's are

each assigned a priority. The priorities are based on Cahn Ingold Prelog rules, based on atomic number. The R/S system has no fixed relation with +/- or D/L systems. An R isomer can be either dextrorotatory or levorotatory, depending on its exact substituents.[2]

In this work, different chiral reagents were used to deposit CuO films on Cu(111) single crystals to understand the role of the precursor on chiral film formation. Figure E.1 shows the (111) pole figures for CuO on Cu(111) deposited from different chiral reagents. The pole figures were obtained by setting 2θ equal to the angle of diffracted intensity for the (111) planes ($2\theta = 38.742^{\circ}$) and performing azimuthal scans at tilt angles, χ, from 0 to 90°. The pole figures in Figure E.1. (A) - (E) show peaks at 57° and 63°. These peaks correspond to either $(\bar{1}11)$ orientation or $(1\bar{1}\bar{1})$ orientation. On the other hand, the pole figures in Figures E.1. (F) – (H) have extra peaks at tilt angle of 27°, which correspond to either (311) or $(\bar{3}\bar{1}\bar{1})$ orientation. Figure E.2 shows the stereographic projections for all the four orientations. No conclusions can be drawn based on the pole figure data for the CuO deposited from different amino acids. For example, the L(-) proline and L(-) asparatic acid have mirror image pole figures even though the CuO films are grown from the same handed enantiomer.

Figure E.3 shows the SEM images of the CuO films deposited on Cu(111) single crystal from different chiral reagents. The chiral reagents influence the morphology of the deposited films. Figure E.3 (D) shows the SEM image of the CuO film deposited using L-asparatic acid precursor. The image shows that CuO grows like spears and are approximately 50 nm in diameter. On the other hand, films deposited using L- arginine has cross hatch morphology with individual crystallites made up of multiple platelets. The morphology of the films deposited from other amino acids and simple carboxylic acids like malic acid and tartaric acid have simple cross hatch morphology with different crystallite sizes.

REFERENCES

1. R. C. Weast, CRC Handbook of Chemistry and Physics, C704 (1998).

2. E. L. Eliel, and S. H. Wilen, *The Stereochemistry of Organic Compounds*, Wiley-Interscience (1994).

Table E.1. List of chiral precursors used for depositing CuO on Cu(111) single crystal. The table also lists different types of notations used for chiral molecules.

Amino Acids	*(+) /(-) notation*	*d/l – notation*	*D/L-notation*	*R/S-Notation*
Alanine	+	d	L	S
Arginine	+	d	L	S
Asparatic acid	-	l	L	S
Glutamic acid	+	d	L	S
Valine	-	l	L	S
Tartaric acid	+	d	L	R, R
Malic acid	-	l	L	S
Proline	-	l	L	S

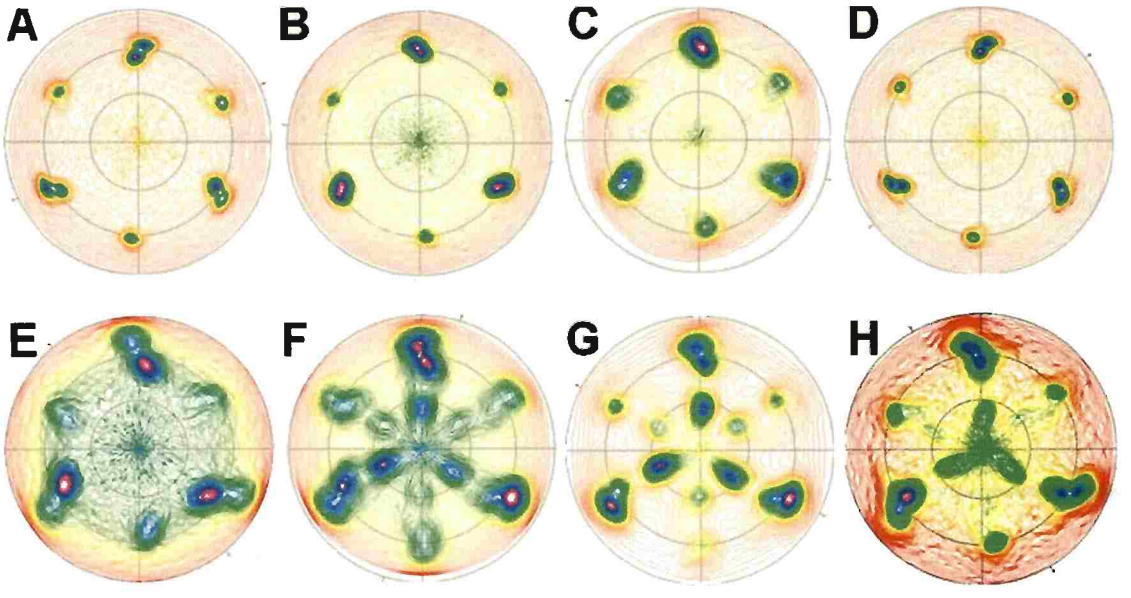

Figure E.1. (111) CuO pole figure for CuO films deposited from different amino acids on Cu(111) single crystals. (A) tartaric acid, (B) asparatic acid, (C) glutamic acid, (D) proline, (E) arginine, (F) alanine, (G) valine and (H) malic acid.

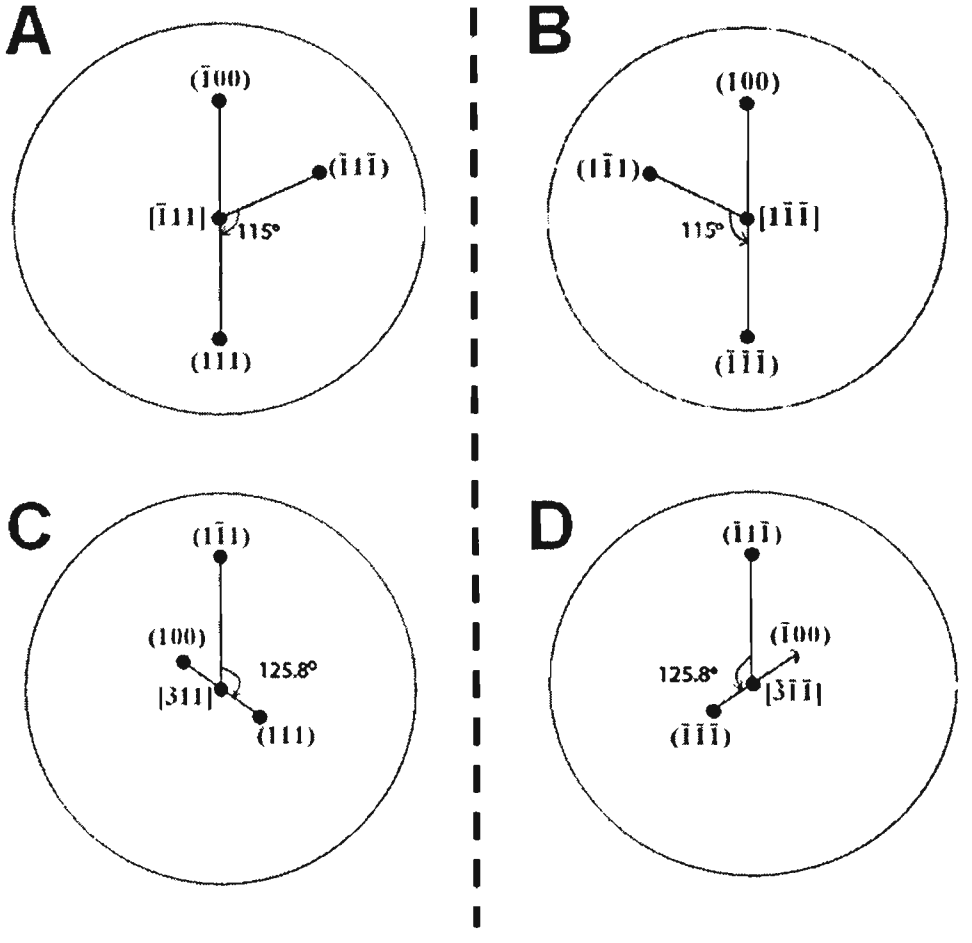

Figure E.2. Stereographic projections for (A) $(\bar{1}\,\bar{1}\,1)$, (B) $(11\bar{1})$, (C) (311) and (D) $(\bar{3}\,\bar{1}\,\bar{1})$ orientations indicating the positions where the (111) type and (100) type reflections should be observed in the pole figures. For the $(\bar{1}\,\bar{1}\,1)$ orientation, reflections from the $(1\,\bar{1}\,1)$ plane at $\chi = 57^{\circ}$ and the $(\bar{1}\,\bar{1}\,\bar{1})$ plane at $\chi = 63^{\circ}$ are separated azimuthally by 115° rotated counterclockwise. For the $(\bar{3}\,\bar{1}\,\bar{1})$ orientation the $(1\,\bar{1}\,1)$ plane is at $\chi = 68.14^{\circ}$, the $(\bar{1}\,\bar{1}\,\bar{1})$ planes at $\chi = 27.41^{\circ}$ and (100) planes at $\chi = 27.19^{\circ}$. For the $(11\bar{1})$ orientation the $(\bar{1}\,1\,\bar{1})$ plane is at $\chi = 57^{\circ}$ and the (111) plane is at $\chi = 63^{\circ}$ are separated azimuthally by 115° rotated clockwise. For the (311) orientation the $(1\,\bar{1}\,1)$ plane at $\chi = 68.14^{\circ}$, the (111) plane at $\chi = 27.41^{\circ}$ are separated azimuthally by 125.8°.

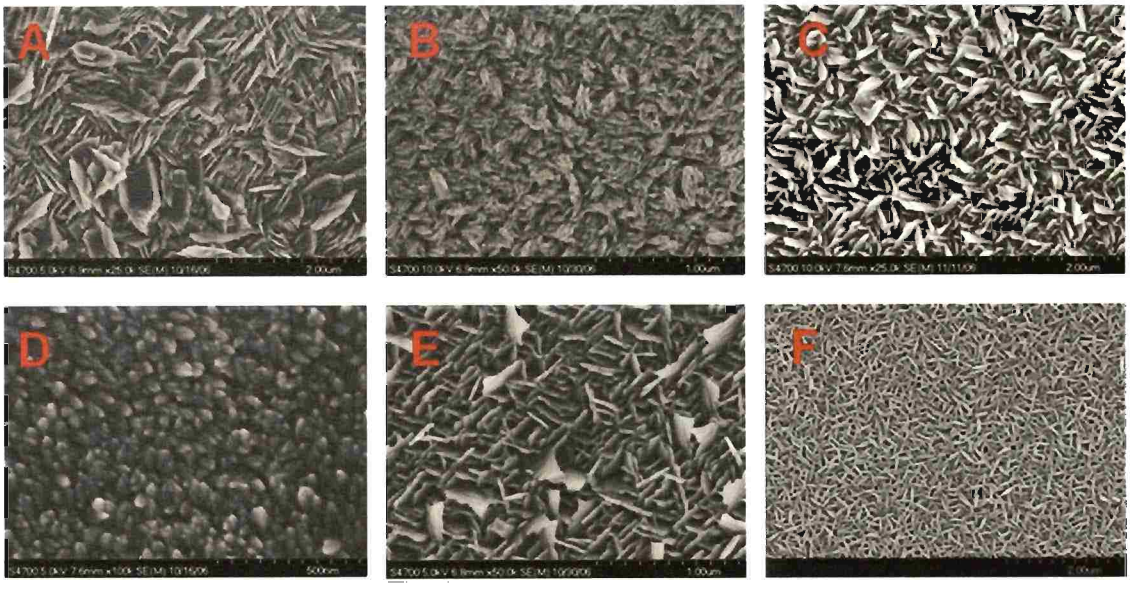

Figure E.3. SEM micrographs for CuO films deposited on Cu(111) single crystal from different chiral precursors. (A) L(+)-Alanine, (B) L(-)-Arginine, (C) L(+)-Valine, (D) L(-)-Aspartic acid, (E) L(+)-Glutamic acid

VITA

Rakesh Vathsal Gudavarthy was born on August 11, 1982, in Shadnagar, Andhra Pradesh, India, to Sujan Vathsal Gudavarthy and Sharadha Gudavarthy. He received his Bachelor of Technology (B.Tech) degree in Chemical Engineering from B. V. Raju Institute of Technology (BVRIT) affiliated to Jawahar Lal Nehru Technological University (JNTU), India in 2005. He received the Best Outgoing Student award from Indian Institute of Chemical Engineers, Hyderabad, India in 2005. During his B.Tech program at BVRIT, he was involved in research projects with Environmental Protection and Training Research Institute (EPTRI), Indian Institute of Chemical Technology (IICT), and Defense Research Development Laboratories (DRDL). He has presented several technical papers at national conferences in India, many of which were declared as the best in the conference. In August 2005, he came to Missouri University of Science and Technology (Missouri S&T) to pursue his Doctor of Philosophy degree in Chemistry. Since November 2005, he has researched under the guidance of Prof. Jay A. Switzer who offered him a research assistantship. Mr. Gudavarthy's research has involved the electrodeposition and characterization of epitaxial metal oxides films and superlattices. During his PhD program at S&T, Mr. Gudavarthy was invited for a summer school on surface science and nanomaterials at University of California at Santa Barbara organized by National Science Foundation (NSF) in 2006. He also interned at Novellus Systems, Inc. in fall 2009 under the guidance of Dr. Jon Reid. He was invited to present his research work at the Student Potter's Lodge Meeting in New York in 2010. He graduated from Missouri University of Science and Technology with a PhD in Chemistry in May 2011.

In addition, Mr. Gudavarthy was involved in many campus activities during his PhD Program at Missouri S&T. He served as the President of International Students Club at S&T from 2007-2008. During the same period, he served as the Secretary for Council of Graduate Students (CGS). He then became the President for CGS in 2008. As the President of CGS, he represented graduate students in University of Missouri Board of Curators meetings, faculty senate, and Rules and Procedures committee.